UNIMORE
UNIVERSITÀ DEGLI STUDI DI MODENA E REGGIO EMILIA

UNIVERSITÀ DEGLI STUDI DI MODENA E REGGIO EMILIA

Dottorato di ricerca in Ingegneria industriale e del territorio

Ciclo XXXVIII

Sustainable Urban Bus Transit: An Integrated Study of Driving Cycle Generation, Powertrain Performance, and Green Hydrogen Production

Candidato: Ahmet Fatih Kaya

Relatore (Tutor): Prof.Simone Pedrazzi

Eventuale Correlatore (Co-Tutor): Dr. Marco Puglia

Eventuale Secondo Correlatore (Co-Tutor): Dr. Nicolò Morselli

Coordinatore del Corso di Dottorato: Prof. Alberto Muscio

To my father, ***Mehmet Akif Kaya****, who has always believed in me...*

First, I wish to express my deepest gratitude to my supervisor, ***Prof. Simone Pedrazzi****. His guidance has played a pivotal role in my academic development, broadening my research perspectives in ways I had not imagined.*

I am also indebted to ***Prof. Alberto Muscio****, whose exceptional warmth and constant support were fundamental to this process. His encouragement made this journey much smoother.*

This journey was made possible by the ***Republic of Türkiye Ministry of National Education*** *and the* ***YLSY scholarship program****. I appreciate the trust they placed in me and the financial support that allowed me to pursue this degree.*

I would like to thank my uncle, ***Ali Doluküp****, for his unwavering presence and for standing by me whenever I needed assistance.*

Last but certainly not least, I owe a debt of gratitude to my wife, ***Elif Kaya****. She has believed in me unconditionally as we embarked on this path together. Her support and positive spirit provided the balance I needed. I am grateful for her companionship throughout these years.*

INDEX

Graphical Abstract

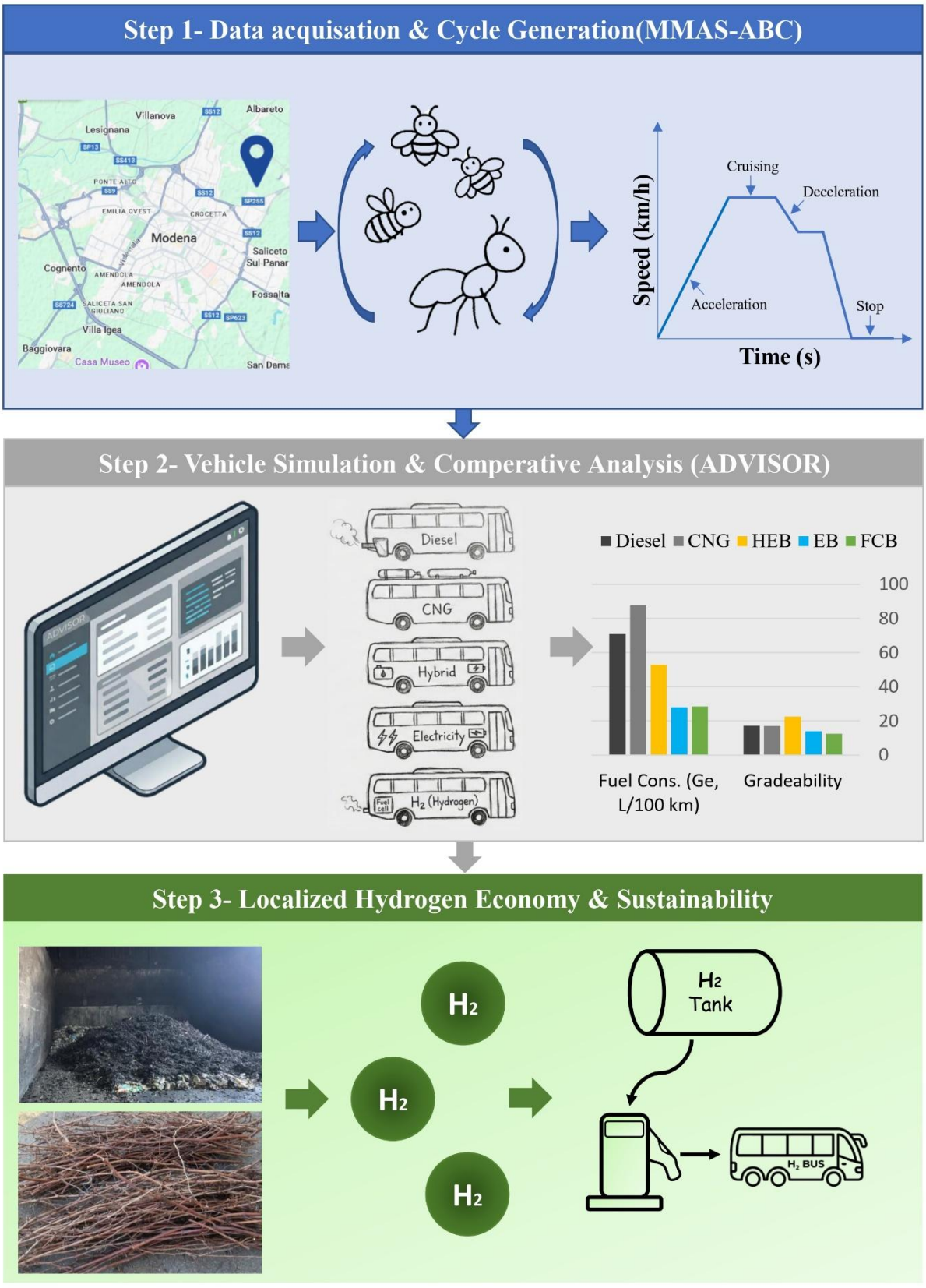

Graphical Summary of the Key Findings

(Section 4.1.)

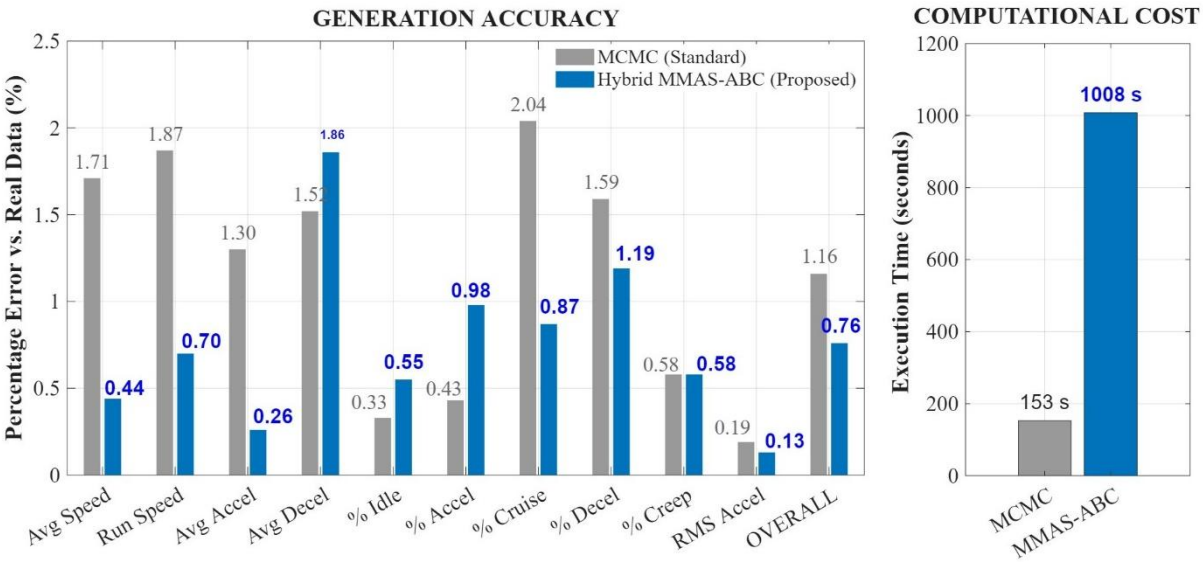

(Section 4.2. and 4.3.)

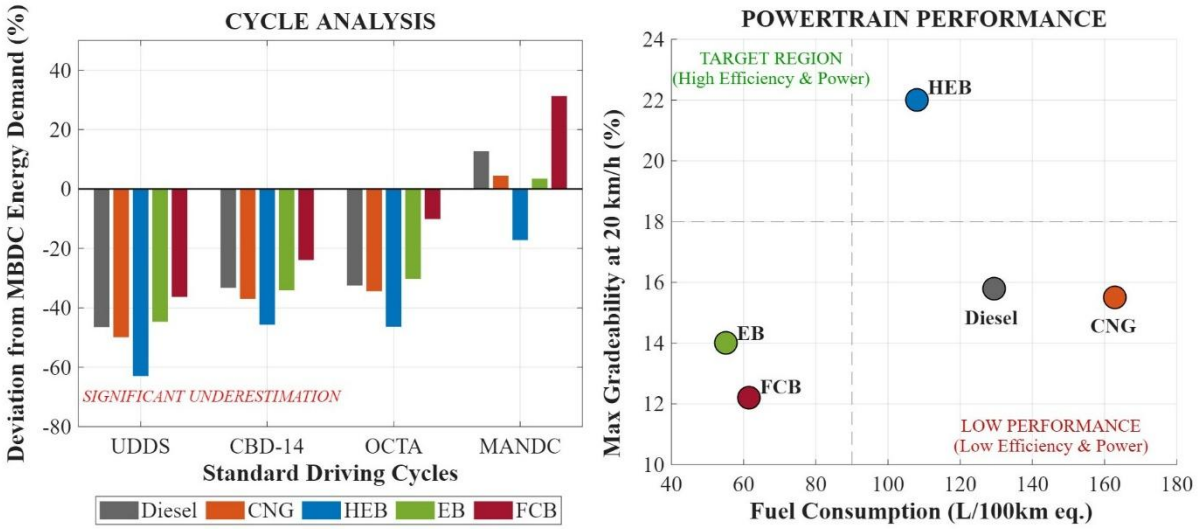

(Section 4.4.)

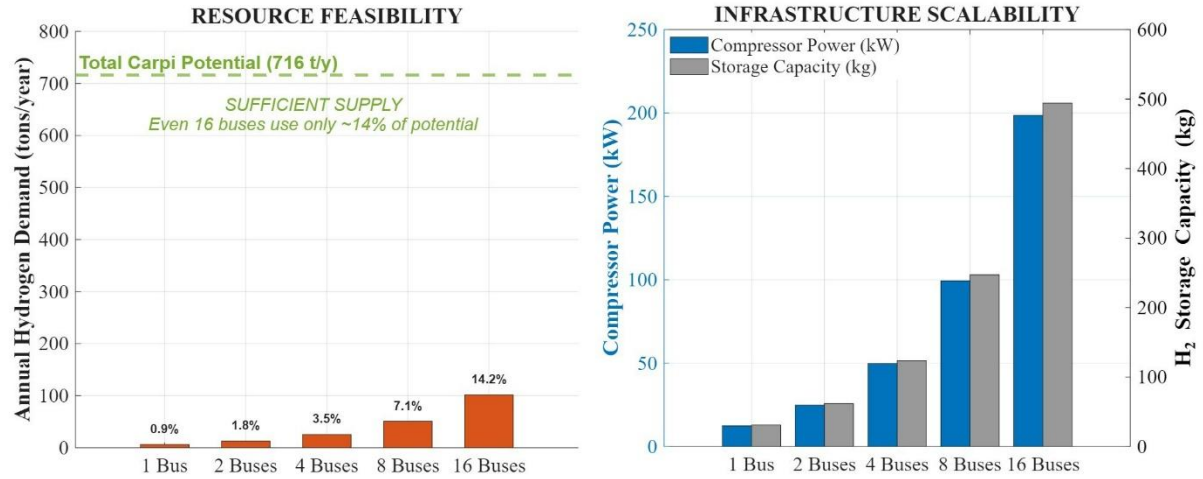

Sustainable Urban Bus Transit: An Integrated Study of Driving Cycle Generation, Powertrain Performance, and Green Hydrogen Production

Abstract (English)

The global transition toward sustainable urban public transport faces two critical barriers: the inadequacy of standardized driving cycles to capture local real-world driving behaviour, and the absence of an integrated assessment framework for evaluating the technological and infrastructural feasibility of green transportation solutions. This thesis proposes a comprehensive multi-scale methodology to bridge these gaps, linking microscopic driving dynamics with the macroscopic design and sizing of a standalone hydrogen refuelling station.

The first stage of the research focuses on developing a representative Modena Bus Driving Cycle (MBDC) through a hybrid metaheuristic optimization algorithm that combines the MAX–MIN Ant System (MMAS) and the Artificial Bee Colony (ABC) algorithm. This hybrid approach demonstrated superior performance in reproducing actual driving data, significantly improving upon conventional stochastic modelling techniques such as the Markov Chain Monte Carlo (MCMC) method.

In the second stage, five different bus powertrain configurations—Diesel, Compressed Natural Gas (CNG), Hybrid Electric (HEB), Battery Electric (EB), and Fuel Cell (FCB)—were developed and benchmarked using the ADVISOR simulation environment. The validated models were subsequently tested under the MBDC to assess their energy consumption and operational performance under realistic local driving conditions. This comparison revealed notable discrepancies between standardized and locally derived cycles, emphasizing the importance of localized testing for accurate energy evaluations.

Finally, the study explores the feasibility of a localized green hydrogen infrastructure to support a future FCB fleet in Modena. Using projected hydrogen demand scenarios derived from operational data, a conceptual Hydrogen Refuelling Station (HRS) was designed and its major components sized accordingly. The potential of regional biomass sources, including Organic Fraction of Municipal Solid Waste (OFMSW) and woody biomass, was also assessed for local bio-hydrogen production capacity.

Overall, the research establishes an integrated and scientifically robust framework for sustainable urban bus transit, connecting real-world drive cycle generation, comparative powertrain analysis, and renewable hydrogen infrastructure design.

Trasporto Pubblico Urbano Sostenibile su Autobus: uno Studio Integrato sulla Generazione di Cicli di Guida, le Prestazioni del Gruppo Motopropulsore e la Produzione di Idrogeno Verde

Abstract (Italian)

La transizione globale verso un trasporto pubblico urbano sostenibile affronta due ostacoli critici: l'inadeguatezza dei cicli di guida standardizzati nel rappresentare il comportamento di guida reale a livello locale e l'assenza di un quadro di valutazione integrato per l'analisi della fattibilità tecnologica e infrastrutturale delle soluzioni di trasporto ecologiche. Questa tesi propone una metodologia completa e multi-scala per colmare tali lacune, collegando la dinamica di guida microscopica con la progettazione e il dimensionamento macroscopico di una stazione di rifornimento di idrogeno autonoma.

La prima fase della ricerca si concentra sullo sviluppo di un Ciclo di Guida rappresentativo per gli autobus di Modena (MBDC) attraverso un algoritmo di ottimizzazione metaeuristico ibrido che combina l'algoritmo MAX–MIN Ant System (MMAS) e l'algoritmo Artificial Bee Colony (ABC). Questo approccio ibrido ha dimostrato prestazioni superiori nella riproduzione dei dati di guida reali, migliorando significativamente le tecniche di modellazione stocastica convenzionali, come il metodo Markov Chain Monte Carlo (MCMC).

Nella seconda fase, sono state sviluppate e confrontate cinque diverse configurazioni di gruppo motopropulsore per autobus — Diesel, Gas Naturale Compresso (CNG), Ibrido Elettrico (HEB), Elettrico a Batteria (EB) e a Cella a Combustibile (FCB) — utilizzando l'ambiente di simulazione ADVISOR. I modelli convalidati sono stati successivamente testati utilizzando l'MBDC per valutare il loro consumo energetico e le loro prestazioni operative in condizioni di guida locali realistiche. Questo confronto ha rivelato notevoli discrepanze tra i cicli standardizzati e quelli derivati localmente, sottolineando l'importanza di test localizzati per una valutazione energetica accurata.

Infine, lo studio esplora la fattibilità di un'infrastruttura localizzata per l'idrogeno verde a supporto di una futura flotta di autobus a cella a combustibile (FCB) a Modena. Utilizzando scenari di domanda di idrogeno proiettati, derivati da dati operativi, è stata progettata una Stazione di Rifornimento di Idrogeno (HRS) concettuale e i suoi componenti principali sono stati dimensionati di conseguenza. È stato inoltre valutato il potenziale delle fonti di biomassa

regionali, tra cui la Frazione Organica dei Rifiuti Solidi Urbani (FORSU) e la biomassa legnosa, per la capacità di produzione locale di bio-idrogeno.

Complessivamente, la ricerca stabilisce un quadro integrato e scientificamente solido per il trasporto pubblico urbano sostenibile su autobus, collegando la generazione di cicli di guida reali, l'analisi comparativa dei gruppi motopropulsori e la progettazione di un'infrastruttura per l'idrogeno rinnovabile.

Nomenclature

Abbr.	*Definition*	*Abbr.*	*Definition*
A/C	Air Conditioning	*MANDC*	Manhattan Bus Cycle
ABC	Artificial Bee Colony	*MBDC*	Modena Bus Driving Cycle
ACO	Ant Colony Optimization	*MCMC*	Markov Chain Monte Carlo
ADVISOR	Advanced Vehicle Simulator	*MCT*	Monte Carlo Trial
APU	Auxiliary Power Unit	*MMAS*	MAX-MIN Ant System
BECCS	Bioenergy with Carbon Capture and Storage	*MPG*	Miles Per Gallon
BEV	Battery Electric Vehicle	*NEDC*	New European Driving Cycle
BRT	Bus Rapid Transit	*NiMH*	Nickel–Metal Hydride
CA	Clustering Analysis	*NPV*	Net Present Value
CBD-14	Central Business District	*NREL*	National Renewable Energy Laboratory
CNG	Compressed Natural Gas	*OAT*	One-at-a-Time
DTW	Dynamic Time Warping	*OBD-II*	On-Board Diagnostic
EB	Battery Electric Bus	*OCTA*	Orange County Bus Cycle
EPA	Environmental Protection Agency	*OFMSW*	Organic Fraction of Municipal Solid Waste
EPCU	Electric Pre-Cooling Unit	*PEBDC*	Patna Electric Bus Driving Cycle
ESS	Energy Storage System	*PEM*	Proton Exchange Membrane
FCB	Fuel Cell Bus	*PM*	Particulate Matter
FCREx	Fuel Cell Range-Extender	*PN*	Particle Number
FCV	Fuel Cell Electric Vehicle	*PSO*	Particle Swarm Optimization
GHG	Greenhouse Gas	*PSS*	Proportional Stratified Sampling
GIS	Geographic Information System	*PV*	Photovoltaic
GPS	Global Positioning System	*PVGIS*	Photovoltaic Geographical Information System
HICEV	Hydrogen Internal Combustion Engine Vehicle	*RMS*	Root Mean Square
HEB	Hybrid Electric Bus	*SETA*	Società Emiliana Trasporti Autofiloviari
HEV	Hybrid Electric Vehicle	*SMR*	Steam Methane Reforming
HP	High-Pressure	*SOC*	State of Charge
HRS	Hydrogen Refuelling Stations	*TCO*	Total Cost of Ownership
HVAC	Heating, Ventilation, and Air Conditioning	*TPM*	Transition Probability Matrix
ICE	Internal Combustion Engine	*UDDS*	Urban Dynamometer Driving Schedule
LCOH	Levelized Cost of Hydrogen	*VSP*	Vehicle Specific Power
LHV	Lower Heating Value	*WLTP*	Worldwide Harmonised Light Vehicles Test Procedure
LP	Low-Pressure		

Latin Symbols	***Definition***	***Latin Symbols***	***Definition***
a	Average Acceleration	P_{cr}	Time Percentage of Creeping Mode
A_v	Vehicle Frontal Area	P_d	Time Percentage of Deceleration Mode
C_D	Drag Coefficient	P_G	The Specific Power Required for a Vehicle to Ascend a Hill
$C_{HP,kg}$	HP Tank Size in Kg	$P_{HP,nom}$	HP Tank Storage Pressure
$C_{LP,kg}$	LP Tank Size in Kg	p_i	Food Source
C_p	Hydrogen Specific Heat	P_i	Time Percentage of Idling Mode
d	Average Deceleration	p_{ij}	The Likelihood that a Process Will Move from the s_i to s_j
D_a	Yearly Hydrogen Demand	P_{in}	Compressor Inlet Pressure
D_d	Daily	p_{new}	New Food Source
$D_{day,worst}$	Worst Case (A/C on) Daily Hydrogen Demand	P_{out}	Compressor Outlet Pressure
DD_{H_2}	Daily Dispensed Hydrogen	PR	Effective Pressure Ratio
$E_{comp,year}$	Annual Electricity Requirement of the Compressor	$Prob_i$	Probability that Onlooker Bee Chooses Source i
$E_{comp,year,kg}$	Compressor Energy Demand per Kilogram of Hydrogen Dispensed	Q	Update Constant
$E_{PCU,spec}$	PCU Energy Consumption	R	Universal Gas Constant
E_{step}	Hydrogen Compression Energy	r_d	Wheel Radius
F_{cg}	Gasoline-Equivalent Fuel Consumption	s_i	Past State
f_d	Total Gear Ratio	s_j	New State
F_D	Drag Force	SF_{HP}	Tank Sizing Safety Factor
Fit	Fitness	t	Time
g	Gravity	T	Gas Temperature
$H_{2,yearly}$	Yearly Hydrogen Consumption of the Fleet	T_{amb}	Ambient Temperature
k_d	Daily Driving Distance of a Single Bus	T_{brk}	Braking Torque
L_B	Lower Bound	$\bar{T}_d$	Daily Ambient Temperature
m	Gas Mass	T_h	Compressor Inlet Temperature
$\dot{m}_{hydrogen}$	Mass Flow Rate of Hydrogen	T_{HP}	Average Storage Temperature for the HP tank
m_v	Vehicle Mass	T_{LP}	Average Storage Temperature for the LP tank
n_a	Number of Positive Acceleration	T_o	The Torque Delivered by the Powertrain
N	Total Count of all GPS Records	U_B	Upper bound
N_{bus}	Number of Bus	V	Volume
n_d	Number of Negative Acceleration	v_a	Average Speed
N_r	The Number of Speed Data where the Vehicle is in Motion	V_{HP}	HP Tank Storage Volume
N_s	The Total Number of Unique States	v_r	Average Running Speed

P	Pressure	v_v	Vehicle Speed
P_a	Time Percentage of Acceleration Mode	w_{spec}	Specific Work Required to Compress 1 Kg of Hydrogen
p_{best}	Best Solution	X_t	Value of a Random Variable at a Given Time t
P_c	Time Percentage of Cruising Mode	Z	Compressibility Factor for Hydrogen
P_{comp}	Compressor Power		

Greek Symbols	***Definition***	***Greek Symbols***	***Definition***
α	Influence of the Pheromone	κ	Adiabatic Index
α_{hist}	Specific Weight for the Histogram Error	ρ	Pheromone Evaporation Rate
α_{road}	Road Angle	ρ_{air}	Air Density
β	Impact of the Heuristic Element	τ_{ij}	Pheromone that has Collected on the Route from State i to j,
$\gamma_{distance}$	Weighting Factor for the Distance Error	$\tau_{ij}^{(0)}$	The Initial Pheromone Value
Δm	Percentage Error	τ_{max}	Upper Pheromone Limit
η	Adiabatic Efficiency	τ_{min}	Lower Pheromone Limit
η_d	Final Drive Efficiency	ϕ	Random Scalar between -1 and 1
η_{ij}	Heuristic Desirability Factor		

1. INTRODUCTION

1.1. Global Energy Context and Emissions

As the world's population expands and technology continues to advance, energy needs are rising steadily. In 2024, global energy consumption grew by 2.2%, with transportation playing a major role in this upward trend [1]. The sector's rising energy use is closely tied to the expanding global vehicle fleet, which reached 1.7 billion units in 2023 and is projected to grow to 2.9 billion by 2050. According to the International Energy Agency, transportation is responsible for roughly 24% of all CO_2 emissions originating from fuel combustion [2]. Between 1990 and 2022, emissions from the transport sector grew at an average rate of 1.7% per year, making it one of the fastest-increasing sources of global greenhouse gases and placing it on a trajectory comparable to that of the industrial sector. Trucks and buses represent less than 8% of the global vehicle stock (excluding two and three wheelers), but they are responsible for more than 35% of direct CO_2 emissions from road transport [3].

Although the adoption of hybrid-electric, fuel cell, and fully electric vehicles has been steadily rising [4], internal combustion engine (ICE) vehicles remain dominant in global transportation. ICEs continue to be favored due to their ease of operation and rapid refuelling [5] and despite substantial technological improvements, their dependence on fossil fuels still drives significant greenhouse gas emissions and contributes to ongoing climate change. Burning fossil fuels has well-documented negative health impacts, particularly for children, contributing to cognitive impairments as well as higher rates of respiratory and long-term diseases. These risks are most acute in low-income urban areas where aging, high-emission vehicle fleets dominate, underscoring a clear case of environmental injustice [6]. Growing awareness of these issues is accelerating the worldwide transition toward electric mobility. When the operational emissions of ICE vehicles are assessed together with their full life-cycle impacts, both battery electric vehicles (BEVs) and fuel cell electric vehicles (FCVs) demonstrate a strong capacity to significantly lower global emissions [7,8].

1.2. Powertrain Technologies in Transportation

Diesel engines are widely used in heavy-duty transport and industrial settings due to their durability and relatively high fuel efficiency. However, their elevated emissions of nitrogen oxides and particulate matter continue to pose major environmental and public-health challenges, underscoring the need for further advancements in emission-control technologies [9]. Compressed natural gas (CNG) presents several notable advantages over diesel, particularly

in terms of environmental performance and operating costs. CNG burns more cleanly, producing substantially lower levels of nitrogen oxides and particulate matter, both of which are key contributors to air pollution and respiratory illnesses. It also results in reduced carbon dioxide emissions per unit of energy, helping mitigate greenhouse gas impacts. Economically, CNG is frequently less expensive than diesel, offering operators meaningful savings in fuel expenditures [10]. These combined benefits make CNG an attractive alternative for urban fleets where air-quality considerations are especially important.

A hybrid electric vehicle (HEV) operates by drawing on multiple onboard energy storage systems. In most conventional designs, one of these energy sources is a liquid fuel such as gasoline or diesel, which is converted into mechanical or electrical power through an internal combustion engine. The second source is an electrical energy storage unit. Contemporary HEVs integrate a range of advanced technologies aimed at boosting overall efficiency. One key feature is regenerative braking, which captures a portion of the vehicle's kinetic energy during deceleration and converts it into electricity to recharge the battery, rather than allowing that energy to dissipate as heat. In addition, certain HEV architectures use the internal combustion engine to power a generator, supplying electricity when needed [11]. Many hybrid models are also equipped with start-stop functionality that shuts down the engine during idling, lowering fuel use and pollutant emissions. These vehicles typically rely on sophisticated control strategies that coordinate the interaction between the electric drivetrain and the combustion engine, enabling higher fuel economy and a reduced environmental footprint.

BEVs rely solely on electricity stored in onboard batteries, which allows them to operate without producing any tailpipe emissions. As a result, they eliminate the release of major air pollutants such as carbon dioxide, nitrogen oxides, and particulate matter which are the substances closely linked to deteriorating air quality and global warming. When these vehicles are charged using energy generated from renewable sources, their environmental advantages increase even further, since the overall dependence on fossil-based electricity is reduced.

FCVs derive their propulsion power from onboard fuel cells. Although several fuel cell technologies exist, most FCVs rely on proton exchange membrane fuel cells, which convert the chemical energy of hydrogen directly into electricity. In several respects, FCVs offer advantages over battery-electric vehicles. Their powertrain components are typically lighter and more compact, contributing to lower overall vehicle mass and reduced greenhouse gas impacts. During operation, FCVs emit neither carbon monoxide, carbon dioxide, nor nitrogen oxides, and instead release only water vapor and heat. Additionally, the overall drivetrain architecture

is simpler, operates more quietly, and achieves higher efficiency levels than conventional ICE-based systems [12]. Even so, the substantial upfront cost of FCVs and the limited availability of hydrogen refuelling stations have prevented their widespread adoption. According to data from the Advanced Fuel Cells Technology Collaboration Programme, the global fleet of FCVs reached 97,356 units by the end of 2024. South Korea stands out as the leading market, accounting for 36% of all vehicles in operation. Most of the global fleet consists of passenger cars, which make up 69%, while heavy-duty trucks represent 12% and buses about 9% [13].

1.3. Operational Challenges in Urban Bus Fleets

Urban mobility systems rely on a range of high-capacity transport modes, and the required investment varies considerably, generally starting with buses at the lower end and increasing for trolleybuses, bus rapid transit systems, trams, and finally metro lines [14]. Buses constitute a major share of public transport fleets. It is well established that differences in operating conditions, such as road gradients or the number of stops, along with vehicle-specific attributes including auxiliary power demands or structural design, exert a strong influence on fuel consumption. This underscores the importance of accounting for these factors when selecting buses for passenger services [15]. Persistent issues in vehicle optimization involve elevated fuel use, degradation of key components, and the development of effective energy management approaches. In addition, vehicle performance is highly dependent on external influences including roadway characteristics, passenger load, and driving style. Optimizing hybrid electric buses (HEB) and fuel cell buses (FCB) requires careful coordination of energy efficiency, battery lifespan, and hydrogen usage, while battery electric buses (EB) continue to face constraints related to battery aging and the capacity of charging infrastructure.

1.4. The Challenge of Representative Driving Cycles

The energy consumption patterns and emission levels of road vehicles are largely dictated by the distinctive driving habits associated with a particular region, and these behaviours are typically captured through driving cycles [16,17]. A driving cycle is generally described as a time series of vehicle speeds that characterizes the prevailing driving style of a specific location [18]. Differences in vehicle operation across varying conditions have resulted in the development of distinct driving cycles tailored to particular vehicle categories. In many developing countries, where local driving cycles are not available, type-approval procedures often rely on widely used standardized cycles, including the New European Driving Cycle (NEDC) and the Worldwide Harmonised Light Vehicles Test Procedure (WLTP) [2,19].

However, many research demonstrates that fuel economy values derived from controlled laboratory tests using these standardized cycles tend to overestimate real-world efficiency, resulting in a considerable gap between certified performance and actual on-road fuel use [2].

Given the increasing abundance of large-scale Global Positioning System (GPS) trajectory datasets, the importance of producing representative driving cycles remains significant. While extensive data collections are invaluable for examining historical fleet behaviour, they serve a different purpose than representative cycles. Custom-designed driving cycles are indispensable whenever reproducible and standardized conditions are required, such as in precise evaluations of energy consumption, assessments of emerging vehicle technologies or transport strategies, and the need for simplified yet reliable input data for powertrain modelling and design [19,20]. Consequently, the development of a localized driving cycle, as undertaken in this study, constitutes a fundamental component of predictive modelling and comparative analysis, offering capabilities that cannot be achieved solely through retrospective data examination.

1.5. Research Methodology and Scope of the Study

This study responds to well-known shortcomings of standardized driving cycles, which frequently fail to capture the unique characteristics of local driving patterns. The initial phase of the research focuses on constructing a bus driving cycle tailored specifically to the urban conditions of Modena, Italy, enabling more reliable estimates of regional energy consumption and emissions. To create these cycles, two different stochastic optimization approaches were employed: the Markov Chain Monte Carlo (MCMC) method and a newly developed hybrid framework that combines the MAX-MIN Ant System (MMAS) with the Artificial Bee Colony (ABC) algorithm, referred to in this work as the MMAS-ABC approach. We introduce this hybrid algorithm as an original contribution to computational intelligence. Although some prior studies have experimented with integrating the classical Ant Colony Optimization (ACO) technique with ABC in various contexts [21–23], the possibility of coupling ABC with more advanced ACO variants has received virtually no attention. This research fills that gap by presenting, to the best of our knowledge, the first integration of the MMAS with the ABC algorithm.

The resemblance between the generated driving cycles and the original dataset is evaluated by examining core performance indicators, the distributions of speed and acceleration, and the overall trip distances. The main innovations and contributions of this part can be summarized as follows:

- Creation of a Localized Bus Driving Cycle for Modena: This study delivers the first driving cycle tailored specifically to urban bus operations in Modena, constructed through established stochastic techniques, including MCMC and bio-inspired optimization methods.
- Introduction of a Hybrid MMAS-ABC Framework for Driving Cycle Synthesis: A new hybrid computational approach is presented that combines the MAX-MIN Ant System with the Artificial Bee Colony algorithm, providing a more accurate and resilient method for producing representative driving cycles.
- Integration of Empirical GPS Data for Greater Realism: In contrast to standardized or artificially generated cycles, the cycles developed in this research are grounded in real GPS trajectories, enabling them to reflect authentic patterns of acceleration, deceleration, stop-and-go motion, and speed variations typical of dense urban environments
- Transferable Methodological Framework: The workflow established here can be adapted for constructing representative driving cycles in other cities or regions.

Once the cycles were generated, the study carried out an extensive evaluation to compare fuel consumption and hill-climbing capability across multiple bus technologies under realistic operating conditions. This involved:

- Comparing the fuel use of diesel, CNG, hybrid electric, battery electric, and fuel cell buses, and examining how air-conditioning loads influence consumption.
- Investigating how variations in bus mass (due to passenger load or different power units), aerodynamic drag coefficient, and wheel diameter affect fuel consumption across vehicle types.
- Assessing fuel consumption on roads with different incline levels.
- Performing gradeability tests to quantify the hill-climbing performance of each bus.

Building on these evaluations of vehicle-level performance under real-world driving conditions, the research then extends its scope to infrastructure planning for sustainable public transport. It presents an initial simulation and assessment of a hydrogen refuelling station integrated with local biohydrogen production in Carpi, Italy. The system incorporates two biomass resources, the organic fraction of municipal solid waste and woody residues to estimate their combined capacity to supply hydrogen for an urban fuel cell bus fleet.

2. LITERATURE REVIEW

2.1. Literature Review on Driving Cycle Construction Methods

A high amount of research on the generation of driving cycles has emerged recently, exploring various methodologies for a range of applications. For instance, Keskin et al. [24] employed a combination of MCMC simulations and the dynamic time warping (DTW) technique to construct a driving cycle for Iğdır, Türkiye. Their approach utilized the MCMC method to generate candidate cycles and DTW to select the most suitable one, based on speed-time data gathered from 19 trips via an on-board diagnostic II (OBD-II) device. They reported that this hybrid MCMC and DTW approach yields highly precise results. Similarly, Bishop and Axon [25] developed candidate driving cycles using a Markov chain method, which was applied to a dataset spanning 1142 km of driving data collected from various drivers using both GPS and OBD equipment. In another study, Cui et al. [2] put forward a hybrid methodology combining MMAS and the Markov Chain for driving cycle generation. Using 130 hours of passenger car trajectory data obtained through the chase-car method in Fuzhou, China, they discovered that their approach could improve the representativeness of the resulting cycle by up to 29.9% over conventional techniques, including clustering, micro-trip, and standard Markov chain methods. Arun et al. [26] utilized data from eight distinct trips, recorded with a GPS and an OBD reader, to generate a driving cycle based on micro-trips for cars and motorcycles in Chennai, India. Focusing on two-wheelers, Gurusamy and Ashok [27] developed a driving cycle in Vellore, India, by applying k-means clustering to micro-trips. Their dataset consisted of 60 hours of recordings from 42 separate trips, captured using both a chase car and onboard instruments, and they subsequently validated the generated cycle by comparing its driving patterns against the original measurements. Mafi et al. [28] constructed local driving cycles for Tehran, Iran, also using the k-means clustering of micro-trips method on an extensive dataset of over 36000 km (950 hours) collected via OBD-II. Their results indicated that the custom-developed cycles enabled a more precise assessment of real-world average CO_2 emission levels when compared to the standardized NEDC and WLTC cycles.

The creation of driving cycles specifically for public transportation has been a less explored area within the existing body of research [19]. For example, Tong and Ng [19] utilized data from 91 bus trips collected via smartphone GPS in Hong Kong. After affirming the reliability of mobile GPS for this purpose, they formulated a driving cycle using a micro-trip-based approach. The representativeness of the final cycle was then verified by comparing it against the source data across 13 evaluation metrics, such as vehicle specific power (VSP) and speed-

acceleration probability distributions. In a separate study, Tong [29] developed a driving cycle for a specific Hong Kong bus route serviced by supercapacitor buses. Based on speed-time data from 12 trips gathered with a smartphone GPS application, a new cycle was generated using a micro-trip method, with VSP employed to determine the ideal driving pattern. It was observed that the resulting cycle's characteristics were significantly different from other bus driving cycles reported in the literature. In South Africa, Hull et al. [30] applied a combination of clustering analysis (CA) and DTW methods to create a representative driving cycle for a paratransit vehicle in Stellenbosch. Their methodology involved an integration of DTW with mixed integer programming to classify micro-trips of different lengths based on their time-series patterns. The construction was based on data from 62 trips involving 40 different drivers, recorded by an onboard GPS device, and ultimately, the performance metrics of the generated cycle deviated from the measured data by less than 10%.

Further research includes the work of Shen et al., [31] who constructed a new driving cycle for a HEB in Shanghai by applying the k-means clustering method to 14 driving samples. They also introduced a novel approach that involved segmenting the driving data based on bus station locations to account for the frequent stops of bus routes. In India, Pandey et al. [32] created the Patna Electric Bus Driving Cycle (PEBDC) by employing k-means clustering on micro-trips derived from 650 km of GPS data, with a comparative evaluation revealing substantial differences from established international bus cycles. For Bus Rapid Transit (BRT) vehicles in Istanbul, Kaymaz et al. [33] utilized the Proportional Stratified Sampling (PSS) method, recording four trips via OBD-II and classifying micro-trips into four speed levels to generate a cycle with less than 10% relative error. Using a large dataset of 371 bus trips in Hanoi, Vietnam, Nguyen et al. [34] applied a Markov chain approach, validating their cycle's accuracy by comparing its speed-acceleration frequency distribution with the original data. Finally, to assess the energy consumption of battery electric buses, Kivekäs et al. [35] developed synthetic driving cycles for a route in Espoo, Finland, by implementing a novel segment-based method on data from 24 trips. A consolidated summary of the studies examined in this review is presented in Table 2.1.

Table 2.1. A Summary of Investigated Studies on Driving Cycle Construction

Ref.	Year	Construction Method	Data Scale	Acq. Method	Location	Vehicle Type
[24]	2025	MCMC and DTW	19 trips	OBD-II	Iğdır, Türkiye	Passenger Car

[25]	2024	Markov Chain	1142 km	OBD-GPS	London & Cambridge, UK	Passenger Car
[2]	2022	MMAS and Markov Chain	130 hours	Chase car	Fuzhou, China	Passenger Car
[26]	2017	Random Micro-Trip Selection	8 trips	OBD-GPS	Chennai, India	Passenger Car & Motorcycle
[27]	2024	K-Means Clustering of Micro-Trips	42 trips	OBD-GPS	Vellore, India	Two-Wheeler
[28]	2022	K-Means Clustering of Micro-Trips	36000 km	OBD-II	Tehran, Iran	Passenger Car
[19]	2021	Random Micro-Trip Selection	91 trips	GPS	Hong Kong	Bus
[29]	2019	Random Micro-Trip Selection	12 trips	GPS	Hong Kong	Bus
[30]	2024	Micro-Trip Clustering and DTW	62 trips	GPS	Stellenbosch, South Africa	Paratransit
[31]	2018	K-Means Clustering	14 trips	OBD	Shanghai, China	Bus
[32]	2023	K-Means Clustering of Micro-Trips	650 km	GPS	Patna, India	Bus
[33]	2019	PSS	4 trips	OBD-II	Istanbul, Türkiye	BRT
[34]	2019	Markov Chain	371 trips	GPS	Hanoi, Vietnam	Bus
[35]	2018	Novel Segment-Based Method	24 trips	Online DAQ System	Espoo, Finland	Bus

The literature reveals a variety of techniques for constructing driving cycles, each possessing its own merits and limitations. According to Hull et al. [30], these generation techniques can be classified into five main categories: MCMC-based, optimization-based (e.g., Genetic Algorithm or MMAS), clustering analysis, segment-based, and random selection-based models. Among these approaches, studies such as Tong and Ng [19] highlight that the field is predominantly governed by two principal methodologies: stochastic state-transition models, like MCMC, and approaches based on micro-trips, which often involve clustering or random selection. While micro-trip-based techniques are advantageous due to their relative simplicity, they encounter significant difficulties in generating representative driving cycles, particularly for buses. The operational variability and frequent stops characteristic of bus routes result in a wide array of micro-trips, which not only increases the computational effort for synthesis but can also lead to the failure to capture critical driving events like severe braking [30,31,36]. In contrast, the MCMC method is noted for its powerful stochastic framework and its effectiveness in preserving the temporal sequence of driving data. Nevertheless, this approach has its own

limitations, including a typical requirement for extensive datasets to function effectively and the potential for producing inconsistent outcomes [19,30].

2.2. Literature Review on Vehicle Modelling and Performance Comparison

A great number of research has focused on analysing vehicle performance and fuel economy across different propulsion technologies through both simulation-based and experimental approaches. Such comparative investigations offer critical insights into the operational advantages and limitations of each vehicle category. For instance, Durkin et al. [37] utilized the quasi-static simulation toolbox in MATLAB/Simulink to evaluate hydrogen consumption in a FCV and a hydrogen internal combustion engine vehicle (HICEV). Their analysis under the WLTC revealed that the FCV achieved markedly higher efficiency, consuming merely 1.05 kg of hydrogen per 100 km, while the HICEV required approximately 1.79 kg-H_2 per 100 km. Similarly, Gautam et al. [38] compared ICE vehicles with HEVs under the Urban Dynamometer Driving Schedule (UDDS), concluding that HEVs exhibit greater fuel efficiency than their conventional counterparts. They further emphasized the potential of HEVs to benefit transportation sectors in developing and emerging economies. Dogdu and Reyhancan [39] performed a comparative assessment of fuel consumption and CO_2 emissions between a series-hybrid vehicle and a conventional gasoline vehicle, considering both the NEDC and the WLTC. Their study showed that incorporating a downsized ICE within the series-hybrid configuration yielded a 3.3% reduction in fuel consumption on the NEDC compared to the traditional gasoline setup. Likewise, Díaz et al. [40] investigated energy usage within urban bus networks, examining the substitution of ICE buses with EBs. Using real-world GPS data, topographical maps, and a quasi-static longitudinal modelling framework, they assessed multiple city routes with varying gradients. Their findings demonstrated that deploying EBs on an optimized route could cut overall energy consumption by up to 68%. Keegan et al. [41] employed the Advanced Vehicle Simulator (ADVISOR) simulation tool to model a range of vehicles, including four ICE vehicles, two parallel HEVs, and two series HEVs. Each vehicle was configured with distinct engine capacities, transmission types, and electric motor ratings. Their comparative evaluation across multiple driving cycles indicated that an ICE vehicle with a 1.9 L engine and automatic transmission consumed 44 L/100 km, whereas a 1.0 L manual counterpart achieved a lower rate of 30.3 L/100 km under identical conditions. Moreover, the study highlighted the substantial fuel-saving potential of hybrid configurations; for example, a series HEV equipped with a 1.0 L engine and 200 nickel–metal hydride (NiMH) battery modules demonstrated a notably low fuel consumption of 6.65 L/100 km. Molina et al. [42] investigated a novel Fuel Cell Range-

Extender (FCREx) architecture, focusing on the optimization of powertrain design parameters such as fuel cell power rating, battery capacity, and hydrogen storage. Through simulation-based energy management optimization, they demonstrated that the FCREx configuration can achieve hydrogen consumption reductions ranging from 16.8% to 25% compared to commercial FCVs. Their results also identified an ideal balance between cost and efficiency, favouring a setup with around 30 kWh of battery capacity and at least 80 kW of fuel cell output. Kim et al. [43] performed a techno-economic comparison between EBs, FCBs, and traditional diesel buses within the context of small to mid-sized urban areas. Using a Total Cost of Ownership (TCO) framework, they projected that by 2030, EBs would achieve a 23.5% lower TCO compared to diesel buses, whereas FCBs would still have a 15.4% higher TCO, despite offering extended range and refuelling convenience. Nevertheless, under a scenario where hydrogen costs decline to €5/kg due to large-scale infrastructure deployment, the FCB's TCO could potentially fall below that of diesel buses, marking a key inflection point for economic feasibility.

In addition to these studies, extensive research has been devoted to understanding the environmental implications of various vehicle technologies, focusing particularly on emissions and energy consumption. Investigations have explored these impacts under different operational scenarios and conditions. For example, Luu et al. [44] performed a comprehensive life cycle impact analysis comparing conventional and electric buses. Their results indicated that EBs outperform traditional ones across multiple environmental indicators such as greenhouse gas (GHG) emissions, fine particulate matter formation, and acidification over the full vehicle lifespan. Furthermore, their study estimated that transitioning from conventional buses to electric alternatives in Vietnam could cut the carbon footprint by roughly 42.62 gCO_2 per passenger kilometre. Muñoz et al. [45] assessed the economic, energetic, and environmental performance of urban buses powered by diesel, natural gas, hydrogen, and electricity. Their analysis showed that a nationwide replacement of Argentina's diesel bus fleet with FCBs could yield a reduction of about 1.3 Mt in CO_2-equivalent emissions, corresponding to an 87% drop in GHG output. Meanwhile, adopting EBs would potentially lower overall energy usage by 25–38% and emissions by 52–61%, resulting in the avoidance of around 0.93 Mt of CO_2-equivalent emissions annually. Shahariar et al. [46] investigated how driving behaviour and traffic flow influence emissions and fuel consumption under real-world transient driving cycles, utilizing both diesel and diesel–biodiesel blends. Their findings revealed that aggressive driving markedly increased CO_2, NO_x, and CO emissions by up to 37%, 38%, and 88%, respectively.

Furthermore, the particulate matter (PM) and particle number (PN) levels rose even more steeply, by 112% and 538%. The study also found that biodiesel significantly mitigated PM and PN emissions, by 71% and 68%, regardless of driving aggressiveness. Additionally, congestion during peak hours notably amplified fuel consumption, highlighting the sensitivity of efficiency to traffic conditions. Ahmadi et al. [47] conducted a comprehensive life-cycle assessment comparing diesel, diesel-hybrid, and fuel cell bus technologies. Their findings confirmed that FCBs outperform other configurations in terms of environmental sustainability. The research also revealed that battery degradation plays a decisive role in long-term performance and that fuel consumption in FCBs is particularly sensitive to variations in passenger load more than in diesel or hybrid counterparts.

The influence of road gradient on vehicle fuel economy, emissions, and climbing capability has also been widely addressed in the literature. These studies collectively emphasize the operational challenges introduced by sloped roadways. De Almeida and Kruczan [48] analysed the Toyota Mirai FCV using ADVISOR software to evaluate how varying hybridization ratios impact performance. Their results indicated that increasing the hybridization ratio reduces maximum gradeability while simultaneously enhancing acceleration. Jiang et al. [49] examined the effect of road gradients ranging from −5% to +5% on diesel vehicle fuel consumption. The most pronounced rise occurred between +3% and +4% gradients; at +4% and a speed of 80 km/h, consumption was found to be 1.4 and 1.52 times higher than at 60 km/h and 40 km/h, respectively. Posada-Henao et al. [50] further developed a fuel consumption model for heavy-duty diesel trucks subjected to varying inclines. They observed that a fully loaded truck (52 tons) consumed significantly more fuel than an unloaded one (19 tons), with consumption 2.92, 2.73, and 2.29 times greater on 7%, 5%, and 2% slopes, respectively. KoteswaraRao K et al. [51] employed the ADVISOR to simulate a Toyota Mirai and explore how variations in powertrain component dimensions affect fuel economy and driving performance under multiple test cycles. Their investigation revealed an optimal configuration wherein downsizing the fuel cell stack from 114 kW to 80 kW, coupled with expanding the battery module count from 37 to 75, produced notable improvements in both energy efficiency and gradeability. However, they also identified a performance threshold. Further reductions in stack size beyond this optimal point inversely increased hydrogen consumption, underscoring the sensitivity of system balance.

Collectively, the reviewed studies summarized in Table 2.2 highlight major advancements in evaluating diverse vehicle technologies. They provide a comprehensive understanding of the

interrelationships between propulsion types, fuel economy, emissions, and operational costs under varied driving conditions and topographical environments.

Table 2.2. A Summary of Examined Studies on Vehicle Modelling

Ref.	Year	Key Findings
[15]	2024	The study highlighted that aligning bus types with route-specific characteristics such as gradient and expected fuel use is crucial to optimizing operational performance.
[37]	2024	The comparison revealed hydrogen consumption rates of 1.05 kg-H_2/100 km for the FCV and 1.79 kg-H_2/100 km for the HICEV, demonstrating the superior efficiency of the fuel cell configuration.
[38]	2021	HEVs exhibited notably greater fuel efficiency compared to their conventional counterparts.
[39]	2024	Incorporating a downsized ICE into a series-hybrid architecture improved overall fuel economy by approximately 3.3% relative to a standard gasoline-powered vehicle.
[40]	2024	Transitioning to EBs along optimized routes could yield an energy consumption reduction of nearly 68%.
[41]	2024	Substantial reductions in fuel consumption can be achieved through the implementation of HEV technology.
[44]	2022	EBs were favored in various environmental impact categories throughout their life cycle.
[45]	2022	Replacing conventional fleets with FCBs could achieve an 87% cut in GHG emissions, while EBs may reduce energy demand by 25–38% and emissions by 52–61%.
[46]	2022	Aggressive driving behaviour was observed to cause sharp increases in CO_2, NO_x, and CO emissions.
[48]	2021	Increasing the hybridization ratio enhanced vehicle acceleration capabilities but simultaneously diminished gradeability performance.
[49]	2025	Fuel usage rose sharply when the road gradient increased from +3% to +4%; at +4% and 80 km/h, consumption was 1.4 and 1.52 times greater than at 60 km/h and 40 km/h, respectively.
[50]	2023	A fully loaded diesel truck (52 tons) consumed significantly more fuel than an unloaded one (19 tons), with consumption rising by factors of 2.92, 2.73, and 2.29 at slopes of 7%, 5%, and 2%, respectively.
[42]	2021	The FCREx configuration cut hydrogen use by 16.8–25% and achieved ideal efficiency with 30 kWh battery + ≥80 kW fuel cell.
[43]	2021	EBs may achieve 23.5% lower TCO by 2030, while FCBs could become cost-competitive if hydrogen falls to €5/kg.
[51]	2024	Optimal downsizing of the fuel cell stack (114 → 80 kW) with increased battery modules improved efficiency; further downsizing led to higher hydrogen use.
[47]	2022	FCBs showed superior environmental performance; battery aging and passenger load strongly influenced efficiency.

2.3. Literature Review on Hydrogen Production and Utilization for Public Transport

In the recent years, many papers have been published focusing the generation of hydrogen with different methods for the hydrogen refuelling stations. Majority of these studies investigated the green hydrogen production. Navas-Anguita et al. [52] evaluated the technological, economic, and environmental performance of a national hydrogen production strategy using an energy system modelling framework that incorporates dynamic carbon emission metrics. Their scenario-based analysis compared conventional fossil-dependent production with low-carbon alternatives. Findings indicated that natural gas reforming remains the dominant method in the near term, while water electrolysis gradually becomes the key pathway in later decades. Under stricter emission constraints, biomass gasification also gains importance. Moreover, the large-scale replacement of fossil fuels with hydrogen in road transport was projected to reduce GHG emissions 36 and 58 million tonnes of CO_2-equivalent by 2050. Ayodele et al. [53] investigated the techno-economic feasibility of wind-powered hydrogen refuelling stations across seven South African cities. The proposed system was designed to supply hydrogen for 25 vehicles per day, each with a 5 kg storage capacity. The analysis began with an evaluation of regional wind resources to determine local energy potential, followed by an assessment of economic performance and emission reduction capability. Results indicated that coastal cities possess favourable conditions for establishing on-site wind-based hydrogen refuelling facilities, offering hydrogen production costs competitive with international benchmarks. The authors also suggested future comparative studies between distributed on-site and centralized hydrogen production models, alongside the integration of other renewable resources such as solar, hydrokinetic, and biomass energy. Chrysochoidis-Antsos et al. [54] examined the feasibility of integrating wind turbines near existing fuel stations to generate hydrogen for both fuel cell vehicle refuelling and injection into local gas networks. A Geographic Information System (GIS) based spatial assessment was employed to identify suitable station locations, incorporating safety, infrastructure, and ecological constraints through buffer zone analysis. Findings revealed that approximately 4.6% of current fuelling stations meet the necessary siting criteria. Subsequent evaluations using meteorological and land-use datasets estimated the hydrogen production capacity of these sites, indicating that under a 30% FCV penetration scenario, they could supply about 2.3% of the projected hydrogen demand. A complementary case study further explored the integration potential of these stations with nearby gas distribution systems. Guerra et al. [55] evaluated the techno-economic feasibility of on-site hydrogen production for a dedicated fleet of 20 hydrogen-powered trains, employing a proton

exchange membrane (PEM) electrolyser technology. A sensitivity analysis is conducted to understand the influence of key factors, including electricity prices, hydrogen market value, operational hours, and fleet size, on overall project viability. The assessment methodology relies on net present value (NPV) calculations, supplemented by standard sensitivity analysis performed using Oracle Crystal Ball. Findings indicate that hydrogen-powered trains represent a sustainable and economically attractive alternative, offering environmental benefits while maintaining operational safety. Bahou [56] investigated Morocco's green hydrogen prospects by evaluating a hydrogen refuelling facility powered by a photovoltaic system connected to the electricity grid. The station is planned to meet the needs of a local taxi fleet, exploring scenarios in which conventional taxis are replaced by FCVs. To determine the station's infrastructure requirements, a model was developed to forecast daily hydrogen consumption. Economic feasibility was assessed by calculating production costs for different station capacities. Findings reveal that covering the entire taxi fleet would demand roughly 152 kg of hydrogen per day, whereas supplying 20% of the fleet would require only 30.4 kg. Additionally, the analysis shows that hydrogen costs decrease with increased station capacity, ranging from $12.56/kg for smaller stations to $9.18/kg for larger ones. This study highlights that appropriately scaled photovoltaic (PV) powered hydrogen stations could offer a viable, cost-effective, and environmentally sustainable alternative to conventional fossil-fuelled urban transport. Gökçek et al. [57] evaluated on-site hydrogen refuelling stations powered by hybrid renewable energy systems in Niğde, Türkiye, and Zaragoza, Spain, using HOMER software. Different system configurations were analysed to supply 24 vehicles daily. Results indicate that solar-based systems are most suitable for Niğde, while combined wind and solar systems perform best for Zaragoza. They also mentioned that utilizing renewables for hydrogen production can significantly reduce CO_2 emissions and support sustainable transportation, contributing to the broader adoption of FCVs. Caponi et al. [58] presented an optimization algorithm designed to find the most cost-effective hydrogen price for scalable refuelling stations that utilize grid-connected electrolysis systems. The model works by analysing the relationships between equipment investment costs, electricity prices, and the specific hydrogen demands of various FCB capacities. Additionally, sensitivity and comparative analyses were performed to define cost boundaries and to benchmark FCB refuelling against EB charging. The study concludes that while hydrogen is not currently cost-competitive, future advancements in electrolyser technology combined with lower electricity prices could significantly reduce the levelized cost of hydrogen (LCOH), making it more economically viable compared to battery-electric options. Bartolucci et al. [59] proposed a framework for a multi-hub hydrogen refuelling network

designed to support a bus system in the Lazio region. The framework integrates two production methods: photovoltaic-powered electrolysis and centralized steam methane reforming (SMR). To assess operational efficiency, every component of the station, from the solar arrays to the storage and dispensing units, was modelled in MATLAB/Simulink. A sensitivity analysis indicated that larger hubs can significantly decrease the levelized cost of hydrogen by up to 40%. The study also found that this combined electrolysis/SMR approach can maintain relatively low carbon emissions.

Focusing on hydrogen generation from biomass, Rosa and Mazzotti [60] analysed hydrogen production from biomass within a bioenergy with carbon capture and storage (BECCS) framework, emphasizing its dual potential to deliver low-carbon hydrogen and achieve carbon dioxide removal. Their spatially resolved assessment for Europe showed that sustainable biomass resources, such as agricultural residues and waste, could support annual production of up to 12.5 Mt of hydrogen while capturing approximately 133 Mt of CO_2, highlighting BECCS as a near-term pathway for negative-emission hydrogen generation. Cormos [61] evaluated decarbonized hydrogen production through biomass gasification integrated with CO_2 capture, highlighting its potential as a negative-emission energy pathway. The study demonstrated that such systems could achieve conversion efficiencies around 57–59% with relatively low energy and cost penalties, while membrane-based CO_2 separation showed superior techno-economic performance compared to absorption-based methods. Andrea et al. [62] performed a techno-economic assessment of hydrogen production for small-scale refuelling stations, focusing on the Rome case study. The analysis compared alkaline electrolysis, biomass gasification, and hydrogen delivery systems through a sensitivity study on the LCOH for production capacities up to 400 kg/day. Results showed that biomass gasification achieved the lowest LCOH (≈5.99 €/kg) compared to electrolysis (≈12.7 €/kg), with both technologies exhibiting cost stabilization beyond specific operating hours. The integration of existing infrastructure in the Rome station design further reduced hydrogen costs, indicating the economic advantage of hybrid production approaches. Martins et al. [63] examined various biomass gasification pathways for green hydrogen production, comparing conventional, plasma, and supercritical water processes through Aspen Plus simulations and economic analyses. Their findings indicated that supercritical water gasification achieved the highest hydrogen yield, while conventional gasification showed potential economic feasibility under specific operating conditions. Despite current cost limitations, the study emphasized that process optimization could substantially improve the viability of biomass-based hydrogen production. Lastly, Tang et al. [64] introduced

a hybrid electrocatalytic configuration in which biomass-derived carbohydrates are selectively converted into formic acid while hydrogen is co-generated through water reduction. The system employs polyoxometalates to facilitate the oxidation reaction, achieving a formic acid yield of 62.5% and a Faradaic efficiency near 100%, with continuous hydrogen output maintained at a low operating voltage of 1.22 V, offering a promising strategy for integrated and energy-efficient hydrogen production from biomass. The summary of the investigated studies is shown in the Table 2.3.

Table 2.3. Summary of the Reviews on the Hydrogen Production

Ref	Year	Key Findings
[52]	2020	Developed an energy system model comparing fossil-based and low-carbon hydrogen pathways; found that natural gas reforming dominates short-term production, while electrolysis and biomass gasification gain importance under stricter carbon limits.
[53]	2021	Assessed wind-powered hydrogen refuelling stations in South Africa; coastal cities found economically viable with production costs competitive at global levels.
[54]	2020	Conducted GIS-based assessment for co-locating wind turbines near existing stations; 4.6% of sites suitable, capable of supplying 2.3% of projected FCV demand.
[55]	2021	Hydrogen trains are sustainable and economically feasible under certain conditions.
[56]	2023	Designed PV-powered hydrogen station for Moroccan taxi fleet; hydrogen cost decreases with higher capacity (from $12.56/kg to $9.18/kg), showing strong scalability.
[57]	2024	Simulated hybrid renewable (PV–wind) hydrogen stations in Türkiye and Spain using HOMER; solar-only optimal for Niğde, hybrid best for Zaragoza, with major CO_2 savings.
[58]	2024	Developed optimization model for grid-connected electrolysis hydrogen refuelling stations; found hydrogen not yet cost-competitive, but falling electricity and electrolyser costs could reduce LCOH by ~50%.
[59]	2023	Proposed multi-hub hydrogen refuelling station integrating PV electrolysis and SMR; larger hubs reduce LCOH up to 40% while keeping emissions low.
[60]	2022	Quantified BECCS-based hydrogen potential in Europe; sustainable biomass can yield 12.5 Mt H_2 and capture 133 Mt CO_2 annually, offering a negative-emission solution.
[61]	2023	Evaluated biomass gasification with CO_2 capture; achieved 57–59% efficiency and identified membrane systems as the most cost-effective decarbonization method.
[62]	2018	Compared alkaline electrolysis, biomass gasification, and delivery for Rome hydrogen refuelling station; biomass gasification achieved lowest LCOH (≈5.99 €/kg).
[63]	2022	Compared three biomass gasification methods; supercritical water gasification achieved highest yield, while conventional gasification showed partial economic feasibility.

[64]	2023	Introduced a coupled biomass-to-hydrogen electrocatalytic system; achieved 62.5% formic acid yield and ~100% Faradaic efficiency at 1.22 V, enabling efficient co-production of H_2.

2.4. Research Gap and Contribution of the Thesis

Although the literature on hydrogen technologies has significantly advanced understanding of hydrogen production, storage, and utilization, important methodological and analytical gaps persist, particularly in linking real-world driving behaviour, hydrogen demand estimation, and renewable hydrogen production potential to the technical design of refuelling infrastructure. Most previous research has concentrated either on techno-economic assessments of large-scale hydrogen production pathways such as electrolysis, biomass gasification, or steam methane reforming, or on vehicle-level performance simulations using standardized driving cycles. However, these studies generally overlook the localized variability in driving patterns and do not explicitly translate the resulting energy demand into design criteria for on-site hydrogen refuelling stations (HRS).

Moreover, the majority of existing works focus on economic optimization or policy-level feasibility, while limited attention has been devoted to developing a comprehensive technical modelling framework that integrates realistic bus operation data, hydrogen demand modelling, and the evaluation of renewable hydrogen generation potential. Another major limitation concerns the lack of data-driven, location-specific driving cycles that can accurately capture the operational dynamics of urban transit systems. Standardized cycles such as UDDS, Orange County Bus Cycle (OCTA), or Manhattan Bus Cycle (MANDC) fail to represent local traffic fluctuations, idling behaviour, and acceleration characteristics, resulting in simplified energy consumption estimates and, consequently, imprecise hydrogen demand projections.

To overcome these limitations, this study introduces a novel hybrid optimization approach combining the MMAS and ABC algorithm for constructing a representative, high-fidelity driving cycle specific to the Modena urban area. The integration of these two algorithms leverages the global search efficiency of MMAS and the adaptive local refinement of ABC, enabling the generation of statistically accurate drive cycles that reproduce both temporal and dynamic characteristics of real driving data collected through GPS. This methodology represents a significant advancement over previous approaches that typically relied on single-swarm algorithms such as ACO or Particle swarm optimization (PSO), which often exhibited premature convergence and limited representational fidelity.

The empirically derived Modena Bus Driving Cycle (MBDC) serves as the analytical basis for the vehicle simulations performed in the ADVISOR environment, encompassing five bus configurations: Diesel Bus, CNG Bus, HEB, EB, FCB. By integrating both standardized and localized driving cycles, the study enables a rigorous comparison of vehicle performance, fuel consumption, and hydrogen demand under realistic operational conditions.

Building upon these simulations, the study proceeds to determine the technical requirements and hydrogen production capacity necessary for an on-site hydrogen refuelling station capable of supporting the representative bus fleet operating under the MBDC. In this context, renewable hydrogen production through biomass conversion pathways is also examined to evaluate its production potential and scalability as a sustainable supply option. While detailed economic optimization is beyond the scope of this research, the study focuses on developing a robust technical framework that connects hydrogen demand estimation with renewable production potential and station component sizing.

In summary, the main contributions of this research can be outlined as follows:

1. Development of a hybrid MMAS–ABC algorithm for generating a statistically accurate, localized bus driving cycle based on empirical GPS data.
2. Creation and validation of the MBDC, providing a high-fidelity representation of real bus operation in Modena's public transport network.
3. Integration of drive-cycle-based vehicle simulations with hydrogen demand estimation for the technical sizing of an on-site refuelling station.
4. Assessment of biomass-based hydrogen production potential to evaluate the feasibility of integrating renewable sources for station supply.
5. Comprehensive comparative analysis of multiple bus powertrain configurations under both standardized and localized operational conditions.

Through this integrated methodology, the study effectively bridges the gap between vehicle-level energy modelling, localized hydrogen demand estimation, and renewable-based refuelling infrastructure design.

3. METHODOLOGY

3.1. Development of the Modena Bus Driving Cycle (MBDC)

Driving cycles, which depict the variation of a vehicle's speed over a defined period, serve as essential analytical tools for evaluating vehicle performance [65]. By emulating real-world driving behaviour, they enable consistent and standardized assessments of fuel efficiency, pollutant emissions, and overall vehicle dynamics under controlled yet representative operating conditions. In this section of the thesis, the methodological framework and development stages of the bus driving cycle specifically designed for the city of Modena are presented in detail

3.1.1. Data Collection and Preprocessing

Located in northern Italy's Emilia-Romagna region, Modena is renowned for its fertile Po Valley setting, which has fostered significant culinary traditions and a prominent automotive heritage. The city's public transit system is overseen by the Società Emiliana Trasporti Autofiloviari (SETA), which provides both urban and suburban bus services across the provinces of Modena, Reggio Emilia, and Piacenza. Alongside traditional buses, Modena maintains a long-standing trolleybus network established in 1950. A key feature of this network is its flexibility, as several lines are periodically reconfigured to accommodate pedestrian zones in the city centre during weekends and holidays [66].

For this research, data was collected along Linea 7, a popular bus line in Modena selected for the driving cycle's construction. The route, which is predominantly served by trolleybuses, covers a distance of roughly 7.6 km and features 26 stops between its origin at the Gottardi stop (near the "Enzo Ferrari" Department of Engineering) and its conclusion at the Gramsci stop. Its path through various road environments, such as major thoroughfares, intersections, and constricted city streets, makes it an ideal source for a rich and representative dataset. The full route is illustrated in Figure 3.1, with its start and end points clearly marked [66].

While operational parameters such as passenger load and service frequency are critical for subsequent analyses of energy consumption at a network level, they are considered beyond the scope of this particular study. The primary focus of this driving cycle generation part is instead on the development of a representative kinematic profile based on observed vehicle speed and acceleration data.

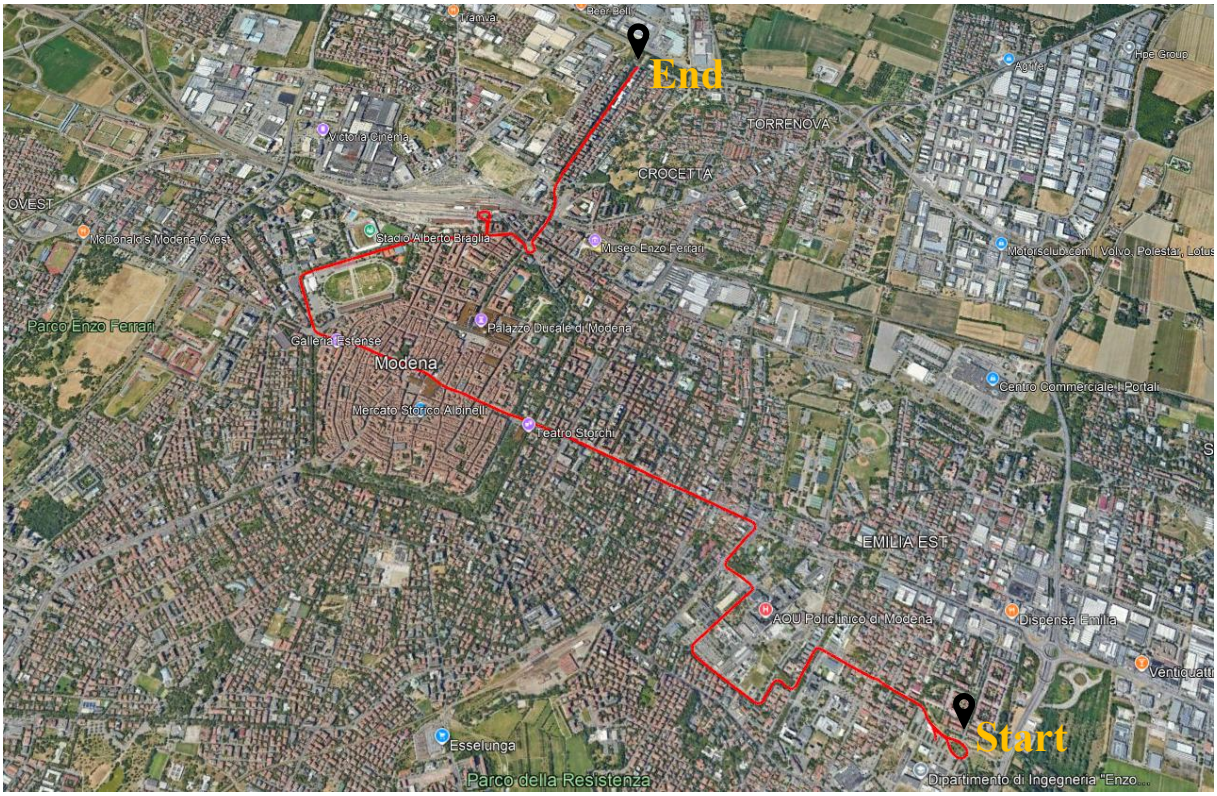

Figure 3.1. Route of the Linea 7

The use of GPS tracking to obtain mobility data is a well-established practice across various fields, including the analysis of travel behaviour, transportation safety, and efficiency assessments [67]. Within transportation research, the proven reliability and sensitivity of GPS technology embedded in modern smartphones have led to its widespread adoption for monitoring vehicle dynamics. Consequently, numerous studies have leveraged mobile device GPS data for the construction of driving cycles, a method favoured for its high accuracy and cost-effectiveness [19,29,68,69]. In alignment with this established methodology, the data for the present study were acquired using an Android mobile device running the "GPS Logger" application. The device was configured for high-frequency data capture, with a sampling rate of 1 Hz (one-second intervals), to record instantaneous geographical coordinates (latitude and longitude), timestamps, and vehicle speed as reported by the GPS chipset.

The data collection campaign was conducted along the Linea 7 route in Modena over a two-month period spanning April and May 2025. To capture a representative sample of typical urban traffic conditions, data logging was performed on multiple weekdays at various times between 10:00 and 17:00, a strategy designed to encompass a broad range of operational periods. The campaign resulted in the recording of 10 complete trips, which amounted to an aggregate travel

distance of approximately 76 kilometres. This final dataset provided the empirical foundation for the development of the Modena bus driving cycle.

It is well-documented that raw GPS data is susceptible to inaccuracies, including signal loss, abrupt fluctuations, white noise, and zero-speed drift. Such artifacts can compromise the reliability of driving cycle development and, if left unaddressed, degrade the overall data quality and impede the precision of subsequent analyses [70]. Therefore, a rigorous preprocessing procedure is essential to mitigate these errors while preserving the integrity of the data. Adopting the multi-stage filtration methodology recommended by [34,70], the initial step in this study involved a thorough manual examination of the collected speed-time profiles.

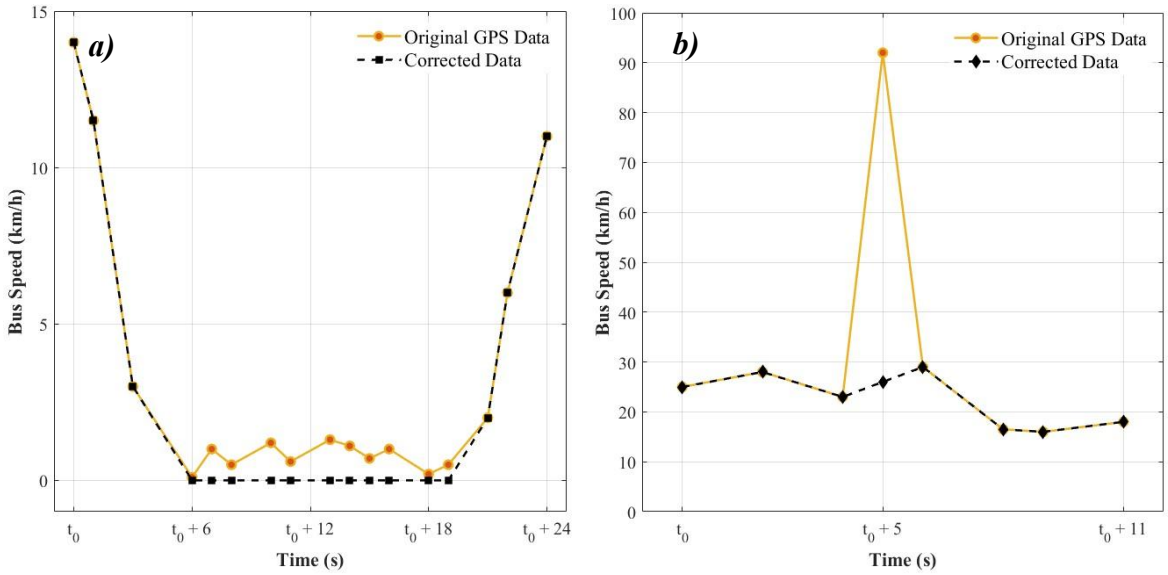

Figure 3.2. Examples of the GPS data correction a) Zero-speed drift b) Outlier speed

The initial stage of data cleaning addressed common GPS artifacts, beginning with the elimination of redundant data entries. This was followed by the correction of zero-speed drift, a known phenomenon where negligible speed values are logged by the GPS unit even when the vehicle is stationary for an extended period [29,70]. For illustrative purposes, Figure 3.2a provides a conceptual example of this correction, showing how minor speed readings during a stop are adjusted to zero. Subsequently, the data was further refined by identifying and rectifying anomalous speed outliers, a technique demonstrated conceptually in Figure 3.2b, where a sudden, erroneous spike in speed is smoothed.

The methodology for correcting these anomalies was grounded in the physical context of the bus's operation, rather than relying on arbitrary numerical limits. For the issue of zero-speed drift, a context-sensitive manual verification was employed. This involved cross-referencing

the speed data with the vehicle's GPS coordinates; minor speed variations were adjusted to zero only when the positional data confirmed that the bus was stationary at a logical stopping point, such as a bus stop or traffic signal. A similar context-aware approach was used for outlier management. Instead of applying a fixed universal threshold, the focus was on identifying physically implausible transients. Each potential outlier was examined in relation to its adjacent data points. Any speed spike implying an acceleration or deceleration rate that exceeded the bus's known performance capabilities was flagged as an artifact and subsequently rectified using linear interpolation to ensure the final speed profile remained both smooth and physically coherent.

3.1.2. Driving Cycle Generation Algorithms

For the purpose of synthesizing a bus driving cycle from real-world GPS data, this study conducted a comparative evaluation of two different methodologies. The first of these is the MCMC technique, and the second is an innovative hybrid approach that combines the MMAS with the ABC algorithm. The subsequent subsections offer a thorough explanation of the underlying framework for both of these methods.

3.1.2.1. Markov Chain Monte Carlo (MCMC) Method

A Markov chain models a sequence of random states and is governed by the Markov property. This principle asserts that the only factors determining a state's value are a limited set of the states that occurred previously [71]. If X_t is used to represent the value of a random variable at a given time t from a collection of all its possible values, known as the state space, then the variable is considered a Markov process when the chance of moving between states is contingent solely upon its current condition and is not affected by any past values. The essential behavior of any given chain is defined by its transition probabilities. The likelihood that a process will move from a state s_i to a new state s_j within a single interval is symbolized by the term p_{ij} [72].

$$P\left(X_{t+1} = s_j \,\middle|\, X_0 = s_k, \dots, X_t = s_i\right) = P\left(X_{t+1} = s_j \,\middle|\, X_t = s_i\right) \tag{3.1}$$

$$p_{ij} = P\left(X_{t+1} = s_j \,\middle|\, X_t = s_i\right) \tag{3.2}$$

The evolution of a Markov chain is governed by the Transition Probability Matrix (TPM), which is a structure that specifies the probabilities for all possible transitions between states. The formulation for the TPM can be given as follows [24]:

$$\text{TPM} = \begin{bmatrix} p_{11} & p_{12} & \cdots & p_{1t} \\ p_{21} & p_{22} & \cdots & p_{2t} \\ \vdots & \vdots & \ddots & \vdots \\ p_{t1} & p_{t2} & \cdots & p_{tt} \end{bmatrix} \tag{3.3}$$

When this concept is applied to the construction of a driving cycle, the main purpose of MCMC is to forecast a vehicle's next state by analysing its current one. This is achieved through maximum likelihood estimation, which involves segmenting the velocity-time data into discrete portions based on key parameters like velocity and acceleration. In the next step, these segments are sorted into "modal bins." This practice of grouping fragments that share similar dynamic properties serves to increase the accuracy of the modelling process [30]. Considering the vehicle's present driving conditions, a future driving cycle can then be generated by running a Monte Carlo simulation with the relevant state transition matrices [73].

In this study, the MCMC methodology was implemented by integrating two distinct but complementary components. First, a Markov chain was established to model the probabilistic transitions between different vehicle states (e.g., speed and acceleration) through the construction of a TPM. This matrix encapsulated the likelihood of a vehicle moving from one state to another, with each transition being contingent only upon the present state. Second, to incorporate the stochastic nature of real-world driving conditions, the Monte Carlo simulation component was utilized. This technique involved generating random samples to construct a multitude of potential driving scenarios and forecast future vehicle states. The synthesis of these two methods within the MCMC framework served to enhance predictive accuracy. The Markov chain provided the underlying structure for state transitions via the TPM, while Monte Carlo sampling provided the mechanism to simulate and explore a wide spectrum of possible driving cycles, ultimately leading to more reliable and comprehensive results.

3.1.2.2. MAX-MIN Ant System (MMAS)

The ACO algorithm is a computational framework for solving optimization problems that abstracts the foraging strategies of some ant species. The core inspiration is the natural mechanism where ants release chemical pheromones to mark advantageous routes, guiding other members of the colony. ACO adapts this principle, creating a positive feedback loop in which successful paths are algorithmically reinforced over time [74]. This reinforcement process guides the entire colony of artificial agents to collectively converge upon optimal or near-optimal solutions.

To overcome the issue of premature convergence often seen in standard ACO, an enhanced version known as the MMAS was developed. The MMAS algorithm achieves this by utilizing maximum and minimum bounds for pheromone values, a mechanism that regulates the search by maintaining pheromone updates within a predefined range. Recognizing that standard driving cycles often fail to represent actual driving dynamics, the MMAS method was chosen for this research because of its potential to produce a more representative generalized driving cycle.

The initialization of the algorithm requires the definition of several key parameters, including the total number of ants and iterations, the pheromone evaporation rate (ρ), and an update constant (Q). Furthermore, the term N_s is used to denote the total number of unique states that result from the discretization of the speed-acceleration space. Based on these definitions, the initial pheromone value is then set with a uniform distribution for all paths, as shown in the following expression:

$$\tau_{ij}^{(0)} = \frac{1}{\rho * N_s} \tag{3.4}$$

This uniformly set value also acts as the initial upper pheromone limit, τ_{max}. In contrast, the lower pheromone limit, τ_{min}, is determined later in the process, based on the probability of the best solution (p_{best}) and the value of N_s.

The solution-building phase begins with each individual ant generating a candidate driving cycle by navigating sequentially through the discretized state space. This process commences from a specified initial state, which is conventionally selected as the state nearest to the origin of the speed-acceleration grid. Each ant then progressively extends its path, one step at a time, until the total duration of the cycle reaches the predefined length.

The calculation of the transition probability between state i and state j involves the interplay of two main components: the accumulated pheromone level on the path (τ_{ij}) and a heuristic desirability factor (η_{ij}). The value for this heuristic factor is derived from how often that specific transition was observed in the data. The resulting probability, p_{ij}, is shown in the following equation [2,74]:

$$p_{ij} = \frac{{\tau_{ij}}^{\alpha} {\eta_{ij}}^{\beta}}{\sum_{k \epsilon \mathcal{N}(i)} {\tau_{ik}}^{\alpha} {\eta_{ik}}^{\beta}} \tag{3.5}$$

In the provided formula, the term τ_{ij} denotes the level of pheromone that has collected on the route from state i to j, while η_{ij} provides the heuristic data. Two critical exponents, α and β, are used to control how much weight is given to the pheromone level versus the heuristic data. The α parameter adjusts the importance of the pheromone factor, whereas the β parameter modifies the impact of the heuristic element within the probability formula.

Elevating the α value amplifies the effect of previously rewarding routes, a process known as exploitation, which encourages ants to follow paths that have proven effective in the past. In contrast, increasing the β value makes it more likely for ants to select options that appear optimal in the immediate vicinity according to heuristic information, a strategy that can be considered a form of greedy exploration. Consequently, achieving the right equilibrium between α and β is vital, as this balance manages the algorithm's choice between pursuing well-known, successful routes and investigating new alternatives that seem promising based on heuristics. The symbol $\mathcal{N}(i)$ is used to represent the collection of all viable subsequent states that can be reached from state i. To decide the next move for an ant, a roulette wheel selection method is employed, which makes a choice based on the computed probabilities for all possible next steps.

The validity of each candidate driving cycle is assessed with a $Cost$ function designed to measure its representativeness. This function operates by quantifying the variations between a generated cycle and the source data in terms of performance criteria, speed-acceleration distributions, and total road distance. The cycle itself is created after a full state sequence is generated by the algorithm; this sequence is then mapped back into a driving cycle through the sampling of corresponding speed-acceleration pairs.

To determine the overall $Cost$, the initial step is to compute the percentage error, Δm, for each individual metric 'm' (which includes values like average speed, acceleration, or the percentage of time in various regimes), according to the expression:

$$\Delta m = \begin{matrix} \left|\frac{m_{cand} - m_{avg}}{m_{avg}}\right| * 100, & \text{if } m_{avg} > \epsilon, \\ |m_{cand} - m_{avg}|, & \text{otherwise,} \end{matrix} \tag{3.6}$$

In the preceding formula, the term m_{cand} signifies the value for a specific metric as calculated for the candidate cycle, while m_{avg} denotes the corresponding average value of that same metric derived from the original dataset. A small constant, represented by ϵ, is incorporated to

prevent any instance of division by zero. In addition to this, a histogram error is calculated using an L_1 norm to quantify the dissimilarity between the speed distribution of the candidate cycle and that of the original data. The final, overall $Cost$ is then determined by combining these elements, as shown in the equation below:

$$Cost = \sum \Delta m + \alpha_{hist} * \text{Histogram Error} + \gamma_{distance} * \text{Distance Error} \tag{3.7}$$

In this cost function, the term α_{hist} represents the specific weight applied to the speed histogram error, while $\gamma_{distance}$ denotes the weighting factor for the distance error. At the conclusion of each iteration, after every candidate driving cycle has been evaluated, the single solution that yielded the lowest cost is identified as the global best for that iteration.

The pheromone update process within the MMAS procedure follows a two-stage approach. Initially, a uniform evaporation step is applied, where all pheromone levels are decreased according to Eq. 3.8 to mitigate the impact of biases from early iterations [74]. Subsequently, a reinforcement step is performed, in which the pheromone values are increased only along the transitions that form the path of the global best solution [2,74], as detailed in Eq. 3.9.

$$\tau_{ij} \leftarrow (1 - \rho)\, \tau_{ij} \tag{3.8}$$

$$\tau_{ij} \leftarrow \tau_{ij} + \Delta\tau \text{ with } \Delta\tau = \frac{Q}{Global\ Best\ Cost} \tag{3.9}$$

To maintain a balance between exploration and exploitation, this entire update process is regulated by a bounding mechanism. All pheromone values are kept within a range defined by a minimum, τ_{min}, and a maximum, τ_{max}. The upper bound, τ_{max}, is updated based on the expression in Eq. 3.10 [75], while the lower bound, τ_{min}, is computed using the formula in Eq. 3.11 [76]. By ensuring that pheromone levels do not become excessively large or small, these bounds effectively preserve the algorithm's overall search capabilities.

$$\tau_{max} = \frac{1}{\rho * Global\ Best\ Cost} \tag{3.10}$$

$$\tau_{min} = \tau_{max} * \frac{1 - {p_{best}}^{1/N_s}}{\left(\frac{N_s}{2} - 1\right) {p_{best}}^{1/N_s}} \tag{3.11}$$

3.1.2.3. Proposed Hybrid MMAS-ABC Method

While MMAS presents a comprehensive method for generating driving cycles, its performance is highly sensitive to the configuration of its control parameters (such as α, β, ρ and Q). Finding the ideal combination of these values manually is a significant challenge, not only because the parameters are often tightly interdependent, but also because a complete theoretical framework for their optimal selection is still lacking [77]. This difficulty is reflected in the diverse strategies seen in the literature for establishing 'fixed' parameter values. Some researchers borrow configurations from prior studies or common heuristics, whereas others conduct their own preliminary empirical tests. Such initial studies typically involve evaluating a limited range of values to find a suitable setting for the specific problem, which is then used as a static configuration in subsequent experiments. A selection of these varied approaches and the resulting parameter sets from different ACO and MMAS studies is documented in Table 3.1.

Table 3.1. Some Examples of the Parameter Settings Reported in the Literature

Reference	Problem Domain	Parameters Tested	Parameters Selected
[78]	Cloud Task Scheduling	$\alpha \in \{0, 0.1, 0.2, 0.3, 0.4, 0.5\}$, $\beta \in \{0, 0.5, 1.5, 2, 2.5, 3\}$, $\rho \in \{0, 0.1, 0.2, 0.3, 0.4, 0.5\}$, $Q \in \{1, 100, 500, 1000\}$	$\alpha = 0.3$, $\beta = 1$, $\rho = 0.4$, $Q = 100$
[79]	Travelling Salesman Problem (TSP)	$\alpha \in \{0, 0.5, 1, 2, 5\}$, $\beta \in \{0, 1, 2, 5\}$, $\rho \in \{0.3, 0.5, 0.7, 0.9, 0.999\}$, $Q \in \{1, 100, 10000\}$	$\alpha = 1$, $\beta = 5$, $\rho = 0.5$, $Q = 100$
[77]	Path Planning for a Mobile Robot	$\alpha \in \{0, 0.5, 1, 2, 4\}$, $\beta \in \{0, 2, 5, 7,9\}$	$\alpha = 1$, $\beta = 7$
[80]	Multi-UAVs Coordinated Trajectory Replanning	Not explicitly tested	$\alpha = 3$, $\beta = 2$, $\rho = 0.7$, $Q = 10$

The ABC algorithm, a nature-inspired metaheuristic that models the collective foraging behaviour of honeybees, has consistently shown strong capability in addressing complex numerical optimization problems [81,82]. In the context of the present hybrid framework, ABC is not employed for the direct construction of the driving cycle. Instead, its role is to optimize the key control parameters of the MMAS algorithm, denoted by the vector $\mathrm{p} = [\alpha, \beta, \rho, Q]$ (see Section 3.1.2.2). During this optimization process, the search domain for each parameter was defined within the following bounds: α and $\beta \in [0.1, 5.0]$, $\rho \in [0.01, 1.0]$, and $Q \in [1, 1000]$.

These intervals were selected with reference to parameter ranges commonly reported in the ACO/MMAS literature, complemented by preliminary assessments to ensure a sufficiently broad exploration of the parameter space. The ultimate aim of this hybrid strategy is to autonomously determine an effective set of MMAS parameters that improve the algorithm's performance, thereby yielding a generalized driving cycle that more faithfully reproduces the statistical properties of the empirical driving data.

To strengthen the optimization procedure, the ABC algorithm simulates a cyclic search mechanism conducted by three distinct groups of agents, mirroring the cooperative behaviour of bees in a natural colony. Each group (Employed Bees, Onlooker Bees, and Scout Bees) plays a specific role in balancing exploration and exploitation within the search space.

Employed Bees: In this phase, every food source p_i within the population is assigned to an Employed Bee responsible for its exploitation. Each Employed Bee generates a new candidate solution p_{new} in the neighbourhood of p_i by applying a differential mutation mechanism that depends on its current position and another randomly chosen solution p_k from the population [81]:

$$\mathrm{p}_{new} = \mathrm{p}_i + \phi\,(\mathrm{p}_i - \mathrm{p}_k) \tag{3.12}$$

Here, ϕ represents a random scalar within the interval [-1, 1]. The generated candidate solution p_{new} is adjusted to remain within the predefined lower (L_B) and upper (U_B) bounds. Once generated, its fitness is evaluated. If p_{new} demonstrates better fitness than p_i, the Employed Bee updates its memory by replacing p_i with p_{new} and resets the associated trial counter. Otherwise, if no improvement is observed, the trial counter of p_i is incremented, indicating stagnation in that region of the search space.

Onlooker Bees: After the Employed Bees complete their evaluations, Onlooker Bees use the shared fitness information to select food sources for further exploration. The probability $Prob_i$ that an Onlooker Bee chooses a given source i is determined by its relative fitness value Fit_i, computed as [81]:

$$Prob_i = \frac{Fit_i}{\sum_j Fit_i} \tag{3.13}$$

A roulette-wheel selection strategy is applied to probabilistically assign sources based on $Prob_i$. Once a source is chosen, an Onlooker Bee creates a neighboring candidate solution p_{new} using

the same differential mutation approach as the Employed Bees. The newly generated solution is then evaluated, and a greedy selection rule is applied, retaining the better solution while updating the trial counter accordingly.

Scout Bees: To prevent premature convergence and improve global search capability, the algorithm introduces a discovery mechanism triggered when a food source fails to improve over a defined number of trials. When this limit is reached, the source p_i is considered abandoned, and the corresponding Employed Bee transforms into a Scout Bee. The Scout discards the obsolete solution and initiates a random search, generating a new candidate food source (parameter set) uniformly distributed within the predefined bounds $[L_B, U_B]$ of the search domain [82]. This reinitialization enhances the algorithm's ability to escape local optima.

Fitness Evaluation: The quality or "profitability" of any candidate parameter vector $p = [\alpha, \beta, \rho, Q]$ produced by the Employed, Onlooker, or Scout Bees is measured through an objective function tailored to the underlying optimization problem. In this hybrid scheme, fitness evaluation requires executing the MMAS algorithm configured with the parameters defined by p. The outcome of this execution yields a performance metric, referred to as $Cost$, which quantifies the accuracy of the driving cycle generated under those parameter settings (see Eq. 3.7).

Since the ABC algorithm typically maximizes fitness values, the $Cost$ metric is transformed into a fitness score, where smaller values indicate superior performance, using the following expression [83]:

$$\text{Fitness} = \frac{1}{(1+\max(0,Cost))} \tag{3.14}$$

This transformation ensures that solutions producing lower Cost values (i.e., better MMAS performance) correspond to higher fitness levels, thereby increasing their likelihood of being selected and propagated by the colony during subsequent search iterations.

Figure 3.3 conceptually outlines the workflow of the proposed hybrid MMAS–ABC optimization framework. The ABC Optimization Layer represents the search behaviour of the Artificial Bee Colony algorithm, which explores potential solutions to determine the most effective parameter configuration for the MMAS. The MMAS Solution Layer illustrates how the Max–Min Ant System operates within the solution space to construct driving cycles, guided by the parameter values obtained from the ABC layer.

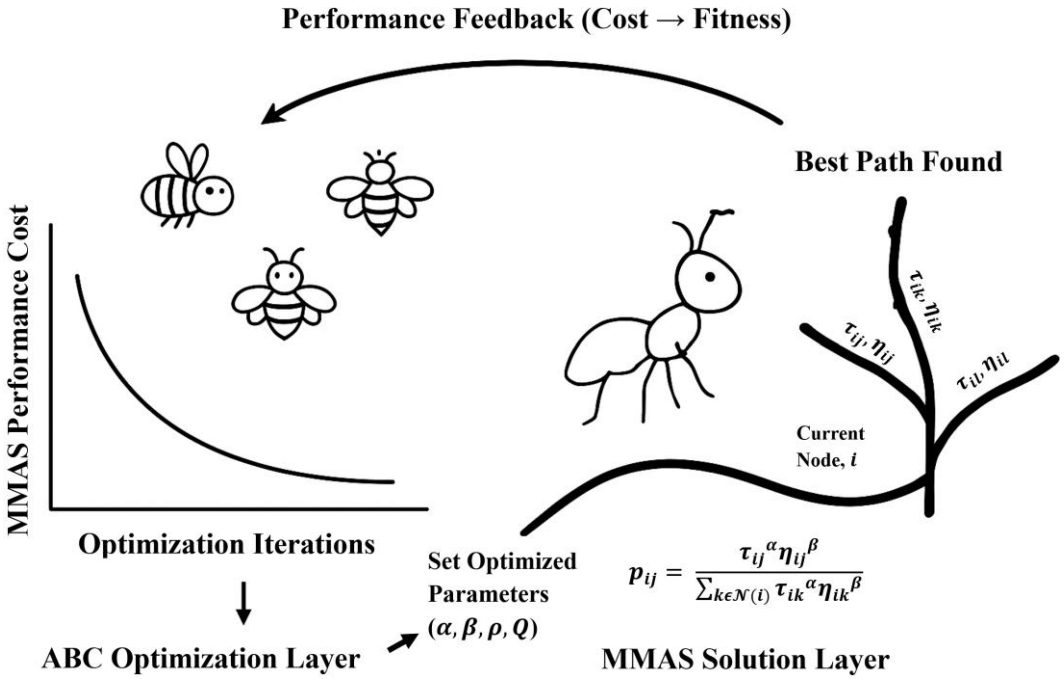

Figure 3.3. Illustrative Diagram of the MMAS–ABC Hybrid Optimization Strategy for Driving Cycle Generation

To expand upon this conceptual overview, Algorithm 1 provides a systematic description of the entire hybrid procedure. The framework is organized hierarchically: the ABC algorithm acts as the upper-level optimizer, adaptively fine-tuning the control parameters that govern MMAS performance. Once these parameters are established, the MMAS algorithm functions at the lower level, employing them to generate, test, and refine candidate driving cycles.

Overall, the process unfolds in three sequential stages. First, an initialization phase prepares and normalizes the input data. Next, during the ABC optimization phase, the MMAS algorithm is repeatedly executed as a fitness evaluator to guide the ABC's parameter search. Finally, in the generation phase, the optimized parameters are applied to produce the finalized driving cycle that best satisfies the defined objectives.

Algorithm 1: Hybrid MMAS–ABC Optimization Framework

Input:
-RealWorldData: GPS-based real-world driving data.
-ABC_params: ABC configuration (maximum cycles, colony size, abandonment limit).
-MMAS_eval_settings: Execution parameters for MMAS evaluations (number of ants, internal iterations, number of repeated runs).

Output:
- Final_Driving_Cycle: The optimized representative driving cycle.

// --- Phase 1: Data Preparation and Initialization---
1: ProcessedData ← Load and preprocess RealWorldData.
2: StateSpace, η ← Discretize ProcessedData and compute the heuristic matrix η.
3: TargetMetrics ← Derive key statistical indicators from ProcessedData.
4: ProblemData ← Aggregate all preprocessed data for MMAS evaluation.

// --- Phase 2: ABC Optimization for MMAS Parameter Tuning---
5: // Initialize Population
6: for each bee i = 1 to ABC_params.population_size do
7: Population[i].params ← Generate random MMAS parameters { α, β, ρ, Q }.
8: Population[i].cost ← Call MMAS_Fitness_Evaluation (Population[i].params, ProblemData, MMAS_eval_settings).
9: Population[i].fitness ← 1 / (1 + Population[i]. $Cost$).
10: end for
11: GlobalBestParams ← Identify the parameter set with the lowest $Cost$.

12: // Main ABC Loop
13: for cycle = 1 to ABC_params.max_cycles do
14: // --- Bee Phases (Employed, Onlooker, Scout) ---
15: Generate new candidate solutions using the perturbation equation:
16: $p_{new} \leftarrow = p_i + \phi (p_i - p_k)$
17: for each new candidate p_{new} do
18: new_$Cost$ ← Call MMAS_Fitness_Evaluation (p_{new}, ProblemData, MMAS_eval_settings).
19: Apply greedy update: if new_ $Cost$ is better, update the Population.
20: end for
21: Perform scout phase to reinitialize stagnated solutions.
22: Update GlobalBestParams if a superior candidate emerges.
23: end for
// --- Phase 3: Final Cycle Generation ---
24: Execute MMAS_core once more using the final GlobalBestParams.
25: Output the resulting Final_Driving_Cycle.
// ---
// Helper Function: MMAS_Fitness_Evaluation (params, problem, settings)
// ---
Run MMAS_core multiple times (num_runs) to compute an average cost.
// Within each MMAS execution:
// 1. Path Construction
Ants probabilistically select nodes using:
$p_{ij} \leftarrow \frac{\tau_{ij}^{\alpha} \eta_{ij}^{\beta}}{\sum_{k \epsilon \mathcal{N}(i)} \tau_{ik}^{\alpha} \eta_{ik}^{\beta}}$
// 2. Pheromone Update
// a. Evaporation:
$\tau_{ij} \leftarrow (1 - \rho) * \tau_{ij}$
// b. Reinforcement (on the best path):
$\tau_{ij} \leftarrow \tau_{ij} + \Delta\tau$, where $\Delta\tau = Q / Best\ Cost$
// ... (Calculate $Cost$ of the cycle generated) ...
return average_ $Cost$
end Function

3.1.3. Evaluation of Cycle Representativeness

To move beyond a purely qualitative assessment and rigorously validate the fidelity of the generated driving cycles, it is imperative to establish a quantitative comparison against the original, empirically collected GPS data. To construct a robust and widely accepted evaluation framework for this purpose, an extensive review of the relevant literature was performed. Based on this review, a comprehensive suite of ten key performance parameters was adopted for the comparative analysis, drawing upon established metrics from seminal studies in the field [19,26,84]. These selected parameters were then systematically utilized to quantify the alignment between the kinematic and modal characteristics of each synthesized driving cycle and the aggregated real-world driving data. This quantitative evaluation formed the primary basis for identifying the most representative and accurate cycle among the generated candidates. Table 3.2. provides a detailed summary of these ten chosen parameters, along with the specific mathematical formulations used for their computation. To clarify the notation within these formulas, N represents the total count of all recorded speed data points in the time series, while the subset of these points where the vehicle is in motion (i.e., speed is greater than zero) is denoted by N_r. The modal characteristics are captured by n_a and n_d, which correspond to the total number of data points where the vehicle is experiencing positive acceleration and negative acceleration (deceleration), respectively. Finally, the instantaneous values at any given time step i are represented by a_i for acceleration, d_i for deceleration, and v_i for the vehicle's speed [19].

Table 3.2. Performance Parameters for Assessing Driving Cycle

Abbr.	Def.	Unit	Expression
$\boldsymbol{v_a}$	Average Speed	km/h	$\frac{\sum_{i=1}^{n} v_i}{N}$
$\boldsymbol{v_r}$	Average Running Speed	km/h	$\frac{\sum_{i=1}^{n} v_i}{N_r}$
$\boldsymbol{a}$	Average Acceleration	m/s^2	$\frac{\sum_{i=1}^{n} a_i}{n_a}$
$\boldsymbol{d}$	Average Deceleration	m/s^2	$\frac{\sum_{i=1}^{n} d_i}{n_d}$
$\boldsymbol{P_i}$	Time Percentage of Idling Mode	%	Percentage of $v_i = 0$
$\boldsymbol{P_a}$	Time Percentage of Acceleration Mode	%	Percentage of $a \geq 0.1$ and $v_i \geq 5$
$\boldsymbol{P_c}$	Time Percentage of Cruising Mode	%	Percentage of $-0.1 \leq a \leq 0.1$ and $v_i \geq 5$
$\boldsymbol{P_d}$	Time Percentage of Deceleration Mode	%	Percentage of $a \leq -0.1$ $v_i \geq 5$

P_{cr}	Time Percentage of Creeping Mode	%	Percentage of $-0.1 \leq a \leq 0.1$ and $v_i \leq 5$
RMS	Root Mean Square Acceleration	m/s^2	$\sqrt{\frac{\sum_{i=1}^{n} {a_i}^2}{n_a}}$

The culminating phase of the methodology is the selection of a single, optimally representative driving cycle from the candidates produced by the MCMC and hybrid MMAS-ABC methods. This selection is governed by a standardized set of evaluation metrics, with the primary objective of minimizing the discrepancy between a synthesized cycle and the original observed driving patterns.

For the MCMC method, the process begins after the generation of a large ensemble of candidate cycles. The optimal cycle is then identified by evaluating each candidate against a composite error metric, which aggregates the deviations from the target characteristics. This error metric is conceptually analogous to the cost function utilized for fitness evaluation in the hybrid MMAS-ABC approach (as detailed by Eq. 3.7). For the MMAS-ABC framework, the optimal cycle is inherently the one generated using the optimized parameters, as this configuration yielded the best performance by minimizing the aforementioned cost function.

Ultimately, regardless of its origin (whether selected from the MCMC pool or generated via the optimized MMAS-ABC approach), the single candidate cycle that exhibits the minimal aggregate error based on these cumulative deviations is designated as the optimal generalized driving cycle, accurately reflecting the specific driving conditions investigated.

3.2. Development of Bus Models and Simulation Environment

3.2.1. Fundamentals of Vehicle Performance

The principle of inertia describes an object's inherent resistance to any alteration in its state of motion, including changes to its velocity or direction [85]. The governing equation for a vehicle's longitudinal motion, which accounts for this inertia along with other tractive and resistive forces, is presented in the following equation:

$$m_v v_v = \left[\frac{(T_o f_d + T_{brk})\eta_d}{r_d}\right] - \left(\frac{1}{2}\rho_{air} C_D A_v {v_v}^2\right) - [m_v g(f_r cos\alpha_{road} + sin\alpha_{road})] \quad (3.15)$$

The variables within this formula are defined as follows: m_v represents the vehicle's mass (kg) and v_v is its speed (m/s). Tractive forces are determined by T_o, the torque delivered by the powertrain (Nm), and T_{brk}, the braking torque (Nm), which are applied through the f_d (total

gear ratio) and r_d (wheel radius, m) with a final drive efficiency of η_d. Resistive forces include aerodynamic drag, defined by ρ_{air} (air density, kg/m³), A_v (vehicle frontal area, m²), and C_D (drag coefficient, -); gravitational forces, defined by g (gravitational acceleration, m/s²) and α_{road} (road angle, rad); and rolling resistance, defined by f_r (rolling resistance coefficient) [86–88].

A vehicle's performance on an incline is a critical factor, as road grade directly impacts fuel consumption by demanding additional power to counteract gravitational and frictional forces. As a slope increases, the gravitational resistance component ("$mgsin\alpha_{road}$" in Eq. 3.15) directly opposes the vehicle's forward motion. Concurrently, the rolling resistance ("$mgf_rcos\alpha_{road}$" in Eq. 3.15) also rises due to the increased normal force on the tires. These combined forces necessitate higher torque output from the engine to sustain speed, which consequently increases fuel consumption and lowers overall efficiency. Therefore, neglecting road grade in vehicle performance analyses can introduce considerable inaccuracies in both fuel economy and emissions predictions.

A vehicle's capacity to handle such slopes is quantified by its gradeability [51], which is formally defined as the maximum incline a vehicle can ascend while holding a specified constant speed. This metric, which characterizes the vehicle's climbing ability, is typically expressed as a percentage that corresponds to the tangent of the road angle [89]. The specific power P_G required for a vehicle to ascend a hill, overcoming the road slope, is calculated using the formula presented in the Eq. 3.16 [90]:

$$P_G = \frac{1}{2}\rho_{air}C_D A_v {v_v}^3 + m_v g v_v sin\alpha_{road} + m_v g f_r v_v cos\alpha_{road} \tag{3.16}$$

The concept of fuel economy serves as a primary metric for quantifying a vehicle's efficiency in converting the chemical energy stored in its fuel into the mechanical work required to cover distance. This efficiency is typically expressed in one of two conventional forms: as fuel consumption, which measures the volume of fuel used per unit distance (e.g., litters per 100 kilometres, L/100 km), or as fuel efficiency, which measures distance covered per unit volume of fuel (e.g., miles per gallon, MPG) [91]. A lower value for fuel consumption or a higher value for fuel efficiency signifies superior operational efficiency. The standard calculation for MPG is provided in the following equation [51]:

$$MPG = \frac{Total\ driven\ miles * Energy\ of\ one\ gallon\ gasoline}{Total\ fuells\ energy\ consumed} \tag{3.17}$$

To provide a standardized and equitable method for comparing the energy use of the diverse bus technologies evaluated in this study, all consumption figures are normalized to gasoline-equivalent units. This normalization is essential because the vehicles operate on disparate energy carriers (e.g., diesel, CNG, hydrogen, electricity), rendering direct comparisons of their native consumption units (litters, m^3, kg, kWh) meaningless for assessing relative efficiency. By converting all fuel types to a common energetic reference point—the energy content of gasoline—this approach simplifies cross-technology comparisons and clearly highlights the true energy efficiency of each powertrain. This methodology is a common practice in the field and has been employed in numerous other comparative studies [92–94]. The conversion is calculated based on the energy content of the specific fuel being used relative to the energy content of gasoline. For instance, the 33.7 kWh of energy contained in one gallon (3.785 L) of gasoline is energetically equivalent to consuming approximately 1 kg of hydrogen [92]. The formal equation used for this conversion is [95]:

$$Gasoline\ Equivalent = \frac{FC}{EC_F} * EC_G \tag{3.18}$$

In Eq. 3.18, FC denotes the vehicle's measured fuel consumption, EC_F represents the energy content of the specific fuel type being evaluated, and EC_G signifies the energy content of the gasoline reference.

Beyond fuel properties, the physical interaction between the vehicle's structure and the surrounding air is a critical factor in determining the aerodynamic forces exerted on the bus. These forces, in turn, have a substantial effect on overall fuel efficiency and operational performance. A comprehensive understanding of these aerodynamic principles is vital for improving bus design, as managing airflow to minimize drag also enhances vehicle stability. By prioritizing aerodynamic efficiency, manufacturers can develop more energy-efficient vehicles. This optimization, which involves meticulous shaping of the vehicle's body and integrating various aerodynamic features, is an essential strategy for improving both performance and fuel economy. The equation for calculating the drag coefficient is [96]:

$$C_D = \frac{2F_D}{\rho_{air} A_v {v_v}^2} \tag{3.19}$$

In this equation, F_D shows the drag force.

3.2.2. Simulation Tool: Advanced Vehicle Simulator (ADVISOR)

The ADVISOR, originally developed by the National Renewable Energy Laboratory (NREL), serves as a comprehensive simulation platform for evaluating the performance of a broad spectrum of vehicles including conventional, hybrid, electric, and fuel cell models across multiple driving cycles [97]. Built on MATLAB/Simulink, ADVISOR combines modular flexibility with a user-friendly graphical interface, enabling users to customize detailed vehicle configurations and control algorithms. Its open-source and offline structure facilitate the modelling of complex propulsion systems while allowing integration with MATLAB/Simulink modules for component-level customization. Through this interface, users can readily modify algorithms, such as regenerative braking or energy management strategies, to simulate real-world operating conditions more accurately. The software includes an extensive selection of predefined system components: nine complete drivetrains, nineteen electric motors, nine battery types, and seven fuel cell models [93]. This versatility supports holistic evaluation of various design alternatives and presents system performance metrics in clear graphical formats, which is essential for refining vehicle architectures and enhancing efficiency. Owing to its adaptability and validated modelling accuracy, ADVISOR has become widely adopted by automotive manufacturers and research institutions alike. The growing community of contributors has further enriched its functionality by adding new subsystems, datasets, and validated experimental results [93,97,98]. Although field testing provides valuable empirical validation, it remains resource-intensive due to the need for specialized instrumentation, facilities, and time-consuming test procedures. Consequently, simulation tools such as ADVISOR have become indispensable for performance prediction and optimization.

In this research, ADVISOR was employed to analyse the performance of buses powered by different fuel types. Its proven compatibility with NREL's empirical data enabled accurate numerical simulations, effectively reducing the need for extensive physical testing. The Orion VI low-floor transit bus, equipped with a 205-kW diesel engine, was chosen as the baseline model. This selection was based on its pre-existing parameterization in ADVISOR and the availability of validated fuel consumption data [99,100]. The modelled bus features a front axle static load fraction of 0.45, a wheelbase of 6.86 m, glider mass of 12,636 kg, frontal area of 6.52 m^2, and an C_D of 0.79. The corresponding MATLAB/Simulink block diagram of this configuration is shown in Figure 3.4.

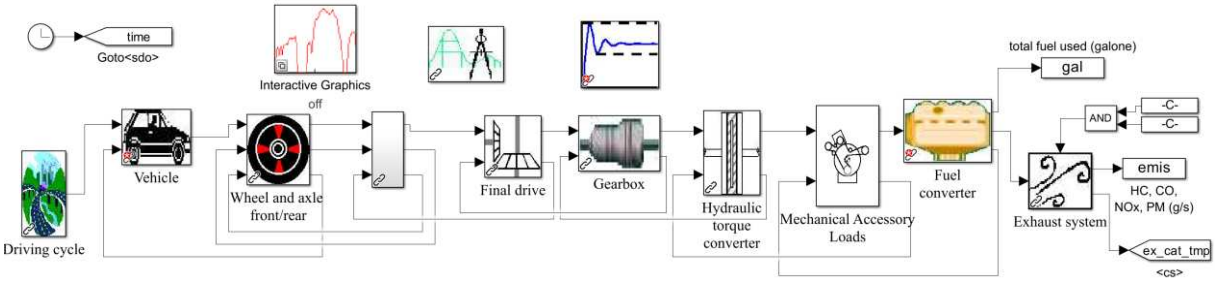

Figure 3.4. Block Diagram of the Diesel Bus

3.2.3. Validation of the Diesel Bus Model

According to NREL, the Orion VI diesel bus demonstrates a fuel economy of 3.2 MPG (diesel equivalent) when operating with the air conditioning (A/C) system engaged, and 4.0 MPG with the A/C turned off. The A/C-off measurements were obtained using chassis dynamometer testing over the Central Business District (CBD-14) driving cycle, whereas A/C-on values were derived from simulation-based estimation by incorporating a representative A/C load profile into the ADVISOR model. These estimations were verified through the 21CT Program Transit Bus Working Group, which included both industrial and governmental participants [100].

In the present study, the ADVISOR model was validated by directly comparing its simulated fuel consumption results with the empirical data reported by NREL for the CBD-14 drive cycle [100]. Over the approximately 3.23 km cycle, the model predicted a total diesel consumption of 2.437 L with A/C on and 2.0 L with A/C off. When normalized to 100 km, this corresponds to 75.4 L/100 km (3.1 MPG) with A/C and 61.9 L/100 km (3.8 MPG) without A/C, both closely matching NREL's measured data. In these simulations, the A/C load was set to 14 kW [100]. These results confirm the model's ability to accurately replicate real-world operating behaviour, establishing the credibility of the Orion VI diesel configuration as a validated baseline for subsequent comparative analyses.

In addition, ADVISOR provides energy consumption results in gasoline-equivalent units, facilitating direct cross-comparison among different bus powertrains. Under this convention, fuel usage equated to 70.9 L/100 km (A/C off) and 86.3 L/100 km (A/C on). The comparative summary of both empirical and simulated fuel consumption values is presented in Table 3.3, which supports the consistency between the model and experimental benchmarks.

Table 3.3. Comparison of the Fuel Consumption for the Diesel Bus Model

Condition	NREL [100]	Simulated Results (This Study)
A/C Off	4.0 MPG	3.8 MPG / 70.9 L gasoline equivalent
A/C On	3.2 MPG	3.1 MPG / 86.3 L gasoline equivalent

3.2.4. Definition of Vehicle Models: Technical specifications of Diesel, CNG, HEB, EB and FCB models

After validating the baseline diesel bus model, a series of alternative bus configurations were developed to assess their performance under the CBD-14 and OCTA drive cycles. Each model's control logic and powertrain setup were tuned to ensure minimal deviation between target and actual velocity profiles. Despite driver proficiency, minor fluctuations in speed tracking are unavoidable. To mitigate this variability, standardized fuel economy protocols define permissible speed tolerance ranges for each cycle [101]. Driving patterns exert a substantial influence on both fuel efficiency and exhaust emissions. As such, some researchers employ robotic driving systems to ensure consistent adherence to drive cycle profiles and to eliminate human-induced discrepancies [102]. According to the Environmental Protection Agency (EPA), during vehicle testing, the instantaneous speed deviation from the target value should not exceed ±3.21 km/h for longer than 2 seconds. However, temporary reductions in speed below target values are acceptable when the vehicle operates at maximum available power [103]. In this study, all modelled powertrains were designed in accordance with these EPA guidelines to ensure simulation validity. For the hybrid electric bus configuration, two battery sizing scenarios (15 and 30 battery modules) were examined in conjunction with the diesel engine to analyse their influence on overall performance, energy consumption, and system responsiveness.

Figure 3.5a depicts how the state of charge (SOC) of the energy storage system (ESS) changes throughout the OCTA driving cycle, comparing configurations with 15 and 30 battery modules (each rated at 12 V and 60 Ah) under active A/C conditions. When only 15 modules are utilized, the available charge is rapidly exhausted, compelling the diesel engine to provide the additional power needed to meet the target speeds of the drive cycle. As a result, a minor discrepancy arises between the desired and the actual vehicle speed. This deviation can be mitigated by increasing the engine's output, thereby compensating for the reduced number of modules.

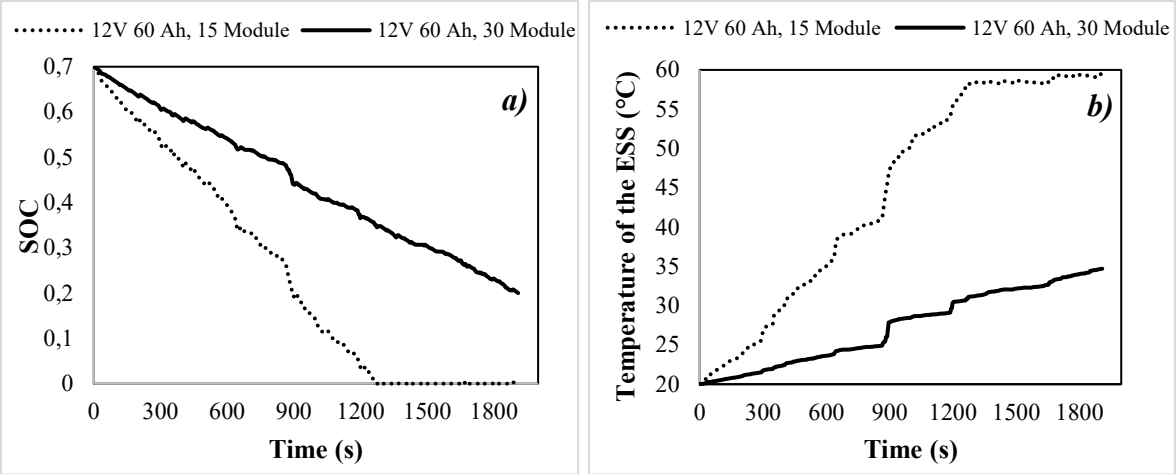

Figure 3.5. a) State of Charge and b) Temperature of the Energy Storage System on the OCTA Driving Cycle for the Hybrid Electric Bus

Figure 3.5b presents the temperature behaviour of the battery modules under varying module quantities. Employing fewer modules leads to greater electrical loading on each unit, which in turn raises the operating temperature. The peak temperature recorded for 15 modules reached 59.5 °C, whereas with 30 modules it was 34.7 °C. Considering that the safe operating limit for nickel–metal hydride batteries is around 70 °C, maintaining an optimal module count is critical, not only to prevent thermal stress and fire hazards but also to avoid escalating cooling system costs and design complexity [104]. For all simulations, the initial SOC of each module was assumed to be 0.7, and the starting temperature was set to 20 °C.

A similar performance trend was identified in the EB configuration. Figure 3.6 illustrates how the vehicle speed varies under A/C on conditions in the OCTA driving cycle, using 30 and 50 battery modules rated at 12 V–60 Ah each. When powered by 30 modules, the EB was unable to complete the drive cycle since the battery SOC dropped to depletion before finishing. In contrast, with 50 modules, the EB successfully maintained sufficient SOC, enabling it to complete the drive cycle with only minimal deviation from the prescribed speed profile, consistent with EPA-recommended performance benchmarks.

The specifications for the conventional bus models, specifically the diesel and CNG versions, were established using data from existing literature, including key parameters such as auxiliary power unit (APU) output and transmission characteristics [100]. For the design and simulation of the hybrid electric, electric, and fuel cell bus models, EPA guidelines were followed. The primary objective of this approach was to minimize the instantaneous deviation between the simulated vehicle speed and the target speed of the reference drive cycle. A summary of the

comparative data illustrating these speed deviations for both the CBD-14 and OCTA cycles is provided in Table 3.4.

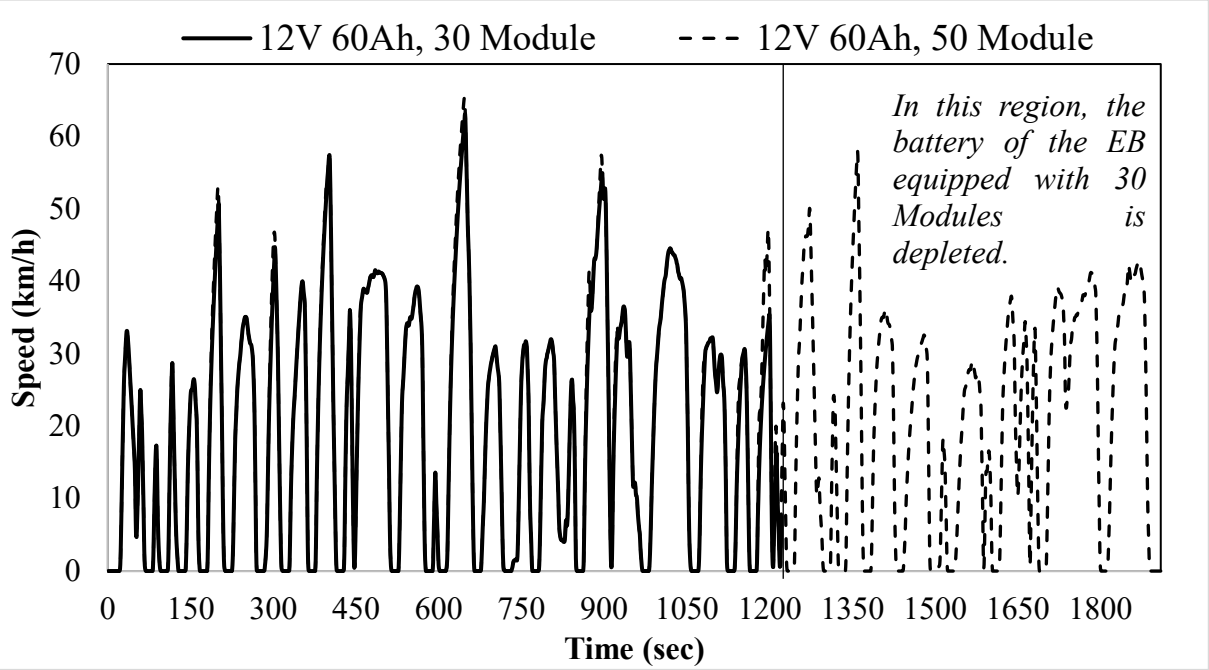

Figure 3.6. Vehicle Speed for Different Number of Battery Modules on the OCTA Driving Cycle

Table 3.2. Comparison of Speed Deviations for Different Bus Types

Drive Cycle	Vehicle Type	$Avg.Diff$ (km/h)	$Diff_t > 3.21_{km/h}$	$Diff_{max,t}$ (km/h)
CBD-14	Diesel Bus	0.044	0%	0.00315
	CNG Bus	0.021	0%	0.48
	Hybrid Electric Bus	0.0246	0%	0.00155
	Electric Bus	0	0%	0
	Fuel Cell Bus	0	0%	0
OCTA	Diesel Bus	0.115	1.52 %	8.38
	CNG Bus	0.4	5.02%	12.05
	Hybrid Electric Bus	0.0007	0%	0.518
	Electric Bus	0.003	0%	0.69
	Fuel Cell Bus	0.12	1.15%	5.34

Table 3.4. provides a quantitative comparison of the speed deviations for the different bus types, using several key metrics. $Avg.Diff$ is defined as the average absolute difference between the target speed and the simulated bus speed. The percentage of total time during which this difference surpassed 3.21 km/h is given by $Diff_t > 3.21_{kph}$, and the maximum instantaneous deviation recorded is denoted by $Diff_{max,t}$.

A significant methodological consideration was the inclusion of A/C operation in all bus configurations to create a worst-case scenario, given the additional load it places on the powertrain. To meet the demands of this high-load condition, essential components like the APU, electric motor, fuel cell, and battery module count were sized accordingly. The five distinct bus models developed with this approach are summarized in Table 3.5, with their differing total masses resulting from the varied engine and battery systems used. A standard passenger load of 26 people, each weighing a nominal 68 kg, was assumed for all simulations [100].

Table 3.3. Properties of the Created Bus Models

Vehicle Type	Weight (kg)	APU	Electric Motor	Battery
Diesel Bus [100]	14515	Detroit Diesel Corp. Series 50 8.5 (205kW) Diesel Engine	-	-
CNG Bus [100]	15223	John Deere 8.1L (209kW) CNG SI Engine	-	-
Hybrid Electric Bus (HEB)	15797	Detroit Diesel Corp. Series 30 7.3L (171kW) Diesel Engine	Westinghouse 75-kW (continuous) AC induction motor	60 Ah NiMH, 12V, 30 modules
Electric Bus (EB)	15194	-	187-kW (continuous) 3-phase AC induction motor/inverter	60 Ah NiMH, 12V, 50 modules
Fuel Cell Bus (FCB)	15685	Fuel Cell 100 kW	187-kW (continuous) 3-phase AC induction motor/inverter	60 Ah NiMH, 12V, 30 modules

The HEB employs a 171-kW diesel engine coupled with an integrated battery pack, forming a combined powertrain that leverages both mechanical and electrical energy sources. In contrast, EB eliminates the internal combustion engine entirely, deriving its propulsion exclusively from battery-based energy storage.

For the FCB, propulsion is achieved through a system composed of two ANL Model 50 kW (net) hydrogen fuel cell units, operating under ambient pressure and collectively capable of delivering a maximum output of 100 kW. The adoption of these particular fuel cell modules aligns with common configurations reported in previous fuel cell vehicle simulations within the literature [93,94,105,106]. The efficiency and operational performance of the APUs and electric

motors incorporated in this study are illustrated through their respective efficiency maps depicted in Figure 3.7.

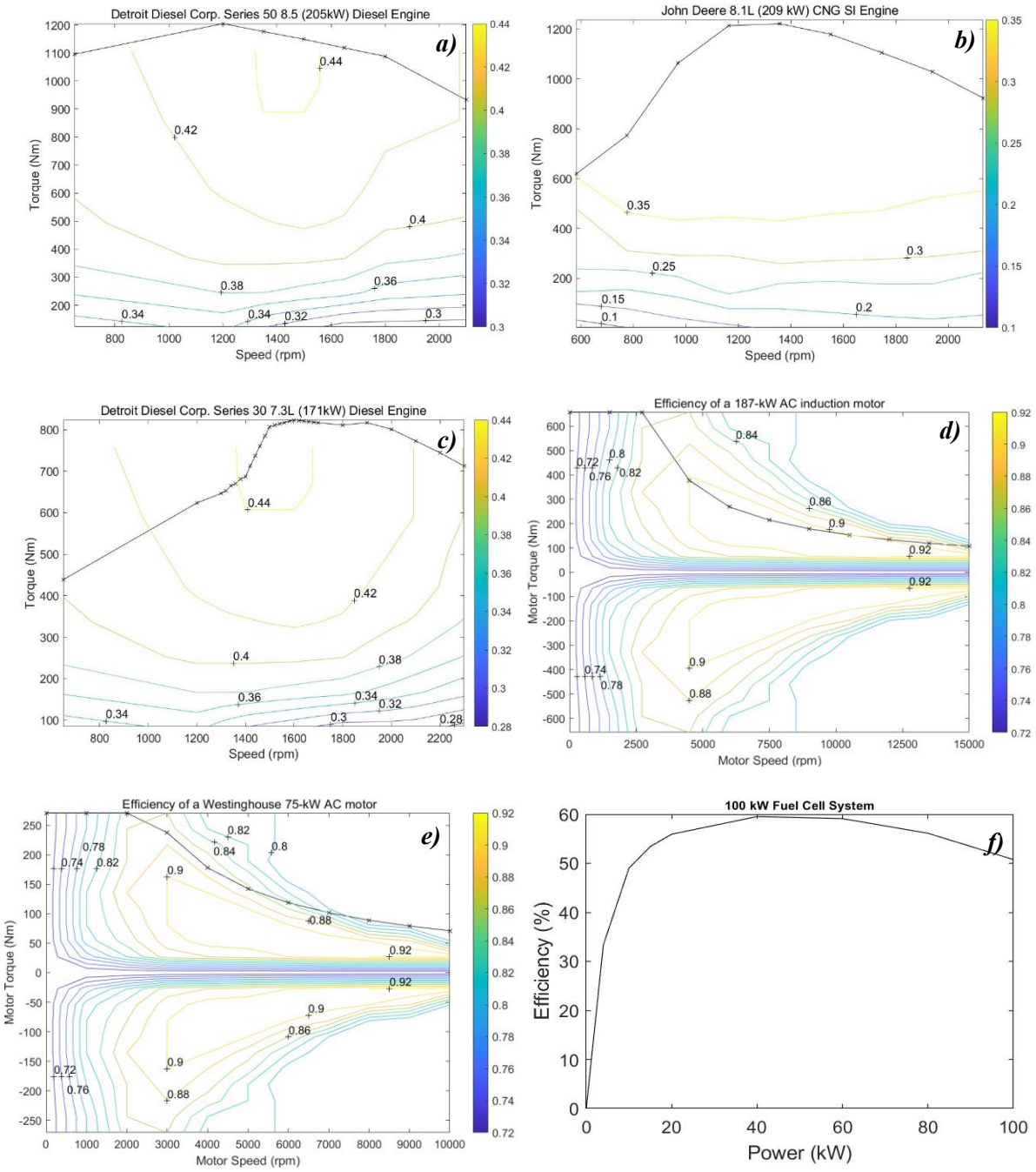

Figure 3.7. Efficiency contour maps illustrating the relationship between torque and rotational speed for: (a) a 205 kW diesel engine, (b) a 209 kW CNG spark-ignition (SI) engine, (c) a 171 kW diesel engine, (d) a 187 kW AC induction motor, (e) a 75 kW Westinghouse AC motor, and (f) the 100 kW fuel cell stack efficiency distribution.

3.2.5. Thermal/HVAC Assumptions for the Fuel-Cell Bus

This study models temperature-dependent heating, ventilation, and air conditioning (HVAC) penalties with two simple thresholds: a heating/cooling stress band whenever the daily mean ambient temperature is either below 10 °C or above 26 °C, and a baseline band for 10–26 °C. On "stress" days, vehicle hydrogen consumption is evaluated with the higher, HVAC-on map; on baseline days, the lower map is used. This choice deliberately trades fine thermal realism for a robust, transparent rule that aligns with field evidence on how heating and cooling actually influence FCB energy use.

Heating is typically more demanding than cooling in transit service, particularly with frequent door cycles and low ambient temperatures. Recent chassis-dyno tests on a production fuel-cell city bus reported much larger energy to heat a cold cabin (6.37 kWh, ≈ 0.34 kg H_2) than to cool a pre-heated cabin (1.74 kWh, ≈ 0.09 kg H_2), and documented ≈ 6 % HVAC and ≈ 8 % door penalties in an urban cycle [107]. On the cooling side, default setpoints around 22 °C and door-induced local drops (~1.8 °C) were instrumented with multiple cabin sensors under controlled setpoints [107].

We therefore adopt a 21 °C winter cabin reference as a pragmatic comfort target within the 20–22 °C range used in practice, acknowledging that comfort is multi-factorial (air velocity, humidity, clothing, seat location) and that modest winter setpoint reductions are acceptable for energy saving [108]. The 26 °C (daily mean) pivot conservatively captures days when sustained A/C duty is expected, recognizing that true hot-day peaks and solar gains exceed the daily mean.

From a heat-balance perspective, steady heating scales with $UA\Delta T$. For a 12 m bus, $UA \approx 350$ W/K is representative, with explicit consideration of door cycling and passenger heat [109]. With $\Delta T \approx 10$–12 K (e.g., 10 °C outdoors, ~21 °C indoors), transmission load alone is ~3.5–4.2 kW, to which infiltration and distribution losses add materially; measured FCB tests likewise show kWh-scale heating energy at standstill for ~15 K warm-ups [107].

Waste-heat availability can partially offset loads in moderate cold. Production FCBs route stack coolant through a plate heat exchanger to support cabin heating, and experiments confirm such integration. Nevertheless, multiple studies show waste heat is insufficient in deep winter, so auxiliary heaters/heat pumps are still required; integrating waste heat reduces hydrogen consumption by ≈ 5–7 % in cold (−10 … 0 °C) simulated cycles [110]. Given this evidence, 10 °C is a conservative, data-informed winter pivot: above ~10 °C, stack waste heat plus passenger gains often keep steady heating modest; below ~10 °C, $UA\Delta T$, infiltration, and defog/defrost

push the bus into an HVAC-dominated regime. Conversely, 26 °C (daily mean) captures days where solar and sensible loads typically drive sustained A/C beyond what free-cooling or intermittent cycling can handle. To remain consistent with the Modena calibration, we implement two calibrated maps: a baseline map (e.g., 9.5 kg/100 km) for 10–26 °C, and an HVAC-stress map (e.g., 14.3 kg/100 km) below 10 °C or above 26 °C. These compactly encode "A/C-off vs. A/C-on (or heater-on)" behaviour and implicitly include auxiliary overheads, consistent with measured whole-vehicle HVAC penalties. These temperature thresholds are propagated into the station-sizing analysis (Section 3.4), where daily hydrogen demand and compressor/precooling loads are evaluated under 'baseline' (10–26 °C) and 'HVAC-stress' (<10 °C or >26 °C) days. Empirical and modelling studies for 12 m buses routinely report 12–14 kW winter heating demands when doors are active, which supports adopting a 14 kW "HVAC-on" penalty for sizing.

3.3. Performance Analysis Scenarios

This section outlines the comprehensive simulation framework meticulously designed and executed to evaluate the dynamic performance, energy efficiency, and operational characteristics of the five distinct bus powertrain configurations previously developed (Diesel, CNG, HEB, EB, and FCB). The primary goal of this analytical phase is to move beyond simple component modelling towards a holistic assessment of how these different technologies perform under both standardized and realistic, localized operating conditions. Recognizing the significant impact of driving patterns on vehicle energy demand, the analytical structure was deliberately organized into two complementary and sequential phases, each addressing a distinct yet interconnected level of assessment.

All simulations were executed within the ADVISOR environment, a highly validated simulation platform developed by the NREL and built on MATLAB/Simulink. ADVISOR's modular, physics-based modelling structure allows precise representation of individual powertrain components and system interactions, offering a high degree of reliability for conventional, hybrid, electric, and fuel-cell vehicles alike. Its flexibility in defining control strategies, integrating user-defined drive cycles, and capturing auxiliary power loads makes it particularly well-suited to the multi-dimensional comparative analyses undertaken in this research.

To establish a rigorous performance baseline and to enable a balanced, multi-dimensional comparison among the five bus powertrain configurations across a wide array of operating

conditions, an extensive benchmarking framework was developed as the preliminary analytical stage. This benchmarking process, implemented through the ADVISOR simulation platform, was designed to provide standardized, reproducible, and internationally comparable performance indicators.

Four widely acknowledged urban transit driving cycles were carefully selected to represent the full operational diversity typically encountered in public transportation:

UDDS: Characterized by moderate speed fluctuations and regular stop intervals, this cycle captures typical urban driving dynamics found in mid-density North American city traffic, thereby serving as a representative baseline of average urban bus operation.

CBD-14: Distinguished by its repetitive stop-and-go motion at low speeds (average top speed around 32 km/h), CBD-14 embodies the operational environment of dense urban centres and congested transit corridors where idling and short acceleration phases dominate energy demand.

OCTA: This cycle integrates both stop-and-go urban traffic and smoother, higher-speed arterial segments, thereby providing a balanced depiction of mixed urban-suburban transit conditions. Owing to its comprehensive operational structure, OCTA is frequently regarded as a realistic benchmark for metropolitan bus operations.

MANDC: The most demanding among the four, this cycle replicates severe inner-city congestion characterized by extremely low average speeds (~11 km/h), high idle fractions, and intense acceleration and braking, thereby representing an upper-limit stress condition for urban bus powertrains.

MBDC: This locally derived, high-fidelity cycle, developed as a core part of this research (Section 3.1) using the hybrid MMAS-ABC algorithm and empirical GPS data from Modena's Linea 7, represents the specific, real-world kinematic demands encountered in the target operational environment. The following Figure 3.8 shows the driving pattern of the UDDS, CBD, OCTA, and MANDC driving cycles. The MBDC is shown in the section 4.1 of this thesis.

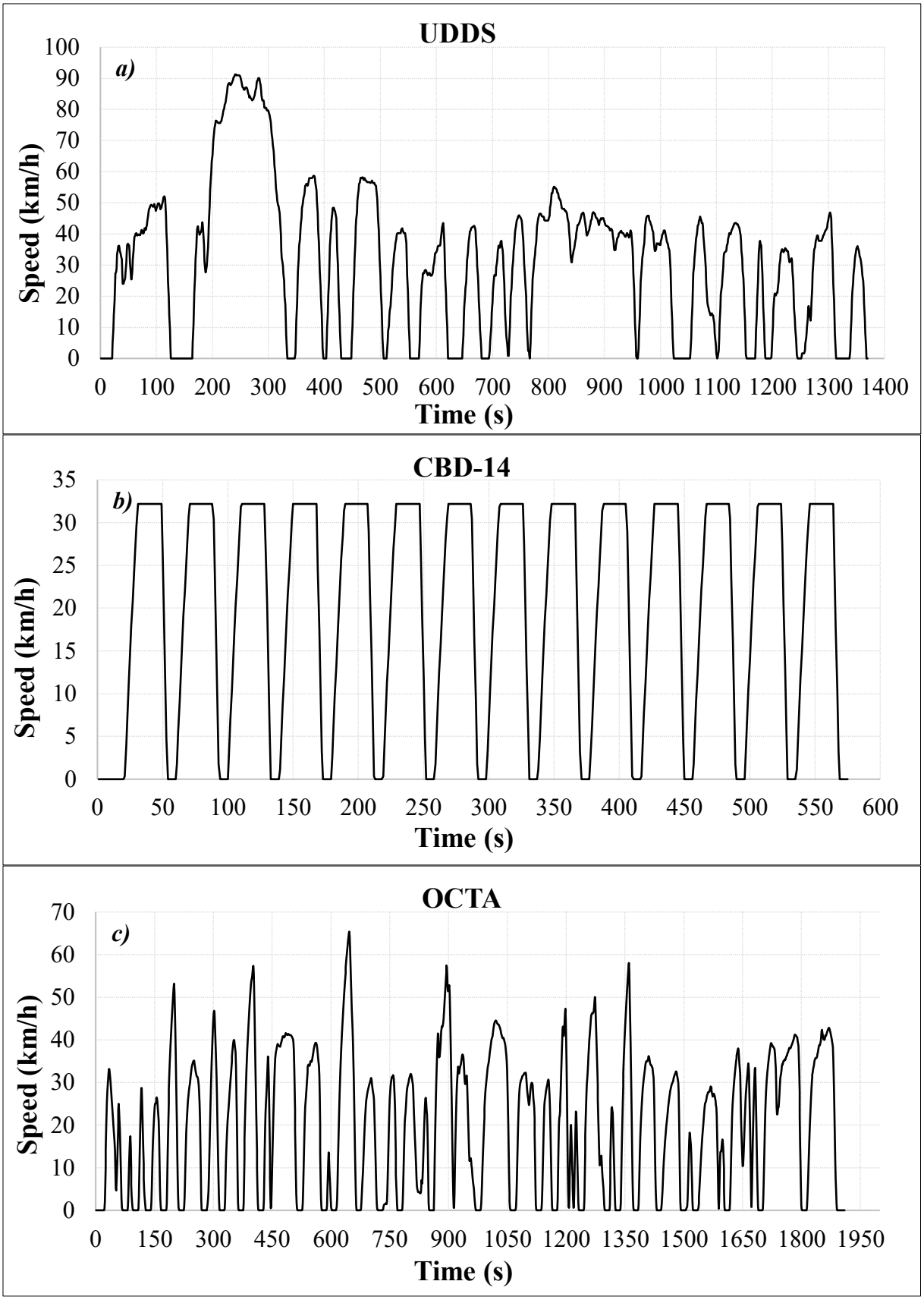
UDDS
a)
Speed (km/h)
Time (s)
0 100 200 300 400 500 600 700 800 900 1000 1100 1200 1300 1400
0 10 20 30 40 50 60 70 80 90 100
CBD-14
b)
Speed (km/h)
Time (s)
0 50 100 150 200 250 300 350 400 450 500 550 600
0 5 10 15 20 25 30 35
OCTA
c)
Speed (km/h)
Time (s)
0 150 300 450 600 750 900 1050 1200 1350 1500 1650 1800 1950
0 10 20 30 40 50 60 70

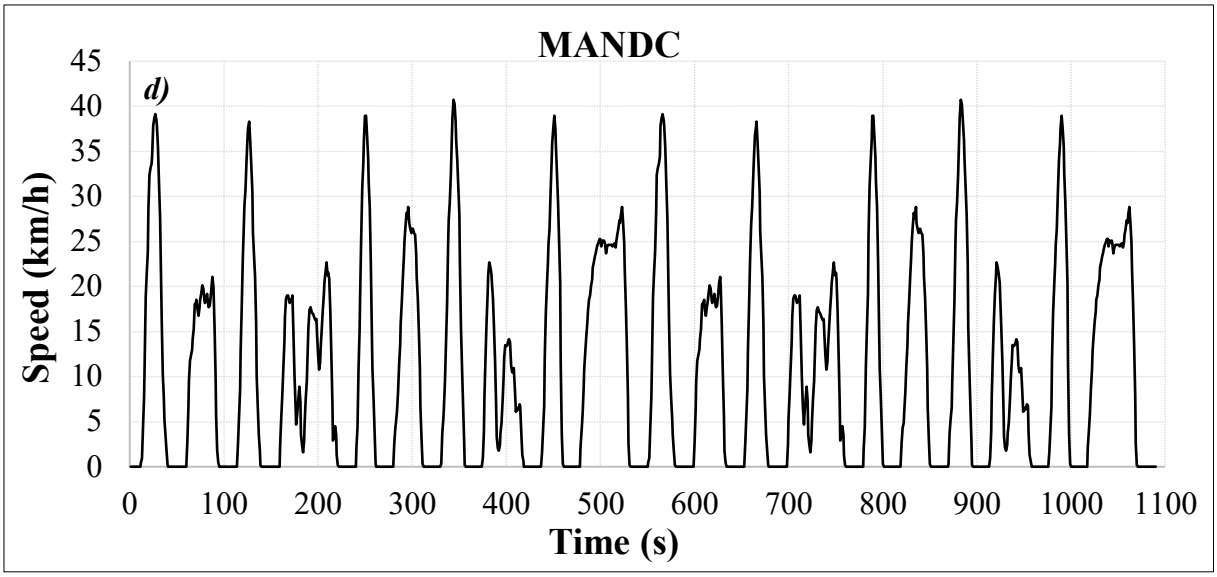

Figure 3.8. Driving Patterns of the a) UDDS b) CBD-14 c) OCTA and d) MANDC

Within this benchmarking framework, four major analyses were conducted to capture the essential aspects of powertrain performance. These benchmarking tests were specifically designed to assess various critical aspects of vehicle performance as detailed below:

- Primary Fuel/Energy Consumption Analysis: The central component of the analysis involved simulating the fuel and/or energy consumption of each of the five bus models across all five driving cycles (UDDS, CBD-14, OCTA, MANDC, and MBDC). To comprehensively evaluate the impact of auxiliary systems, a significant factor in real-world bus operation, simulations were conducted under two distinct conditions for each cycle and model combination: with the A/C system deactivated (baseline efficiency) and with the A/C system fully activated (high auxiliary load, assumed at 14 kW). All resulting consumption figures were subsequently normalized to gasoline-equivalent units (L/100 km) using standard energy content conversions (See Eq. 3.18, Section 3.2.1) to allow for direct and equitable comparisons of energy efficiency across the diverse powertrain technologies and fuel types. This comparative consumption data forms the core of the results presented in Section 4.2.
- Parameter Sensitivity Analysis: An investigation was conducted specifically on the OCTA drive cycle to quantify the influence of key inherent vehicle design parameters on baseline fuel consumption (A/C off). Three critical physical parameters were selected for this sensitivity study due to their significant impact on vehicle dynamics and energy

demand: the total bus weight, the aerodynamic drag coefficient, and the wheel radius. The methodology involved systematically varying each parameter by ±10% from its nominal value (as defined in Table 3.5), while holding the other two parameters constant at their baseline levels. This controlled variation approach allowed for the isolation and quantification of each parameter's individual contribution to overall vehicle efficiency under the mixed urban/arterial operating conditions represented by the OCTA cycle. The results of this analysis provide insights into potential optimization pathways through weight reduction, aerodynamic improvements, or tire selection.

- Performance Analysis on Graded Roads: The impact of road inclination on fuel consumption and vehicle performance was assessed using a modified version of the CBD-14 drive cycle. While the standard CBD-14 cycle has a flat elevation profile, ADVISOR allows for the incorporation of constant road grades, simulating driving on sustained inclines. Simulations were performed for fixed road inclinations of 0%, 2%, and 4%, under both A/C on and A/C off conditions. The CBD-14 cycle was chosen for this analysis primarily because its relatively low top speed helps mitigate potential issues where less powerful vehicles (particularly under high load and steep grade) might struggle to accurately follow the target speed profile, ensuring a more consistent comparison focused solely on the effect of gravitational resistance across the different technologies. (It should be noted that the 0% grade results from this specific analysis also serve as the baseline CBD consumption data).

- Gradeability Tests: To determine the maximum steady-state hill-climbing capability intrinsic to each bus model's powertrain, standard gradeability tests were performed independently of specific driving cycles. These simulations calculated the maximum sustained grade (expressed as a percentage) that each vehicle could successfully ascend while maintaining constant speeds of 20 km/h and 40 km/h. Tests were conducted with the A/C system both activated and deactivated to assess the impact of auxiliary load on peak powertrain performance under demanding conditions. These results provide crucial insights into the fundamental torque delivery and sustained power capabilities of the different powertrain architectures, critical factors for route planning and vehicle selection in areas with significant topographical variation.

By integrating these diverse analyses, including multiple driving cycles, auxiliary load conditions, parameter variations, and specific performance tests such as gradeability, this methodological framework provides a comprehensive and robust foundation for evaluating the

five bus technologies. The culminating comparison, focusing on the differences observed between the MBDC and the standard cycles, allows for a critical assessment of the value and necessity of localized driving cycle development for accurate performance prediction in the specific context of Modena.

3.4. Feasibility Assessment of a Local Hydrogen Refuelling Infrastructure

This section presents the comprehensive methodological framework developed to evaluate the practicality of deploying a localized hydrogen refuelling infrastructure. The primary goal of this analysis is to conceptualize and size an HRS specifically designed to support a potential fleet of FCBs operating within the city of Modena. This chapter marks a methodological shift in the thesis: transitioning from the vehicle-scale performance assessments of earlier chapters to a system-level and infrastructural perspective. By doing so, it establishes a bridge between the theoretical energy efficiency of hydrogen-based vehicles and the tangible infrastructure required to sustain them. The outcome is a holistic understanding of the technological, operational, and logistical feasibility of integrating hydrogen into Modena's public transportation ecosystem.

A defining and innovative feature of this framework is its direct reliance on original simulation results generated within this research. Rather than depending on generalized or literature-derived fuel consumption figures which may not reflect Modena's actual driving conditions, this analysis draws upon the specific results from the FCB simulations conducted on the MBDC. This localized, data-driven approach ensures that the resulting HRS design is accurately tailored to Modena's real-world driving behaviour, operational schedules, and geographic context.

The feasibility study is structured into three primary stages:

1. Hydrogen demand estimation, derived directly from the simulation outcomes and operational scenarios.
2. Conceptual design of the refuelling station architecture.
3. Analytical sizing of major HRS components using established engineering principles.

3.4.1. Estimation of Hydrogen Demand

The first and most fundamental step in planning a hydrogen fuelling facility is to determine the total daily hydrogen requirement it must reliably supply. In a captive fleet setting such as an

urban bus system, this calculation is relatively predictable, given the fixed nature of routes, timetables, and operating hours.

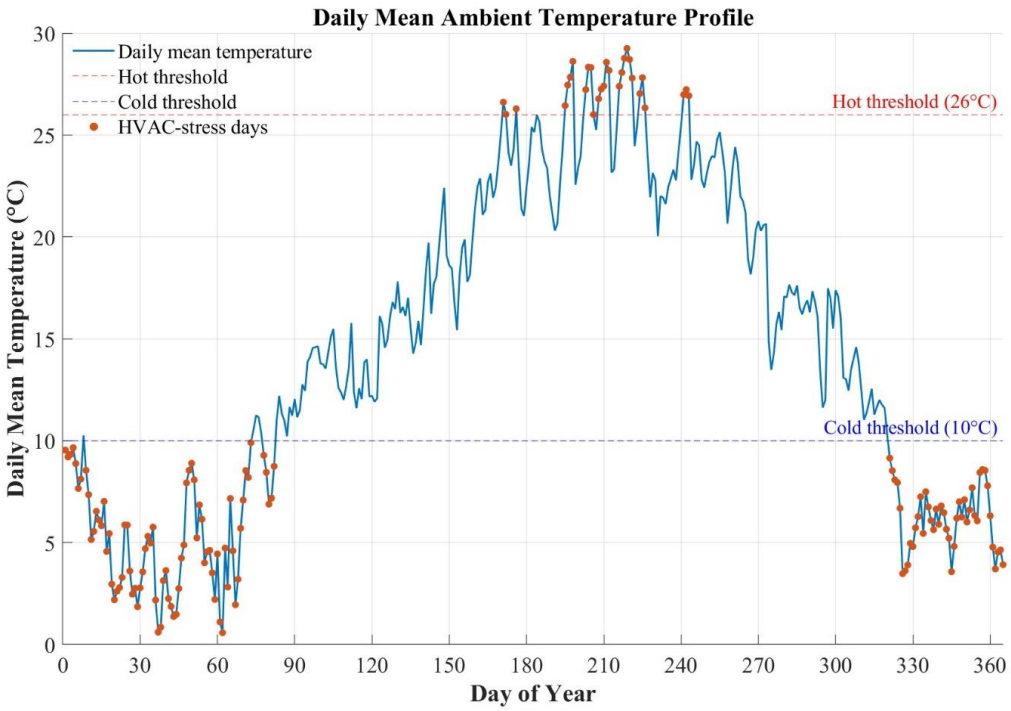

Figure 3.9. Daily Mean Ambient Temperature (°C) of Modena

Daily fleet hydrogen demand is computed by coupling the hourly ambient-temperature record with the vehicle-level HVAC threshold logic defined in the section 3.2.5. The ambient temperature driver is an 8760-element hourly series (°C) downloaded from the Photovoltaic Geographical Information System (PVGIS) portal [111] for the study location and year (non-leap). The vector is partitioned into calendar days $d = 1, \ldots, 365$, each containing 24 consecutive hourly samples. For each day d, the daily-mean ambient temperature $\bar{T}_d$ is computed. Days are then classified as HVAC-stress if $\bar{T}_d < 10°\mathrm{C}$ (heating-dominated) or $\bar{T}_d > 26°\mathrm{C}$ (cooling-dominated), and as baseline otherwise ($10 \leq \bar{T}_d \leq 26°\mathrm{C}$). Consistent with the section 3.2.5, the model applies two calibrated consumption maps: the baseline map F_{base} (e.g., 9.5 kg H_2/100 km) on baseline days and the HVAC-stress map F_{stress} (e.g., 14.3 kg H_2/100 km) on stress days. Given the number of buses N_{bus} and the per-bus daily driving distance k_d (km/bus/day; constant or time-varying), the per-day fleet hydrogen demand is:

$$D_d\,[kg/day] = N_{\mathrm{bus}}\,\frac{k_d}{100} \times \begin{cases} F_{\mathrm{stress}}, \bar{T}_d < 10°\mathrm{C} \text{ or } \bar{T}_d > 26°\mathrm{C} \\ F_{\mathrm{base}}, 10 \leq \bar{T}_d \leq 26°\mathrm{C} \end{cases} \tag{3.20}$$

Summing D_d over the year yields the annual fleet hydrogen demand D_a. Figure 3.9 shows the daily-mean ambient temperatures over the year in Modena.

3.4.2. Conceptual Design of the Hydrogen Refuelling Station

The proposed HRS adopts an on-site hydrogen generation model, in which hydrogen is produced locally and immediately supplied to storage and dispensing units. This configuration was selected to complement the vision of a locally sourced green hydrogen network, potentially supplied by biomass-derived feedstocks, while simultaneously eliminating transportation costs and the logistical complexity of external hydrogen delivery.

The conceptual layout of the proposed station, illustrated in Figure 3.10, is designed to ensure safe, efficient, and continuous high-pressure hydrogen delivery to buses. The process unfolds through the following sequential stages:

1. Hydrogen Generation: Hydrogen is produced via a localized process, such as electrolysis or biomass gasification, depending on available feedstock sources.
2. Low-Pressure Storage: The produced hydrogen is first collected in a low-pressure buffer tank, which stabilizes the flow from the production unit and acts as an intermediate storage stage.
3. Compression: A multi-stage compressor draws hydrogen from the buffer tank and increases its pressure substantially. This step represents the most energy-intensive operation in the station, as it provides the potential energy required for both high-pressure storage and vehicle refuelling.
4. High-Pressure Storage: The compressed hydrogen is transferred into a cascade system of high-pressure tanks, which serve as the station's principal storage reservoir. These tanks enable rapid hydrogen transfer during refuelling operations.
5. Pre-Cooling and Dispensing: Before fuelling, hydrogen passes through a pre-cooling system, which reduces its temperature to mitigate the thermal effects caused by rapid compression during dispensing. Finally, the cooled, high-pressure hydrogen is delivered to the vehicle via dispensers, typically operating at 350 bars for heavy-duty bus applications.

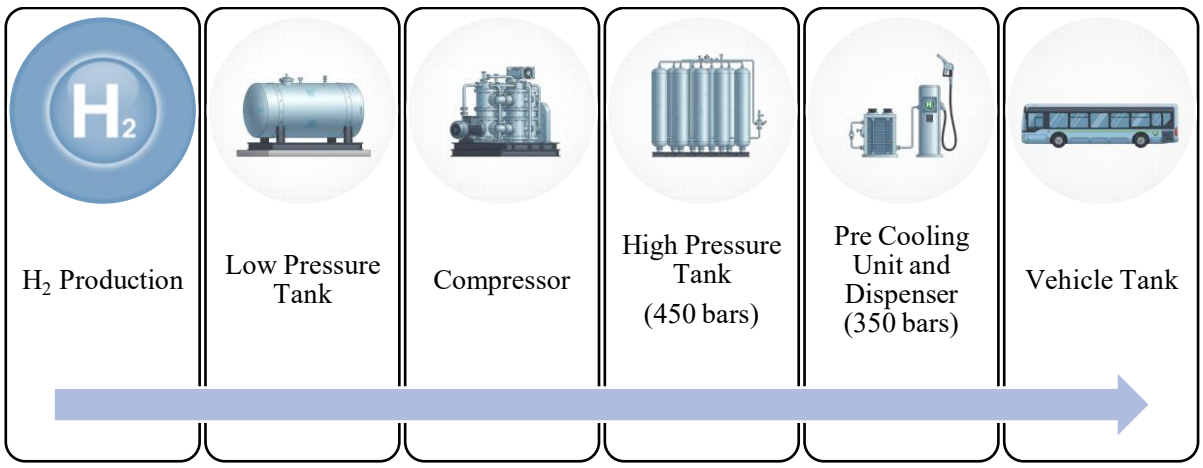

Figure 3.10. Conceptual Schematic of the Proposed Hydrogen Refuelling Station

This stepwise configuration supports operational efficiency, safety compliance, and scalability, making it suitable for future expansion as hydrogen demand grows [112–114].

3.4.3. Analytical Sizing of Key Components

The sizing process is based on a dynamic simulation model in MATLAB that considers the fleet's instantaneous and daily fuel demands, the impact of environmental conditions on consumption, and overall system reliability. The methodology begins with determining the demand, extends to calculating the mass and volume of the High-Pressure (HP) and Low-Pressure (LP) storage tanks, and subsequently determines the work and power requirements for the main compressor and the production (booster) compressor. Finally, the energy consumption model for the Electric Pre-Cooling Unit (EPCU), required for cooling during refuelling, is described.

Let the worst-case daily fleet demand computed in section 3.4.1 be $D_{day,worst}$ [kg/day]. The mass capacities of the HP and LP tanks are calculated based on the determined worst-case daily demand $D_{day,worst}$, with an added operational safety margin, considering the similar studies in this field [113,115–117]. A safety factor SF_{HP} of 1.2 is used in the simulation model. This factor provides a buffer against potential downtime in production or compression, unexpected demand surges, or the need for flexibility in refuelling strategies.

$$C_{HP,kg} = D_{day,worst} \cdot SF_{HP} \tag{3.21}$$

With this approach, the HP storage system is sized to hold 120% of the fleet's daily demand.

The physical volume of the HP tank is calculated using the ideal gas law $PV = mRT$ to ensure it can store the determined mass capacity at the nominal storage pressure. For simplicity in this simulation model, the compressibility factor for hydrogen (Z = 1) is assumed [59].

The HP storage volume V_{HP} is determined using these parameters as follows:

$$V_{HP} = \frac{C_{HP,kg} \cdot R_{spec} \cdot T_{HP}}{P_{HP,nom}} \tag{3.22}$$

Here, $C_{HP,kg}$ is the calculated storage mass m, $P_{HP,nom}$ is the nominal HP storage pressure P, (45 MPa or 450 bars), T_{HP} is the average storage temperature T (300 K) and R_{spec} is the specific gas constant for hydrogen, 4124 J/(kg·K).

The LP storage tank acts as an intermediate buffer, temporarily storing hydrogen from the 1-bar production source (e.g., biomass) before it is drawn by the main (LP → HP) compressor. This tank typically operates within a pressure band of 2 bar to 5 bar. The LP storage capacity ($C_{LP,kg}$) is determined proportionally to the HP storage capacity. Based on common industry practices and the need for an intermediate stock to support continuous compressor operation, the LP mass capacity is defined as 20% of the HP capacity.

$$C_{LP,kg} = 0.20 \times C_{HP,kg} \tag{3.23}$$

The volume of the LP tank is also calculated using the ideal gas law (Z = 1), sized to hold its mass capacity at the maximum operating pressure ($P_{LP,max}$). Although the LP tank operates between 2-5 bar, the upper limit of 5 bar is used as the reference for the volume calculation for simplification. If we consider the ideal gas law:

$$m = C_{LP,kg} \text{ (Calculated LP mass)} \tag{3.24}$$

$$P = P_{LP,max} \text{ (Maximum LP operating pressure, 5 bar)} \tag{3.25}$$

$$T = T_{LP} \text{ (Average storage temperature, 300 K)} \tag{3.26}$$

The LP storage volume (V_{LP}) is then calculated [118]:

$$V_{LP} = \frac{C_{LP,kg} \cdot R_{spec} \cdot T_{LP}}{P_{LP,max}} \tag{3.27}$$

Two main compression processes occur at the station: 1) From production to the LP tank and 2) From the LP tank to the HP tank (Main Compressor). The capacity of the main compressor (maximum mass flow rate, kg/s) is determined by how quickly it can refill the HP tank. This defines how fast the station can "recover" after high demand. In the model, it is assumed that the compressor can fill the entire HP tank $C_{HP,kg}$ from an empty state to nominal pressure in 12 hours ($t_{fill,hours}$). Although a shorter refuelling duration is feasible, achieving this requires a larger compressor capacity, which consequently increases compressor cost.

$$\dot{m}_{comp,max} = \frac{C_{HP,kg}}{t_{fill,hours} \times 3600\ (s)} \tag{3.28}$$

This $\dot{m}_{comp,max}$ (kg/s) value limits the maximum mass the compressor can move per time step dt in the simulation.

In this study, both the main LP → HP compressor and the LP production booster (1 bar → 2–5 bar) are modelled using the classical single-stage adiabatic compression expression for ideal gases. At every simulation step, the compressor inlet and outlet pressures are read from the current LP and HP states, and the effective pressure ratio is defined as $PR = P_{out}/P_{in}$. The specific work required to compress 1 kg of hydrogen is evaluated as [117]:

$$w_{spec} = \frac{C_p \cdot T_h}{\eta} \left[(PR)^{\kappa-1/\kappa} - 1\right] \tag{3.29}$$

In this equation, C_p shows the specific heat at constant pressure for hydrogen, T_h is the compressor inlet temperature of the hydrogen, η is the adiabatic efficiency and κ is the adiabatic index, which is 1.4 for the hydrogen [115,117]. In this study, it was assumed the adiabatic efficiency of the compressor is equal to 75% [117].

In each step of the simulation, the instantaneous electrical power is computed from the mass flow rate of the hydrogen ($\dot{m}_{hydrogen}$) realized within the step [59,117]:

$$P_{kW} = \frac{w_{spec} \times \dot{m}_{hydrogen}}{1000} \tag{3.30}$$

and the step energy (kWh) is accumulated as:

$$E_{step} = \frac{w_{spec} \cdot \dot{m}_{moved}}{3.6 \times 10^6} \tag{3.31}$$

It should be noted that $\dot{m}_{hydrogen}$ denotes the actual mass flow rate (kg/s) realized within that time step, while $\dot{m}_{moved} = \dot{m}_{hydrogen}\,\Delta t$ is the total mass that is effectively transferred during that time step.

To refuel in accordance with protocols, the high-pressure hydrogen must be cooled before it reaches the dispenser. This process is handled by the EPCU. Instead of directly sizing the EPCU's cooling capacity (kW), its energy consumption is calculated based on an empirical model. This model assumes that the specific energy required for cooling (kWh/kg) depends on two main factors [113,117].

1. Ambient Temperature (T_{amb}): The higher the ambient temperature, the greater the cooling load.
2. Dispensed Mass Flow (DD_{H_2}): The daily amount of hydrogen dispensed.

The specific EPCU energy consumption ($E_{PCU,spec}$) is estimated by [113,117].

$$E_{PCU,spec} = \frac{0.3}{1.6e^{-0.018T_{amb}}} + \frac{25\ln(T_{amb}) - 21}{DD_{H_2}} \tag{3.32}$$

The objective of this section is station-level sizing rather than high-fidelity transient thermodynamics. Therefore, the adopted formulation intentionally preserves a reduced set of assumptions: hydrogen is treated as an ideal gas, storage temperature is taken as 300 K, compressor work is evaluated using the classical single-stage adiabatic expression, and refuelling is represented through a nominal fixed-duration transfer. These simplifications are consistent with previous station sizing studies where the focus is annual throughput and compressor energy budgeting, not nozzle-level dynamics or SAE J2601 transient pressure-controlled filling. The presented model thus maintains analytical tractability while remaining sufficiently accurate for comparative infrastructure evaluation.

3.4.4. Green Hydrogen Production Potential for the Hydrogen Refuelling Station

Biohydrogen generation in this study is linked to the biodegradable share of municipal refuse that is handled at the Carpi processing plant. The plant's throughput characteristics and mass transfer patterns were evaluated, and different engineering routes for turning this biogenic fraction into hydrogen were reviewed. Because most of this biodegradable feedstock is traced

back to household and agricultural streams [119], anaerobic bioconversion was taken as the dominant conversion route.

A processing configuration for this organic municipal waste stream was defined in which raw biogas is first upgraded to biomethane. The methane-enriched stream is then channelled to steam methane reforming, after which the resulting syngas is subjected to the water–gas shift reaction. Finally, hydrogen is isolated and polished by means of pressure swing adsorption to obtain a purified product suitable for fuel applications.

$$CH_4 + H_2O \rightarrow CO + 3H_2$$

$$CO + H_2 \rightarrow CO_2 + H_2O$$

The energetic performance of this conversion chain, expressed as the lower heating value (LHV) ratio between hydrogen produced and biomethane supplied, can be estimated at roughly 77% [120,121]. When an LHV of 45.4 $MJ \cdot kg^{-1}$ is used for biomethane [120] and 120 $MJ \cdot kg^{-1}$ is applied for hydrogen [122], the resulting stoichiometric calculation gives a theoretical production level on the order of 0.29 kilograms of hydrogen for each kilogram of biomethane.

The potential methane output obtainable from this organic municipal feedstock spans roughly 177 – 580 NL for each kilogram of total volatile solids [123]. With total volatile solids representing about 73 % of the dry matter [124] and the incoming waste containing approximately 50 % moisture [125], this interval corresponds to nearly 64.6 – 211.7 NL of biomethane per kilogram of Organic Fraction of Municipal Solid Waste (OFMSW) entering the treatment plant. Using a methane density of around 0.7 $kg \cdot m^{-3}$ under standard reference conditions (273.15 K and 0.101325 MPa) [126], this range converts to approximately 45.22 – 148.19 kg of biomethane on a per-ton basis of OFMSW. Applying the hydrogen yield derived earlier, this biomethane potential can be associated with about 13.11 – 42.98 kg of hydrogen per metric ton of treated OFMSW. For subsequent estimations, a conservative benchmark of 15 kg H_2 per ton of OFMSW is selected to quantify the hydrogen generation potential of the Carpi waste stream.

The facility also manages a notable stream of woody biomass originating from maintenance of vegetation and lawn management activities, which comprises discarded timber, pruning residues from urban green areas, and materials linked to hydrogeological rehabilitation interventions [119]. In the case of this lignocellulosic input, thermochemical gasification is considered a viable conversion pathway. This process involves subjecting carbon-rich solids to

elevated temperatures so as to form a fuel gas mixture containing hydrogen, carbon monoxide, nitrogen, carbon dioxide, water vapour, and light hydrocarbons [127]. Employing steam as the gasifying medium is known to favour more hydrogen-rich synthesis gas compositions [128]. Additionally, to raise the hydrogen fraction in the produced syngas, the water–gas shift reaction is conventionally deployed. Finally, to achieve the purity thresholds required for proton exchange membrane fuel cell operation, hydrogen can be separated and refined by pressure swing adsorption [129].

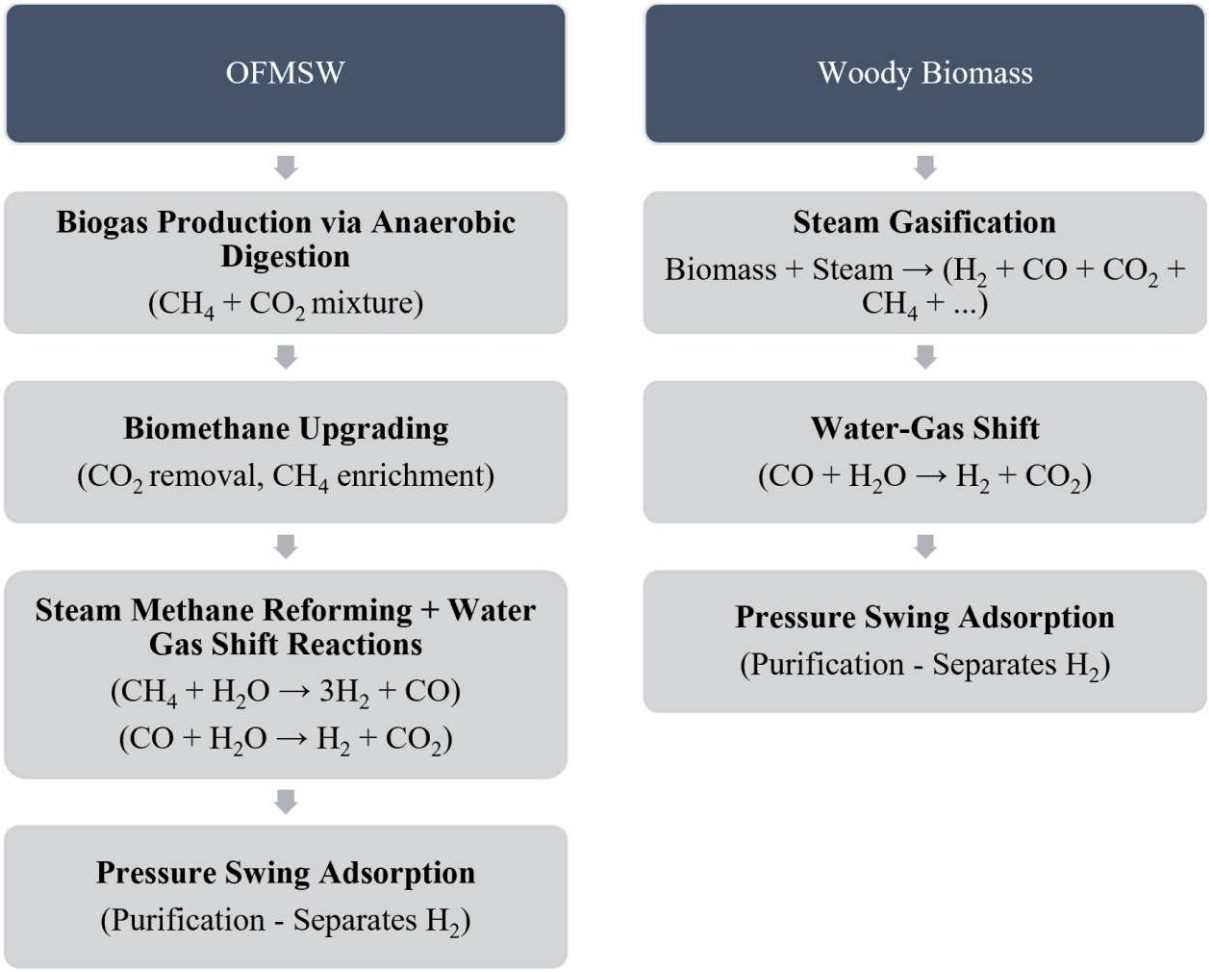

Figure 3.11. Hydrogen Production from the OFMSW and Woody Biomass

Demol et al. [130] simulated a 20 MW plant configuration incorporating oxygen–steam gasification together with catalytic steam reforming and subsequent water–gas shift conversion. In their case study, hydrogen was isolated through a hybrid separation train featuring both membrane units and pressure swing adsorption, delivering an output of roughly 79 grams of hydrogen per kilogram of moisture-free biomass. In the present assessment, a more cautious conversion factor of 60 grams of hydrogen per kilogram of dry biomass is applied. Figure 3.11 shows the hydrogen production pathway from two different biomass sources.

4. RESULTS

4.1. Driving Cycle Development Results

This section presents the core findings obtained through the implementation of the proposed driving cycle generation techniques. To provide a consistent reference point for comparative assessment, the analysis begins with a characterization of the aggregated raw driving dataset, which functions as the empirical baseline. Subsequently, the cycles synthesized using the MCMC approach and the hybrid MAX–MIN Ant System coupled with the Artificial Bee Colony (MMAS–ABC) algorithm are described in detail, and their respective performances are systematically evaluated against the defined benchmark.

4.1.1. Characteristics of Modena Real Driving Data

To establish a reliable empirical reference for this research, fundamental performance parameters were computed for each of the ten distinct bus trips recorded within the Modena network. A concise statistical overview of these indicators is summarized in Table 4.1. The analysis revealed notable variability in maximum speeds, ranging between 36.4 km/h and 53 km/h, with a mean peak value of 44.66 km/h. Across the entire dataset, the mean overall velocity (v_a) was determined as 12.85 km/h, while the mean running speed (v_r) which is calculated only when the vehicle was in motion reached 18.96 km/h, underscoring the significant portion of time spent idling.

Table 4.1. Statistical Overview of the Performance Parameters

Trip	v_a (km/h)	v_r (km/h)	a (m/s^2)	d (m/s^2)	RMS (m/s^2)	P_i, %	P_a, %	P_c, %	P_d, %	P_{cr}, %
1	14.50	21.46	0.90	-0.84	0.89	32.43	25.82	5.73	29.98	0.47
2	14.13	20.56	0.81	-0.77	0.80	31.27	26.97	6.09	29.79	0.82
3	12.19	18.53	0.69	-0.67	0.68	34.23	26.11	7.15	27.79	0.22
4	12.91	19.02	0.74	-0.75	0.74	32.14	27.30	6.77	28.57	0.42
5	13.04	19.39	0.75	-0.75	0.75	32.77	26.91	6.14	27.86	0.85
6	12.39	18.49	0.71	-0.67	0.69	33.02	25.54	8.47	27.66	0.54
7	11.42	16.85	0.56	-0.47	0.47	32.27	22.11	13.55	27.75	0.33
8	12.66	19.22	0.79	-0.67	0.72	34.11	23.83	6.98	29.75	0.55
9	11.86	17.29	0.57	-0.55	0.54	31.41	24.63	10.35	27.52	0.43
10	13.39	18.79	0.70	-0.63	0.66	28.76	26.37	8.94	30.71	0.98
Mean	12.8467	18.9598	0.7211	-0.6758	0.6939	32.2405	25.5596	8.015	28.7385	0.5609

The acceleration and deceleration profiles observed reflected typical stop-and-go urban traffic dynamics, yielding an average positive acceleration (a) of 0.721 m/s^2 and a corresponding deceleration (d) of –0.676 m/s^2. The overall intensity of these fluctuations was further captured through the Root Mean Square (RMS) acceleration value of 0.694 m/s^2.

Modal distribution analysis provided additional insight, showing that roughly 32.24% of total driving time was spent idling (P_i), whereas acceleration (P_a) and deceleration (P_d) phases accounted for approximately 25.56% and 28.74%, respectively. In contrast, steady-state cruising (P_c) represented only 8.02% of the total duration, with creeping operation (P_{cr}) limited to 0.56%. Collectively, these quantified behaviors and their variability define the empirical performance envelope that the subsequently generated synthetic driving cycles are intended to emulate.

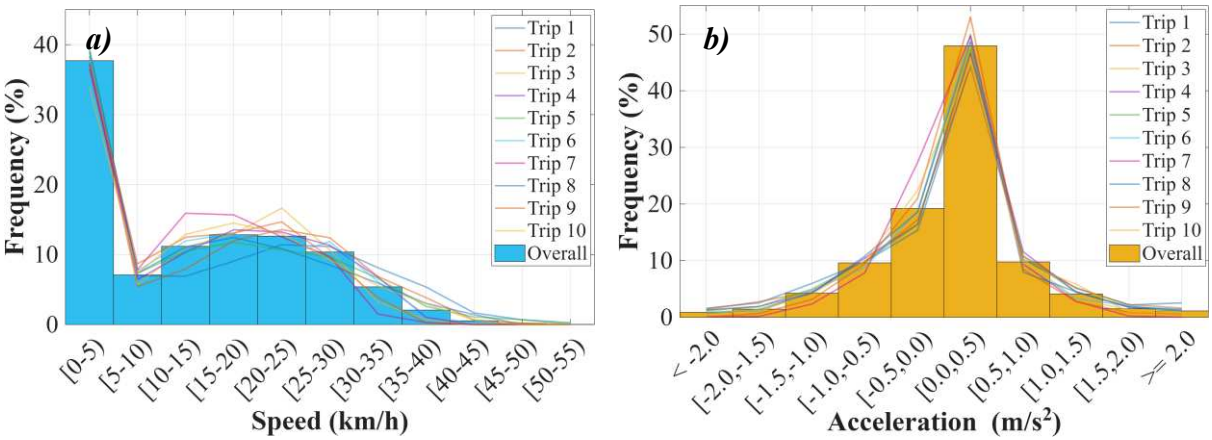

Figure 4.1. Frequency distributions for (a) speed and (b) vehicle acceleration

The statistical distributions of both speed and acceleration extracted from the recorded dataset are depicted in Figure 4.1. In this visualization, bar plots illustrate the aggregated data encompassing all trips, while the profiles of the ten individual routes are superimposed as semi-transparent lines to emphasize variation among trips.

The analysis of the speed histogram (Figure 4.1a) highlights a distinct pattern dominated by low-velocity operation. The most notable feature is a sharp frequency concentration in the 0–5 km/h range, accounting for 37.71% of the total driving duration. Beyond this range, the frequency drops steeply before a secondary cluster appears between 10 and 20 km/h, indicating that most vehicle movement (apart from idling) occurs within low-to-moderate speed intervals. As speed increases above approximately 20–25 km/h, the occurrence of such higher velocities

becomes progressively less frequent, with driving events above 40 km/h remaining relatively rare.

The acceleration distribution presented in Figure 4.1b follows a similar concentration trend. The majority of data points fall within the 0 to 0.5 m/s^2 interval, which alone represents 47.92% of the total operating time. This observation suggests that the buses typically function under near-steady-state conditions, characterized by minimal acceleration and braking activity. Such behaviour aligns with the dynamics of dense urban traffic, where vehicles spend extended periods idling, cruising steadily, or performing gentle speed transitions.

To provide a more comprehensive understanding of the interaction between speed and acceleration, Figure 4.2 illustrates a three-dimensional frequency distribution combining these two variables. This surface map displays the relative duration spent at each speed–acceleration state. A single, dominant concentration region is observed, representing roughly 31.93% of the entire operational time. This cluster is centred around very low speeds (0–5 km/h) and near-zero accelerations (0–0.5 m/s^2). Such a pronounced accumulation confirms that the majority of driving activity involves idling phases or slow manoeuvres requiring minimal throttle or braking input, an expected outcome given the frequent stops, traffic signals, and congestion typical of urban bus routes.

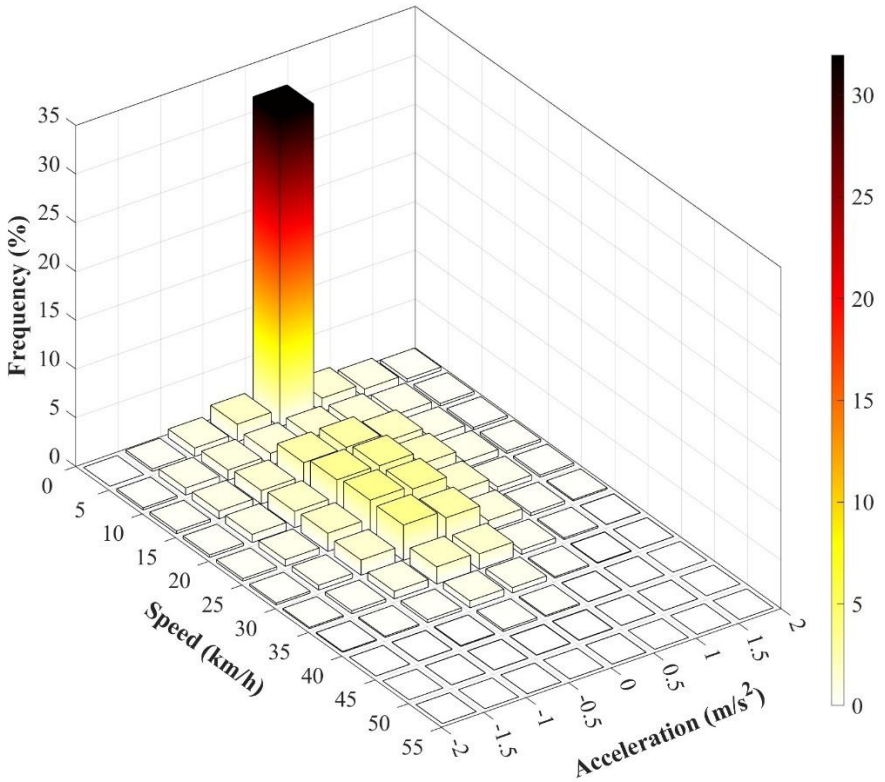

Figure 4.2. Three-Dimensional Speed - Acceleration Map of the GPS Recordings

4.1.2. Characteristics of Developed Driving Cycles

4.1.2.1. Driving Cycle Generated by Markov Chain Monte Carlo Method

A representative driving cycle for the city of Modena was constructed utilizing the MCMC methodology previously described in Section 3.1.2.1. The final selection among the candidate cycles was based on minimizing a specifically defined cost function, ensuring the most accurate reproduction of the real driving behaviour. To evaluate how the simulation length influences the statistical representativeness of the generated cycle, multiple candidate profiles were created using different Monte Carlo Trial (MCT) counts. Each of these cycles was then compared to the empirical dataset, and their corresponding error metrics were assessed.

The comparative analysis revealed a consistent trend: as the number of MCTs increased, the mean percentage error across all principal performance parameters decreased progressively. This convergence characteristic of the MCMC approach, indicating improved fidelity with higher iteration counts, is illustrated in Figure 4.3. The results demonstrate that the cycle generated using 100,000 MCTs achieved the lowest mean error value of 1.16%, when evaluated against the aggregated Modena dataset across ten key performance indicators. Consequently, the driving cycle corresponding to this MCT configuration was identified as the most statistically representative output and selected for subsequent in-depth examination.

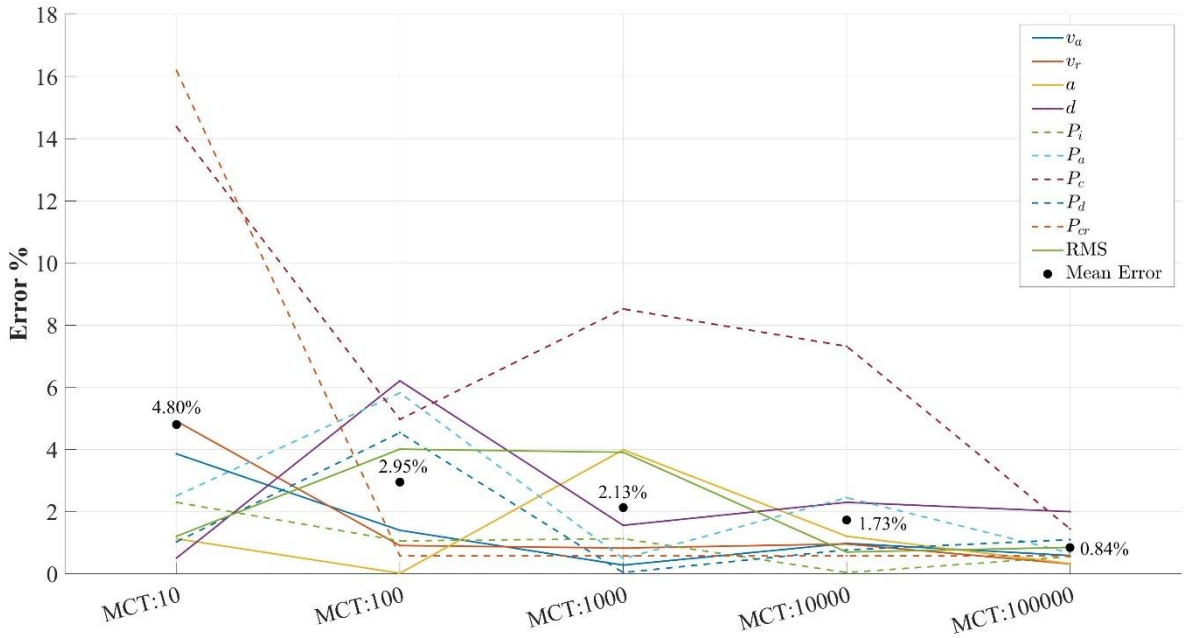

Figure 4.3. Convergence trend of the MCMC-generated cycles with increasing Monte Carlo Trials

The speed–time trajectory of the chosen MCMC-generated cycle is presented in Figure 4.4, which provides a second-by-second depiction of the synthesized driving behaviours typical of Modena's urban operating conditions. The profile clearly captures the stochastic fluctuations and transient dynamics that characterize real-world city bus operations, making it a suitable benchmark for the performance and energy analysis stages discussed in the following sections.

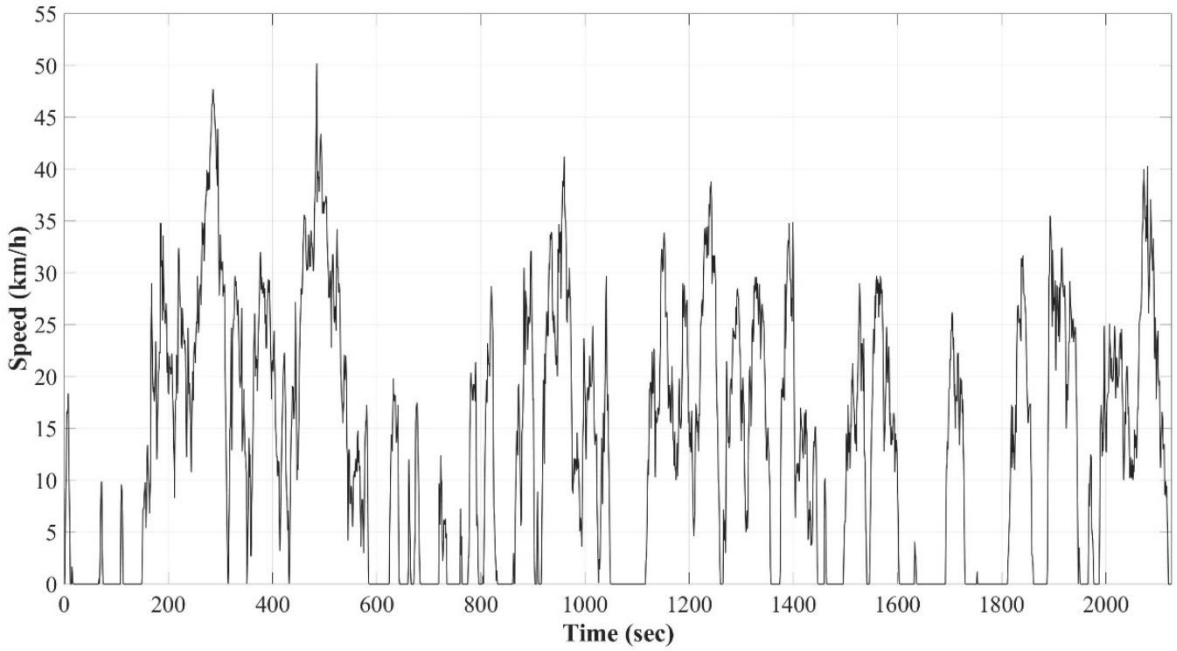

Figure 4.4. Time–velocity profile of the MCMC Developed Driving Cycle

4.1.2.2. Driving Cycle Generated by Hybrid MMAS-ABC Method

To highlight the importance of a systematic parameter calibration process for the MMAS algorithm, a preliminary sensitivity analysis was performed. In this initial stage, the parameters α, β, and ρ were fixed at values (α = 4, β = 2, ρ = 0.3) previously identified as effective in a related driving cycle study by Cui et al. [2]. The analysis then concentrated on examining the influence of the pheromone update constant (Q) on the algorithm's overall accuracy. The average percentage deviation between the MMAS-generated driving cycle and the original Modena GPS dataset was computed for different Q values. Considerable performance fluctuations were observed: the mean deviation was 13.85% at Q = 1, increased sharply to 32.41% at Q = 10, slightly decreased to 28.26% at Q = 100, reached its lowest value of 24.22% at Q = 500, and then rose again to 39.74% at Q = 1000.

These results clearly demonstrate that even a single-parameter adjustment can cause large variations in model performance. This variability exposes the limitations of applying fixed parameter values obtained from literature to datasets with distinct driving patterns, such as

Modena's. Consequently, an automated and holistic parameter optimization procedure was adopted to refine all MMAS parameters simultaneously. To achieve this, the hybrid MMAS–ABC optimization framework, previously described in the section 3.1.2.3. The search domains for the parameters were defined within the following lower (L_B) and upper (U_B) bounds: $\alpha \in [0.1, 5.0]$, $\beta \in [0.1, 5.0]$, $\rho \in [0.01, 1.0]$, and $Q \in [1, 1000]$. Within the ABC configuration, a colony of 40 bees was employed, running for a maximum of 25 cycles, with an abandonment limit of 10 for solutions showing no improvement. During each fitness evaluation step in an ABC cycle, the MMAS core was executed for 100 iterations using 50 ants, averaged across four runs to ensure stable cost estimation.

Through this iterative optimization, the hybrid approach successfully converged to an optimal parameter configuration: $\alpha = 0.1$, $\beta = 0.98$, $\rho = 0.01$, and $Q = 200$. The convergence pattern of this process is shown in Figure 4.5, which depicts the reduction in the MMAS cost function (Eq. 3.7) across the ABC cycles. The figure illustrates the continuous decline of the total cost, corresponding to the overall error of the generated driving cycle at each iteration. Notably, a sharp drop is observed during the early cycles, indicating the ABC algorithm's strong exploratory capacity and rapid convergence toward a stable minimum.

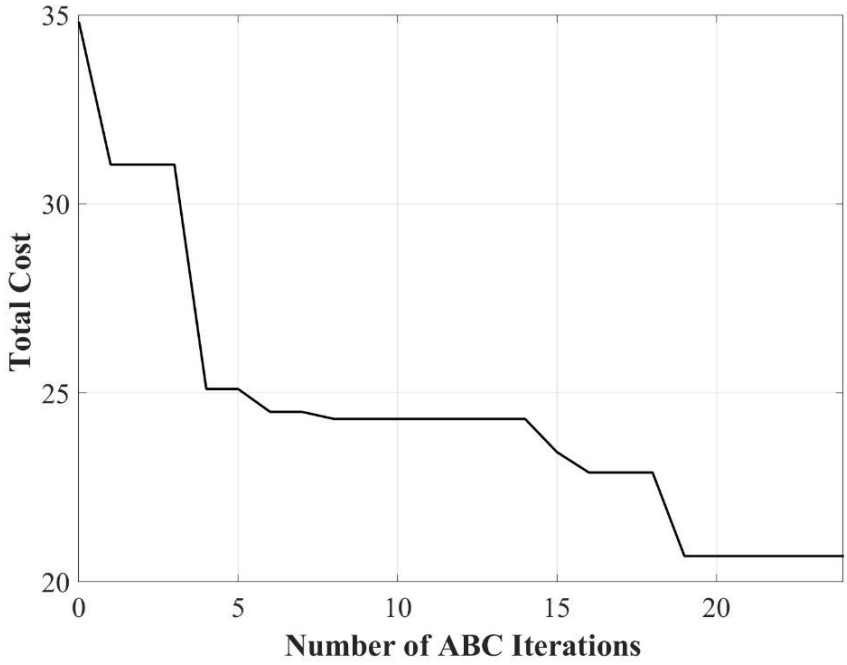

Figure 4.5. Cost vs. Number of ABC Iterations

Using these optimized parameters, the MMAS algorithm was rerun to generate the final representative driving cycle for Modena. The optimized hybrid MMAS–ABC cycle achieved an exceptionally low average deviation of only 0.76% across the ten key performance indicators

when compared with the aggregated reference dataset. The speed–time profile of this optimized cycle is shown in Figure 4.6, while a detailed comparative evaluation of its performance relative to both the original Modena data and the MCMC-generated cycle is presented in Section 4.1.2.3.

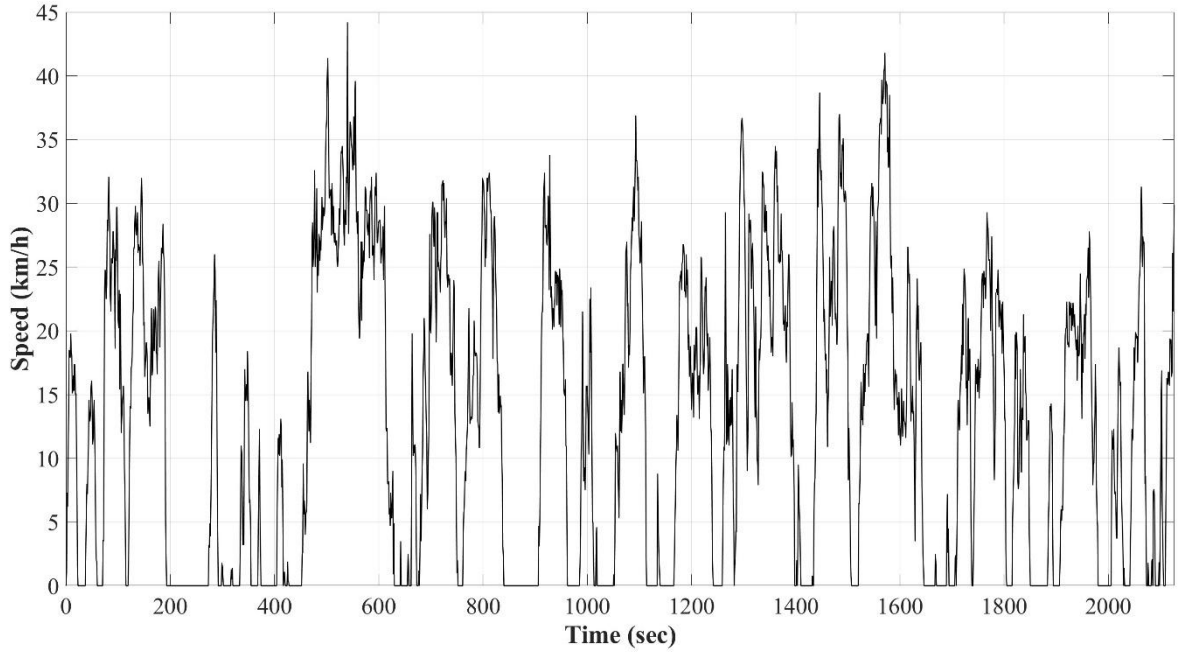

Figure 4.6. Speed–time trajectory of the optimized hybrid MMAS–ABC representative driving cycle for Modena

4.1.2.3. Comparison of the Generated Driving Cycles

A comparative evaluation was conducted to assess the representativeness of the driving cycles produced by the MCMC and hybrid MMAS–ABC approaches, using the aggregated Modena dataset as the reference benchmark. Table 4.2. summarizes this assessment by listing ten key performance indicators and the respective percentage deviations of each generated cycle from the empirical data.

Table 4.2. Comparison of the Key Performance Parameters

Metric	Original Data	MCMC	MCMC % Diff	Hybrid MMAS-ABC	Hybrid % Diff
v_a (km/h)	12.847	13.067	1.71	12.79	0.44
v_r (km/h)	18.96	19.314	1.87	18.827	0.70
a (m/s^2)	0.721	0.712	1.30	0.723	0.26
d (m/s^2)	-0.676	-0.686	1.52	-0.663	1.86
P_i %	32.241	32.346	0.33	32.064	0.55
P_a %	25.56	25.670	0.43	25.811	0.98

$\boldsymbol{P_c}$ %	8.015	7.851	2.04	7.945	0.87
$\boldsymbol{P_d}$ %	28.739	29.196	1.59	28.397	1.19
$\boldsymbol{P_{cr}}$ %	0.561	0.564	0.58	0.564	0.58
RMS (m/s^2)	0.694	0.6952	0.19	0.6948	0.13
Average Error %	-	-	1.16	-	0.76

The results indicate that both methods could generate driving cycles that closely reproduced the real-world Modena driving behaviours. However, the hybrid MMAS–ABC technique consistently outperformed the MCMC approach across most of the evaluated parameters. This superiority is reflected in the overall average percentage deviation, which was only 0.76% for the hybrid model compared to 1.16% for the MCMC-generated cycle.

The hybrid method's advantage was particularly evident in replicating the speed- and acceleration-related metrics. For instance, the average speed v_a was reproduced with a marginal error of 0.44% by the hybrid algorithm, whereas the MCMC cycle exhibited a 1.71% deviation. A similar pattern was observed for the average running speed v_r, where the hybrid approach achieved a 0.70% difference versus 1.87% for MCMC. Additionally, the average acceleration a was more precisely represented by the hybrid framework (deviation of 0.26%) compared to 1.30% with MCMC.

Although the average deceleration d was slightly better captured by the MCMC method (1.52% versus 1.86%), the hybrid algorithm generally demonstrated superior performance in other metrics, notably, in RMS acceleration, which was nearly identical to the original dataset (0.13% difference for hybrid versus 0.19% for MCMC).

When examining the modal time percentages, both approaches yielded strong agreement with the reference data. The MCMC method showed a slightly better match in the acceleration phase P_a with a 0.43% deviation (compared to 0.98% for hybrid) and in the idling phase P_i with 0.33% (versus 0.55%). Conversely, the hybrid MMAS–ABC cycle achieved closer matches for the deceleration phase P_d (1.19% versus 1.59% for MCMC) and cruising phase P_c (0.87% versus 2.04% for MCMC). Both methods produced an identical deviation of 0.58% for the creeping mode P_{cr}.

In summary, while both stochastic approaches effectively reproduced the essential dynamics of urban driving, the hybrid MMAS–ABC model demonstrated a more consistent and precise alignment with the empirical data, primarily due to its integrated optimization mechanism.

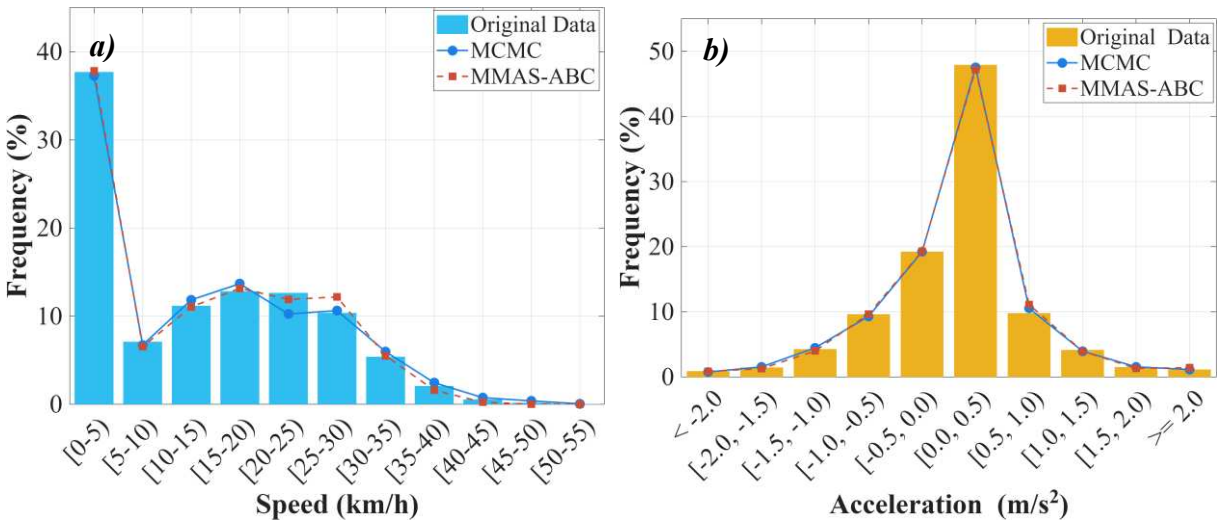

Figure 4.7. Comparison of the a) Speed b) Acceleration Distributions of the newly developed driving cycles with the original data

The distributional comparison between the generated cycles and the original Modena data is depicted in Figure 4.7. The speed distribution in Figure 4.7a reveals that both generated cycles successfully reproduced the core characteristics of the empirical dataset. The dominant frequency peak corresponding to idling and very low speeds (0–5 km/h) was accurately replicated, with frequencies of 37.28% (MCMC) and 37.85% (hybrid MMAS–ABC), closely matching the original 37.71%. The hybrid method achieved slightly better alignment in the low-to-moderate speed range (5–25 km/h), indicating improved fidelity in representing urban speed dynamics.

Similarly, the acceleration distribution shown in Figure 4.7b confirms that both methods effectively reproduced the essential dynamic features of the driving data. The primary peak within the 0–0.5 m/s^2 range which represents periods of low or near-zero acceleration was closely matched across all datasets: 47.92% in the original data, 47.53% in the MCMC cycle, and 47.2% in the hybrid MMAS–ABC cycle. The alignment extended to more extreme values as well, such as the strong deceleration range (−2.0 to −1.5 m/s^2), where the observed frequencies were 1.46%, 1.55%, and 1.27% for the original, MCMC, and hybrid datasets respectively.

The enhanced accuracy of the hybrid MMAS–ABC framework stems from its distinct methodological foundation. Unlike the MCMC approach, which relies on a stochastic random-walk process, the hybrid framework operates as a targeted optimization system. The ABC component serves as an intelligent tuning layer that systematically refines the MMAS parameters with the explicit objective of minimizing the defined cost function. This goal-driven

parameter adaptation allows the model to identify the configuration that maximizes statistical accuracy. As a result, the hybrid MMAS–ABC not only achieves higher precision for the Modena dataset but also provides a scalable and adaptable platform capable of generating representative driving cycles for diverse datasets through re-optimization.

4.1.3. Computational Cost and Sensitivity Analysis

In practical implementations, the computational efficiency of a driving cycle generation method is just as crucial as its representational accuracy. To evaluate this aspect, execution times for both the MCMC and MMAS algorithms were recorded on a system equipped with an AMD Ryzen 7 4800H processor and 16 GB of RAM, as depicted in Figure 4.8. The results clearly show that the computational demand of the MCMC approach, displayed in the left panel, grows proportionally with the number of MCTs. Achieving its most accurate output (with a 1.16% average error) required 100,000 trials, taking approximately 1008 seconds (roughly 17 minutes) to generate a representative cycle. In contrast, the right panel illustrates the scalability of a single execution of the MMAS algorithm (operating with the ABC-optimized parameters), where the final cycle which features a 0.76% deviation was completed in only 153 seconds, using 50 ants across 100 iterations.

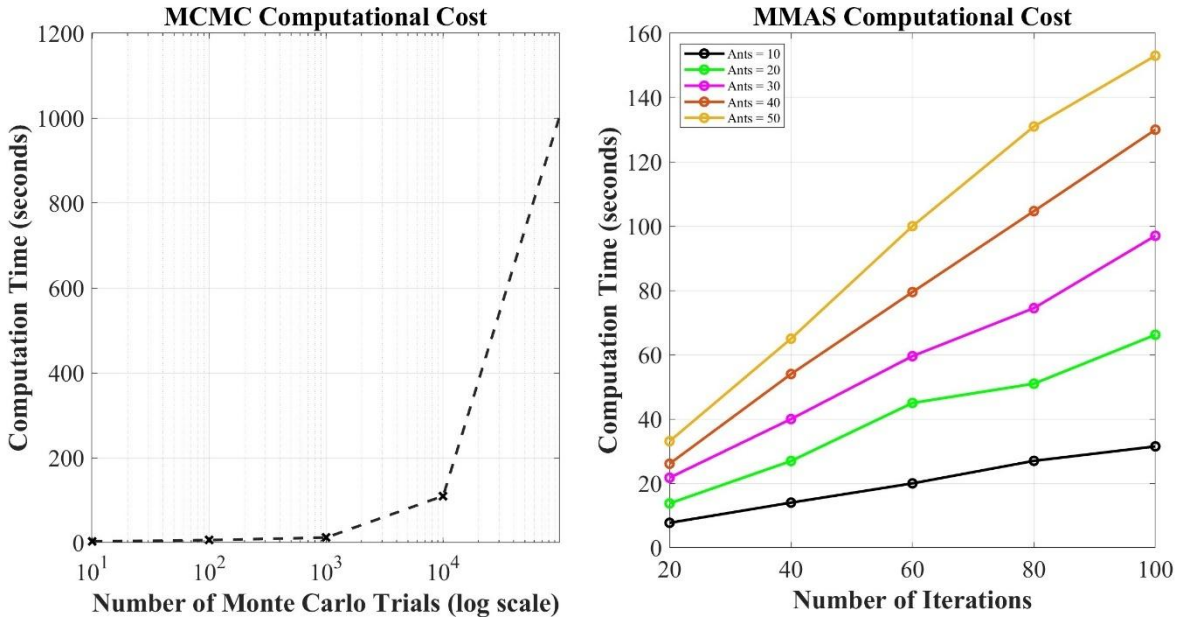

Figure 4.8. Comparison of the Computational Cost

However, it is important to distinguish the runtime efficiency of a single MMAS execution from the considerable computational investment required to obtain its optimal parameter set. The complete MMAS–ABC optimization routine required nearly nine hours to reach convergence.

Although this represents a substantial initial cost, it leads to a highly robust and efficient model configuration. Once tuned, the MMAS algorithm consistently produced driving cycles with error rates below 3%, outperforming the best results of the much longer MCMC simulations (1.16% error). This suggests that while the optimization phase introduces time overhead, future studies may focus on accelerated metaheuristic tuning to improve overall runtime. A key technical challenge during this study was the tight integration between the algorithms, as every fitness evaluation in the ABC layer necessitated a full MMAS execution, substantially increasing computational complexity.

To deepen the understanding of the MMAS framework, two complementary analyses were performed. The first was a benchmark comparison, evaluating the ABC-optimized parameter set against several configurations reported in the literature. The second was a One-at-a-Time (OAT) sensitivity analysis, designed to quantify how small deviations in individual parameters influence model accuracy.

Table 4.3. Comparison of Performance with Literature-Derived Parameter Sets

Source	α	β	ρ	Q	Average Error (%)
This Study (ABC-Optimized)	0.1	0.98	0.01	200	0.76
Tawfeek et al. [78]	0.3	1	0.4	10	2.85
Dorigo et al. [79]	1	5	0.5	100	79.88
Duan et al. [80]	3	2	0.7	10	28.30

As shown in Table 4.3, the benchmarking results clearly demonstrated that parameter configurations are not universally transferable values that perform effectively in other optimization domains yielded poor results when applied to driving cycle synthesis. This outcome reinforces the necessity of the ABC-based tuning stage. The OAT sensitivity analysis, visualized in Figure 4.9, further revealed that the model accuracy is highly sensitive to all control parameters, particularly the heuristic influence coefficient β. Even slight deviations from the optimized values led to sharp increases in error. Each parameter exhibited a distinct error–response curve, featuring a well-defined minimum at the ABC-determined optimal point. These findings strongly confirm that the ABC optimization process effectively identifies the global parameter combination that minimizes error.

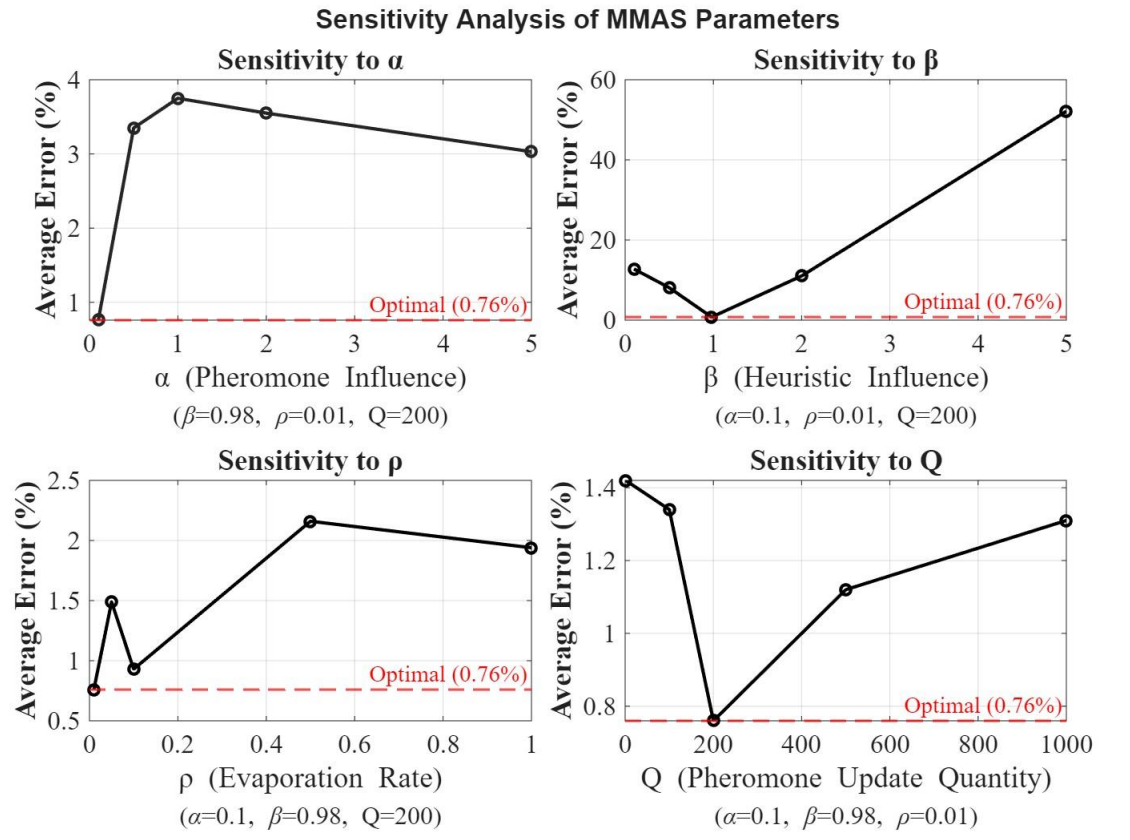

Figure 4.9. One-at-time Sensitivity Analysis

A key conclusion drawn from these investigations is that the correct selection and calibration of MMAS control parameters exert a far greater influence on model performance than the computational effort of an individual run. While an inadequately tuned MMAS may produce deviations as high as 52%, a properly optimized version consistently achieves less than 3% error with moderate computational cost. This emphasizes the critical importance of integrating a robust optimization framework such as the ABC algorithm to fine-tune sensitive parameters prior to the final driving cycle generation phase.

4.1.4. Final Modena Bus Driving Cycle (MBDC) and Its Characteristics

To situate the driving cycles generated for Modena within a broader framework, this section conducts a comparative evaluation against well-established standardized urban bus driving cycles reported in the literature. For this benchmarking effort, the cycle derived through the MMAS-ABC optimization procedure was selected, as it demonstrated superior fidelity in reproducing the aggregated driving data collected from Modena. The key performance indicators of the MBDC and those of other recognized urban bus cycles are summarized in Table 4.4.

Table 4.4 Characteristics of MBDB and other literature derived bus cycles

Study	Location	v_a (km/h)	v_r (km/h)	a (m/s^2)	d (m/s^2)	P_i %	P_a %	P_c %	P_d %	P_{cr} %	RMS
MBDC (This Study)	Modena, Italy	12.79	18.827	0.723	-0.663	32.06	25.81	7.95	28.4	0.564	0.695
Tong[29]	Hong Kong	13.41		0.931	-0.980	42.1	27.26	2.7	26.2	1.4	-
Kivekas et al. [35]	Espoo, Finland	20.42	-	0.541	-0.508	16.65	32.39	15.11	34.37	1.49	-
Nguyen et al. [34]	Hanoi, Vietnam	16.76	18.14	0.5	-0.52	7.62	34.2	14.1	32.7	11.4	0.49
Nesamani and Subramanian [131]	Chennai, India	14.0	21.6	0.65	-0.71	32.2	29.8	3.5	29.6	4.9	-
Yuhui et al. [132]	Fuzhou, China	13.8	-	0.74	-	34.4	27.0	15.5	23.1	-	-
Shen et al. [31]	Shanghai, China	23.0	-	0.71	-0.83	34.0	33.0	5.0	28.0	-	-

The comparative results indicate that the MBDC displays a distinctive dynamic pattern relative to cycles originating from other metropolitan contexts. Although all urban bus cycles inherently feature frequent start–stop events and highly variable speed patterns, the magnitude and interplay of these behaviours can vary considerably because of local operational conditions. Such conditions encompass a spectrum of factors including traffic flow intensity, street layout and gradient, scheduling strategies, passenger load variability, and even prevailing driving habits characteristic of the region. For instance, the operational rhythm which is defined by the alternation of acceleration, cruising, braking, and idling segments tends to differ not only among cities but sometimes across different routes within the same urban area.

Since the MBDC is constructed from empirical data collected along Linea 7, it accurately encapsulates the unique operational features of that specific route, such as stop frequency, dwell times at intersections, and speed constraints imposed by local infrastructure. This context-specific representation highlights an essential insight: while standardized or externally sourced cycles are valuable reference tools, they often fall short of capturing the real operational nuances and context-dependent dynamics present in a particular urban setting like Modena.

Therefore, the development of a locally tailored driving cycle such as the MBDC becomes indispensable for studies seeking high-fidelity modelling of real driving conditions. These localized cycles enable more accurate predictions of vehicle energy consumption, pollutant emissions, and powertrain efficiency. Furthermore, they provide a reliable foundation for the design and evaluation of innovative vehicle technologies and transportation policies that must

align closely with the specific mobility patterns and infrastructure characteristics of the target urban environment.

4.2. Comparative Fuel Consumption Analysis Across Driving Cycles

Fuel and energy consumption results on the MBDC were compared against those derived from four widely recognized standardized or representative urban driving cycles: UDDS, CBD-14, OCTA, and MANDC. In a deliberate shift from conventional benchmarking approaches that often utilize standard cycles as the reference, this analysis strategically employs the MBDC as the definitive baseline. This perspective allows for a direct and quantitative assessment of the extent to which these commonly adopted standard cycles deviate from the specific, empirically validated, real-world operating conditions observed in Modena. Such an approach is crucial for rigorously highlighting the potential inaccuracies, limitations, and misrepresentations inherent in relying solely on generic cycles for local performance assessments, sophisticated operational cost projections, and strategically sound technology selection processes pertinent to Modena's public transport system. Table 4.5 aggregates the comprehensive gasoline-equivalent consumption values (L/100 km) for all five distinct bus powertrain models across the complete set of five cycles, under both A/C off and on conditions. Significantly, the table explicitly calculates and presents the percentage difference of each standard cycle's result relative to the MBDC baseline, providing a clear, normalized metric of deviation from the established local reality. Complementing this tabular data, Figure 4.10 provides a detailed visual comparison structured by bus type, displaying the absolute consumption values across the five cycles through grouped bar charts, thereby enabling an intuitive interpretation of overarching trends, relative performance hierarchies, and the precise magnitude of the differences across the diverse cycle representations.

Table 4.5. Comparison of the Fuel Consumption for Different Powertrains

Vehicle	A/C	UDDS	%dif MBDC	CBD	%dif MBDC	OCTA	%dif MBDC	MAN DC	%dif MBDC	MBDC (Ref)
Diesel	Off	59	-42.83%	70.9	-31.30%	70.9	-31.30%	113.9	10.37%	103.2
	On	69.2	-46.52%	86.3	-33.31%	87.4	-32.46%	145.8	12.67%	129.4
CNG	Off	72.1	-46.15%	88	-34.28%	87.3	-34.80%	138.8	3.66%	133.9
	On	81.6	-49.91%	102.7	-36.96%	106.9	-34.38%	170.3	4.54%	162.9
HEB	Off	39.4	-58.17%	52.9	-43.84%	55.3	-41.30%	81.5	-13.48%	94.2
	On	40	-62.96%	58.6	-45.74%	57.9	-46.39%	89.4	-17.22%	108
EB	Off	24.9	-40.57%	28	-33.17%	29.9	-28.64%	42	0.24%	41.9
	On	30.5	-44.65%	36.3	-34.12%	38.4	-30.31%	57	3.45%	55.1

FCB	Off	30.8	-24.51%	28.5	-30.15%	40.5	-0.74%	55	34.80%	40.8
	On	39.1	-36.32%	46.7	-23.94%	55.2	-10.10%	80.6	31.27%	61.4

The most prominent and overarching finding, powerfully underscored by both the numerical data in the final Table 4.5 and the visual representation in Figure 4.10, is the substantial and pervasive deviation of all four standard cycles from the MBDC results. This finding comprehensively validates the central argument of this thesis: standardized driving cycles, irrespective of their intended representational focus, whether moderate urban conditions (UDDS), low-speed transit corridors (CBD), mixed urban and suburban profiles (OCTA), or extreme inner-city congestion (MANDC), fail to accurately capture the specific energy demands dictated by Modena's unique and empirically derived driving patterns. The magnitude, and in certain instances even the direction (i.e., overestimation versus the more common underestimation), of these deviations are observed to vary significantly. This variability is dependent not only on the specific standard cycle being compared but also, critically, on the distinct powertrain technology under evaluation. This profound variability inherently underscores the unreliability and potential fallibility of utilizing generic cycles for applications demanding high fidelity and local accuracy, such as detailed techno-economic feasibility studies or environmental impact assessments specific to Modena.

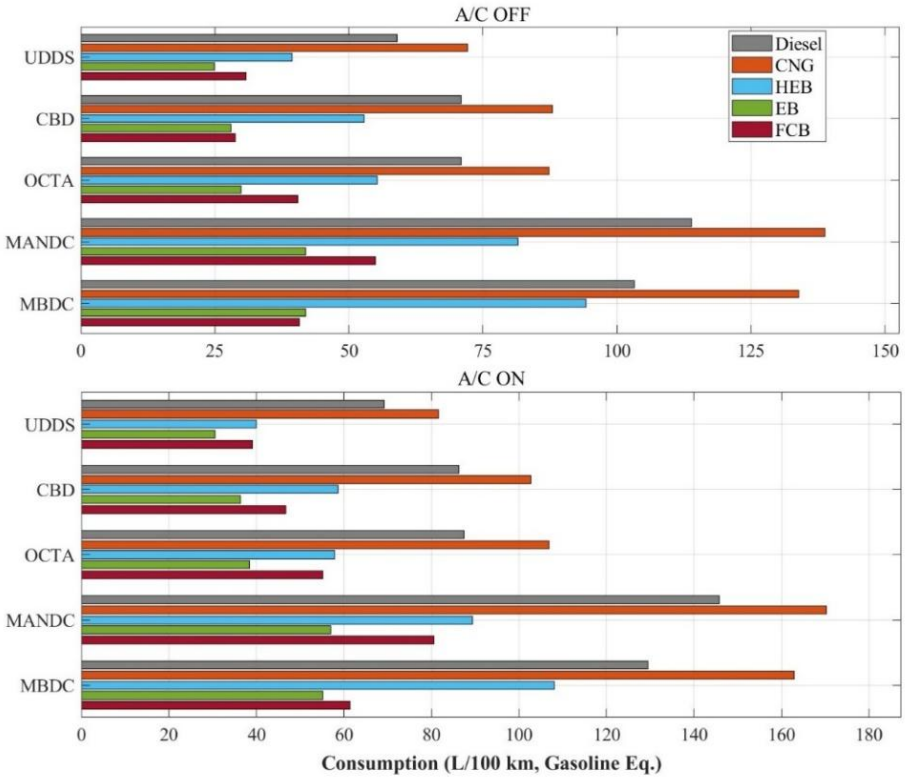

Figure 4.10. Fuel Consumption Data of Different Powertrains on Various Driving Cycles

Analysing the performance under A/C off conditions in meticulous detail, using MBDC as the reference benchmark and referencing the final data in Table 4.5:

- UDDS vs MBDC (A/C Off): The UDDS cycle consistently and significantly predicts far lower fuel consumption compared to the MBDC baseline across every evaluated powertrain technology. The extent of this underestimation is remarkably high, indicating a fundamental mismatch in cycle severity. Specifically, the underestimation ranges from a substantial -24.51% for the FCB (predicting 30.8 L/100km versus MBDC's 40.8 L/100km) to an exceptionally large discrepancy of -58.2% for the HEB (predicting only 39.4 L/100km compared to MBDC's 94.2 L/100km). For the conventional Diesel and CNG buses, the underestimations remain severe at -42.8% and -46.1%, respectively. Similarly, the EB shows a -40.6% deviation. These large negative differences strongly suggest that the moderate acceleration profiles, higher average speeds, and lower idling times characteristic of the UDDS cycle do not adequately represent the intense energy demands imposed by the frequent stops, prolonged idling periods, and specific transient operations inherent in the MBDC. Relying on UDDS data would lead to grossly optimistic projections of fuel economy and operational costs for bus deployment in Modena.
- CBD vs MBDC (A/C Off): The low-speed, highly repetitive CBD-14 cycle also consistently underestimates the MBDC consumption profile, although the magnitude varies across technologies. The smallest underestimation is observed for the FCB at -30.15% (28.5 vs 40.8 L/100km). The underestimation is slightly larger for the EB (-33.17%, 28.0 vs 41.9 L/100km), CNG bus (-34.3%, 88.0 vs 133.9 L/100km) and the EB (-33.2%, 28.0 vs 41.9 L/100km). However, the discrepancies are considerably larger for the HEB (-43.8%, 52.9 vs 94.2 L/100km). While the CBD cycle explicitly focuses on low-speed operation common in central business districts, its highly regular, predictable pattern of acceleration and deceleration, coupled with shorter idling times compared to MBDC, likely explains its failure to capture the full energy penalty associated with Modena's specific driving style, particularly for the advanced powertrain concepts (HEB) whose efficiencies are sensitive to transient patterns.
- OCTA vs MBDC (A/C Off): The OCTA cycle, often considered a relevant benchmark for transit buses due to its inclusion of both urban and arterial road segments, similarly underestimates the energy demands observed on the MBDC. The degree of underestimation is the smallest for the FCB, at -0.74% (40.5 vs 40.8 L/100km). For the

other models, the underestimation is considerably larger: -31.3% for the Diesel bus (70.9 vs 103.2 L/100km), -34.8% for the CNG bus (87.3 vs 133.9 L/100km), -41.3% for the HEB (55.3 vs 94.2 L/100km), and -28.6% for the EB (29.9 vs 41.9 L/100km). These figures clearly demonstrate that even a commonly accepted and relatively diverse transit bus cycle like OCTA provides a significantly optimistic assessment of fuel consumption compared to the operational realities captured by the MBDC, suggesting that its higher-speed segments dilute the impact of severe urban congestion.

- Manhattan (MANDC) vs MBDC (A/C Off): The comparison with the extreme, highly aggressive Manhattan cycle yields the most complex and revealing insights, demonstrating that higher cycle severity does not uniformly lead to higher consumption relative to MBDC. For the conventional Diesel (+10.4%) and CNG (+3.7%) buses, as well as the FCB (+34.8%), the Manhattan cycle predicts *higher* consumption than MBDC. This outcome indicates that the combination of Manhattan's extremely low average speed and its unique acceleration pattern place a greater energy demand on Diesel, CNG, and FCB technologies compared to the MBDC cycle. In stark contrast, the EB shows virtually identical consumption on both cycles (+0.2% difference, 42.0 vs 41.9 L/100km). Most strikingly, the HEB exhibits anomalous behaviour, predicting significantly lower consumption on the Manhattan cycle (81.5 L/100km) compared to MBDC (94.2 L/100km), resulting in a -13.5% difference relative to MBDC. This counterintuitive result strongly suggests a unique, perhaps highly favourable, synergistic interaction between the HEB's specific control strategy and those unique driving dynamics—an advantage clearly not realized to the same extent in the MBDC's specific operational pattern.

The analysis under A/C on conditions further reinforces the inadequacy of standard cycles and highlights the crucial interplay between driving dynamics, auxiliary loads, and powertrain technology:

- UDDS, CBD, OCTA vs MBDC (A/C On): These cycles consistently and significantly underestimate the A/C On consumption observed on MBDC for all models. The magnitude of this underestimation is often even larger than in the A/C Off case, indicating that standard cycles fail to capture both the baseline energy demand and the additional burden imposed by auxiliary systems under real-world local conditions. For instance, OCTA underestimates MBDC A/C On consumption by percentages ranging

from -10.1% for the FCB (55.2 vs 61.4 L/100km) to a very large -46.4% for the HEB (57.9 vs 108.0 L/100km). The underestimations from UDDS and CBD are generally even greater, frequently exceeding 30% and reaching as high as -63.0% for the HEB on UDDS (40.0 vs 108.0 L/100km).

- Manhattan (MANDC) vs MBDC (A/C On): Similar to the A/C Off scenario, the Manhattan cycle predicts higher A/C On consumption than MBDC for Diesel (+12.7%), CNG (+4.5%), and FCB (+31.3%). The EB again shows very similar consumption (+3.4% difference). The distinct behaviour of the HEB persists, with Manhattan predicting considerably lower consumption than MBDC (-17.2% difference, 89.4 vs 108.0 L/100km), which further suggests a cycle-specific efficiency advantage for this hybrid powertrain on the Manhattan cycle, even with the A/C active.
- Technology Ranking Shifts (A/C On): The relative efficiency ranking among technologies remains consistent across all driving cycles when the A/C load is applied. Specifically, the established order of EB (55.1 L/100 km) < FCB (61.4 L/100 km) < HEB (108.0 L/100 km) < Diesel (129.4 L/100 km) < CNG (162.9 L/100 km) observed on MBDC persists in all other cycles. This stability suggests that, despite variations in speed patterns and load conditions across driving cycles, the influence of the A/C system does not alter the overall efficiency hierarchy. Consequently, the electric bus consistently demonstrates the highest energy efficiency, while CNG and diesel technologies remain the least efficient options under comparable operational conditions.

In conclusion, this comprehensive, multi-cycle comparative analysis, rigorously benchmarked against the locally derived MBDC and supported by the detailed quantitative data presented in the final revised Table 4.5 and visualizations in Figure 4.10, unequivocally demonstrates that standardized driving cycles provide widely divergent, and predominantly inaccurate, predictions of fuel consumption for Modena's specific operational context. The deviations identified, ranging from substantial underestimations by moderate cycles (often exceeding 40–50%) to inconsistent results and altered technology rankings when compared to extreme cycles such as MANDC, all relative to the MBDC benchmark, highlight the critical limitations and potential pitfalls of relying solely on generic benchmarks for applications that require local accuracy. The unique performance profiles observed on the MBDC strongly validate its necessity for generating realistic energy assessments, reliable operational cost projections, and strategically informed decision-making regarding the selection and deployment of sustainable

public transport solutions tailored specifically to the infrastructure, traffic patterns, and operational realities of the city of Modena.

Further context for the simulation results presented in Table 4.5 can be gained by comparing them with experimental studies reported in the literature. Notably, the study by Wayne et al. [133] provides directly comparable chassis dynamometer test results for conventional diesel, Liquefied natural gas (LNG), and hybrid electric buses across several standard cycles, including UDDS, CBD, OCTA, and MANDC. Two key trends observed in Wayne et al.'s findings (specifically Figure 24 of their study) align well with the results of the present study. Firstly, Wayne et al. consistently reported lower fuel economy (higher fuel consumption) for the LNG bus compared to the conventional diesel bus across all tested cycles. For example, on the MANDC, the diesel bus achieved approximately 3.9 MPG while the LNG bus reached only 2.9 MPG. This finding directly corresponds with our simulation results in Table 4.5, where the CNG bus consistently exhibits significantly higher gasoline-equivalent fuel consumption than the Diesel bus across all five driving cycles evaluated. Secondly, the results from Wayne et al. generally show an increasing trend in fuel consumption (decreasing MPG) as the cycle severity increases, moving from UDDS to CBD, OCTA, and finally MANDC for diesel, LNG and HEB. This trend is largely mirrored in our simulation results presented in Table 4.5, where consumption for most powertrain types generally increases across the sequence UDDS < CBD ≈ OCTA < MBDC < MANDC, although technology-specific responses (like the HEB on MANDC) introduce nuances. This broad agreement with experimentally derived data from comparable vehicles and cycles lends further credibility to the simulation results and the observed impact of driving cycle characteristics on bus fuel consumption.

4.3. Additional Performance Benchmarking Analyses

4.3.1. Effect of Vehicle Parameters on Fuel Consumption

It is widely recognized that a vehicle's primary physical parameters such as total mass, aerodynamic drag coefficient, and wheel radius play a decisive role in determining its resistance to motion and inertia, which in turn dictate its fuel consumption characteristics. To assess how variations in these three parameters influence the performance of different bus configurations, a detailed sensitivity analysis was performed using the OCTA drive cycle as a reference. All computations were carried out with the A/C system switched off to eliminate the confounding influence of auxiliary energy demands, ensuring that the observed outcomes could be solely attributed to the physical parameters under examination.

In the analysis, each of the three parameters was independently altered by ±10% relative to its baseline value, while the remaining two parameters were kept constant. This methodological approach enabled a clear evaluation of individual parameter sensitivity. Fuel consumption outcomes were expressed in gasoline-equivalent units (L/100 km), with the summarized results and corresponding percentage variations presented in Figure 4.11 and Table 4.6. In Table 4.6, the notation F_{cg} denotes the gasoline-equivalent fuel consumption, while %d signifies the relative change in consumption for each test case. The ±10% modification interval was selected to represent realistic fluctuations in both operational and design conditions. For example, total bus mass may vary substantially due to passenger load differences. Given that the simulations were based on 26 occupants and the bus's maximum seating capacity is 50, the resulting variation in vehicle mass could reach approximately 1,700 kg, supporting the plausibility of the chosen adjustment range [100].

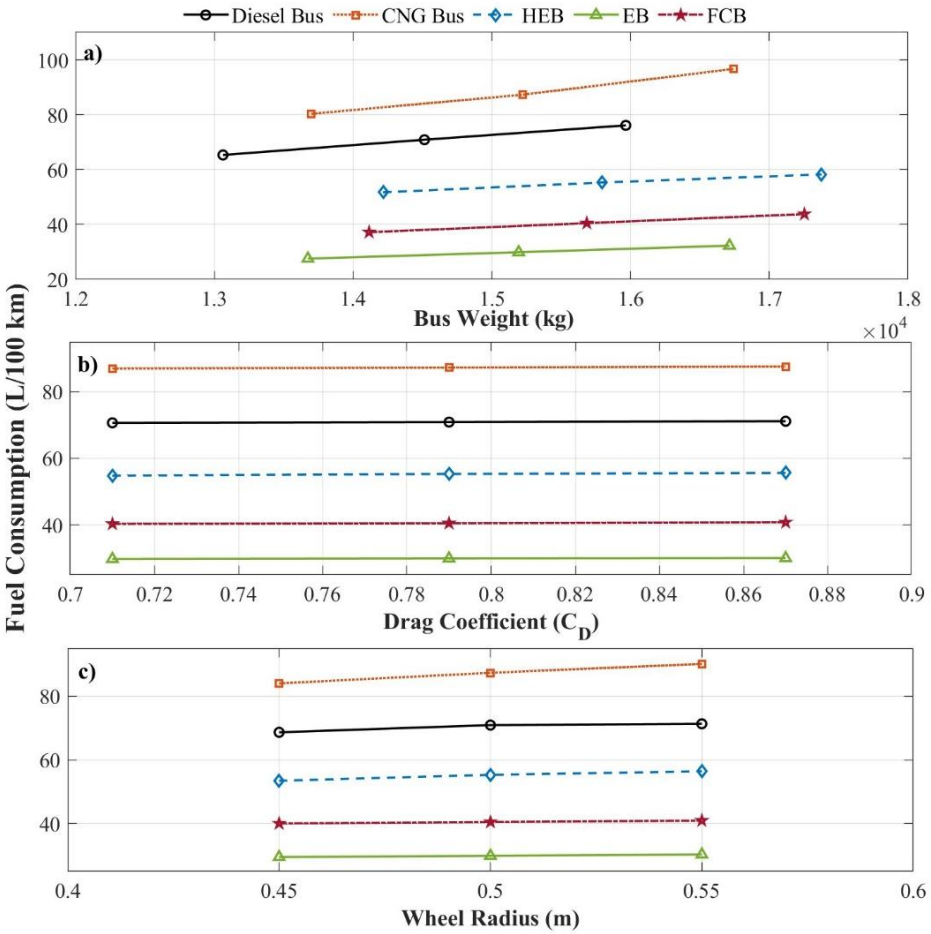

Figure 4.11. Influence of (a) vehicle mass. m_v (C_D = 0.79, r_d = 0.5 m), (b) aerodynamic drag coefficient (m_v = 14,515 kg, r_d = 0.5 m), and (c) wheel radius (C_D = 0.79) on the gasoline-equivalent fuel consumption

Likewise, the adopted C_D values of 0.71, 0.79, and 0.87 were derived from a literature review, which indicates that older bus models with less aerodynamic refinement can reach drag coefficients near 0.93 [134,135], whereas modern streamlined designs often achieve considerably lower values through aerodynamic optimization [136]. The selected wheel radii of 0.45, 0.50, and 0.55 meters also align well with typical dimensions reported for contemporary urban buses [40,137–139].

A comparative interpretation of Figure 4.11 and Table 4.6 demonstrates a distinct hierarchy in the magnitude of parameter influence. Among the parameters analysed, vehicle mass exerted the greatest impact on fuel consumption, while aerodynamic drag had the least. The CNG-powered bus exhibited the highest sensitivity to weight variation: a 10% decrease in mass led to a 7.97% reduction in fuel consumption, whereas a 10% increase caused an approximately 10.79% rise. Conversely, the HEB showed the lowest sensitivity to mass changes; its fuel consumption dropped by 6.45% with a 10% weight reduction and rose by 5.32% with a 10% increase, indicating that its powertrain system is comparatively robust against mass fluctuations.

Table 4.6. Impact of vehicle mass, aerodynamic drag coefficient, and wheel radius on the gasoline-equivalent fuel consumption across various bus configurations

Bus Weight, m_v (kg) (C_D = 0.79, r_d = 0.5 m)														
Diesel Bus			CNG Bus			Hybrid Electric Bus			Electric Bus			Fuel Cell Bus		
m_v	F_{cg}	%d	m_v	F_{cg}	%d	m_v	F_{cg}	%d	m_v	F_{cg}	%d	m_v	F_{cg}	%d
13063	65.34	7.84	13700	80.34	7.97	14217	51.73	6.45	13675	27.57	7.79	14116	37.2	8.14
14515	70.9	-	15223	87.3	-	15797	55.3	-	15194	29.9	-	15685	40.5	-
15966	76.13	7.37	16745	96.7	10.79	17377	58.24	5.32	16713	32.3	8.03	17253	43.8	8.14
Drag coefficient, C_D (-) (m_v = 14515 kg, r_d = 0.5 m)														
-	Diesel Bus			CNG Bus			Hybrid Electric Bus			Electric Bus			Fuel Cell Bus	
C_D	F_{cg}	%d		F_{cg}	%d		F_{cg}	%d		F_{cg}	%d		F_{cg}	%d
0.71	70.68	0.31		87	0.34		54.82	0.87		29.75	0.5		40.32	0.44
0.79	70.9	-		87.3	-		55.3	-		29.9	-		40.5	-
0.87	71.16	0.37		87.58	0.37		55.64	0.61		30	0.33		40.76	0.64
Wheel radius, r_d (m) (C_D = 0.79)														
-	Diesel Bus			CNG Bus			Hybrid Electric Bus			Electric Bus			Fuel Cell Bus	
r_d	F_{cg}	%d		F_{cg}	%d		F_{cg}	%d		F_{cg}	%d		F_{cg}	%d
0.45	68.64	3.19		84.04	3.73		53.45	3.35		29.47	1.44		40.05	1.11
0.5	70.9	-		87.3	-		55.3	-		29.9	-		40.5	-
0.55	71.29	0.55		90.14	3.25		56.38	1.95		30.33	1.44		40.94	1.08

In contrast, variations in aerodynamic drag C_D produced only marginal effects on consumption across all bus types. The HEB responded most noticeably, where a 10% rise in C_D increased

fuel use by 0.61%, and a 10% reduction lowered it by 0.87%. Other models showed even weaker responses: the diesel bus exhibited only a 0.31% decrease under reduced drag, while the electric bus registered a minimal 0.33% increase with higher drag.

Adjustments in wheel radius within the same ±10% range (0.45–0.55 m) had a moderate impact, greater than that of aerodynamic drag but still less pronounced than mass effects. Once again, the CNG bus was the most responsive: enlarging the wheel radius by 10% led to a 3.25% increase in fuel consumption, while reducing it by 10% resulted in a 3.73% decrease. On the other hand, the diesel bus showed the smallest sensitivity to an increased radius (0.55% rise), and the FCB demonstrated the least improvement when the radius was reduced (1.15% decrease).

Overall, the findings clearly demonstrate that increases in any of the three investigated physical parameters result in higher fuel consumption across all examined powertrain types. Nonetheless, it must be emphasized that the quantitative sensitivities reported here are specific to the OCTA drive cycle. The degree of influence exerted by these parameters may vary under different driving conditions characterized by distinct speed and acceleration profiles.

4.3.2. Effect of Road Slope on Fuel Consumption (Modified CBD-14 Cycle)

To assess how road gradient influences vehicle energy demand, fuel consumption estimations were carried out for each bus configuration using a customized version of the CBD-14 driving cycle. In this investigation, simulations were performed under constant slopes of 0%, 2%, and 4%, with separate analyses conducted for both active and inactive air conditioning modes. This approach enabled the isolation of grade resistance effects from auxiliary power influences, thereby clarifying each powertrain's specific response to elevation. Although the conventional CBD-14 cycle does not inherently include elevation profiles, the ADVISOR platform allows such modifications which is a capability that has been widely utilized in previous research to examine vehicular performance under inclined conditions [140]. The summarized outcomes of this analysis, expressed in gasoline-equivalent units, are presented in Table 4.7.

Table 4.7. Road grade effect on the fuel consumption for different powertrains

	0% road grade		**2% road grade**		**4% road grade**	
Bus Type	A/C off	A/C on	A/C off	A/C on	A/C off	A/C on
Diesel Bus	70.9	86.3	94.2	110.3	174.7*	208*
CNG Bus	88	102.7	114.3	134.2	215.3*	241.1*
Hybrid Electric Bus	52.9	58.6	71	73.3	78.7	80.2
Electric Bus	28	36.3	40.5	49.2	54	53.3
FCB	28.5	46.7	47.7	72.1	65.7	79.7

A preliminary evaluation of Table 4.7 indicates a recurring trend: across all grade scenarios and A/C settings, the CNG-powered bus consistently exhibited the highest fuel consumption. However, a more detailed comparison based on the relative change in consumption as the road gradient increased revealed that the HEB showed the smallest proportional rise. This finding highlights the HEB's superior capability to sustain efficiency when operating on sloped roadways.

At the 2% grade, the FCB experienced the steepest rise in fuel consumption when the A/C was turned off, registering an increase of approximately 67%. Under the same slope with the A/C operating, again the FCB displayed the highest relative increase, amounting to 54.4%. Conversely, among all tested models, the CNG bus recorded the lowest percentage rise in consumption at this grade when the A/C was off, while the HEB exhibited the smallest increase when the A/C was on. Despite this variation in sensitivity, the EB maintained the lowest absolute fuel consumption across every grade, underscoring its inherent efficiency advantage even under moderate incline conditions.

The findings obtained for the 4% grade scenario require careful interpretation, particularly for the diesel and CNG buses. At this elevated slope, noticeable discrepancies emerged between the prescribed drive cycle speeds and those achievable by the simulations, indicating potential accuracy limitations under high-load conditions [101]. Nonetheless, even with these constraints, the HEB continued to show the lowest proportional increase in fuel consumption for both A/C operating states. Meanwhile, the diesel, CNG, and FCB models exhibited pronounced rises in absolute consumption, clearly demonstrating the substantial impact of gradient-induced load on these powertrain types.

Overall, the analysis of the fixed 2% and 4% slope conditions reveals that the HEB possesses a comparative advantage in minimizing the rate of increase in fuel consumption associated with road incline. However, the EB consistently outperformed all other models in terms of absolute efficiency, achieving the lowest gasoline-equivalent fuel consumption across every evaluated scenario, thereby confirming its strong energy performance even on inclined terrains.

4.3.3. Gradeability Test Results

Beyond the assessment of fuel consumption under varying operating conditions, gradeability analyses were conducted to evaluate the climbing performance of the five distinct bus powertrain architectures. These simulations determined the maximum continuous slope

(expressed as a percentage) that each bus could successfully ascend at two fixed velocities: 20 km/h, representing low-speed conditions such as starting or manoeuvring on urban gradients, and 40 km/h, corresponding to steady climbing at a moderate speed. Each test was executed under both A/C off and on states, thereby enabling evaluation of the influence of auxiliary energy demand on the vehicle's maximum climbing capability. The complete set of outcomes from these simulations is summarized in Table 4.8.

Table 4.8. Gradeability of Different Powertrains for 20 km/h and 40 km/h Speed

	20 km/h		**40 km/h**	
Vehicle Type	A/C off	A/C on	A/C off	A/C on
Diesel Bus	17.2%	15.8%	7.3%	6.8%
CNG Bus	17%	15.5%	7.1%	6.7%
Hybrid Electric Bus	22.5%	22%	10.3%	10.1%
Electric Bus	14%	14%	9.8%	9.8%
FCB	12.4%	12.2%	6.2%	6.0%

The analysis of Table 4.8 reveals a clear and consistent outcome: the HEB outperformed all other models across every evaluated condition. The superior gradeability exhibited by the HEB underscores the effectiveness of its dual-source powertrain configuration: combining an internal combustion engine with an electric motor. It provides enhanced torque output essential for ascending steep gradients.

At the lower test speed of 20 km/h, the HEB achieved a maximum grade of 22.5% with the A/C system deactivated and a slightly reduced 22% when the A/C was operating. These results substantially exceeded the performance of the conventional buses. The diesel bus reached 17.2% (A/C off) and 15.8% (A/C on), while the CNG Bus achieved 17.0% and 15.5% under the same respective conditions. The electric-based configurations displayed comparatively limited gradeability at this speed; the EB consistently sustained a 14% maximum grade regardless of A/C operation, while the FCB demonstrated the lowest performance—only 12.4% under A/C off and 12.2% when the A/C on. This finding indicates that, in low-speed and high-torque scenarios, the FCB configuration in this study was the least capable. It is also notable that the A/C load had a measurable impact on the Diesel and CNG buses, reducing their gradeability by approximately 1.4–1.5 percentage points, whereas its effect was minor for the HEB (0.5 points) and negligible for the EB and FCB.

At the higher velocity of 40 km/h, a general decline in gradeability was observed across all configurations, consistent with the increased power demand required to counter aerodynamic drag and maintain greater speeds on inclines. Nonetheless, the relative ranking among bus types remained largely unchanged. The HEB once again demonstrated the strongest performance, reaching grades of 10.3% with A/C off and 10.1% with A/C on. The EB followed closely, maintaining a steady gradeability of 9.8% under both conditions. The conventional buses exhibited reduced capabilities at this speed: the diesel bus achieved 7.3% (A/C off) and 6.8% (A/C on), while the CNG Bus managed 7.1% and 6.7%, respectively. The FCB continued to display lower gradeability, achieving 6.2% and 6.0% under A/C off and on modes, respectively. At 40 km/h, the impact of A/C operation was more uniform among the internal combustion engine–based and fuel cell models, lowering their climbing capacity by approximately 0.2–0.5 percentage points. In contrast, the HEB's sensitivity to auxiliary load remained minimal (0.2 points), and the EB's performance remained unaffected.

In summary, the gradeability evaluation clearly emphasizes the dominance of the hybrid electric configuration, particularly under low-speed conditions typical of steep urban routes. The HEB's ability to simultaneously draw power from its combustion engine and electric motor provides the torque advantage necessary for superior climbing performance compared to the other analysed models. Although the EB demonstrated relatively strong performance at 40 km/h, its capability at 20 km/h was noticeably inferior to that of the HEB and conventional buses. The FCB consistently exhibited the lowest gradeability, implying that, within the simulated configuration, it may be less suitable for transit routes characterized by significant elevation changes.

4.4. Green Hydrogen Refuelling Station for Public Transportation

4.4.1. Hydrogen demand and station sizing

Based on the hydrogen consumption results determined in Section 4.2 for the FCB application, together with the daily average ambient temperature distributions documented in Section 3.4.1, the prospective sizing of a hydrogen refuelling station was performed. Within this framework, each bus was assumed to travel 150 km per day, and for different fleet sizes (1, 2, 4, 8 and 16 buses), the corresponding high-pressure tank capacity, low-pressure tank capacity, and compressor power demand of the station were calculated following the methodology described in Section 3.4.3.

Table 4.9 summarises the resulting system sizing parameters for the five scenarios. In this table, N_{bus} denotes the fleet size, $H_{2,yearly}$ represents the yearly hydrogen consumption of the fleet (kg), P_{comp} indicates the required compressor power, and C_{HP} and C_{LP} correspond to the required hydrogen mass storage capacities of the high-pressure and low-pressure buffer tanks (kg of hydrogen), respectively. In this manner, the table provides a direct quantitative link between fleet scale and station hardware configuration, enabling the comparison of capacity requirements across different deployment magnitudes.

Table 4.9. Sizing of the HRS components for Different Daily Range

No	N_{bus}	Daily Range, km	P_{comp}, kW	C_{HP}, kg	C_{LP}, kg	$H_{2,yearly}$
1	1	150	12.4	25.74	5.15	6349.0
2	2	300	24.8	51.48	10.30	12699.9
3	4	600	49.7	102.96	20.59	25407.74
4	8	1200	99.3	205.92	41.18	50839.92
5	16	2400	198.6	411.84	82.37	101707.24

The results illustrate a near-linear growth trend: when the number of buses increases from 1 to 16, the yearly hydrogen demand rises from approximately 6.3 tonnes to slightly above 101 tonnes, and the compressor requirement increases correspondingly from 12.4 kW to almost 200 kW. The same proportional pattern is observed for storage components. The high-pressure buffer, for example, grows from 25.7 kg for a one-bus case to 411.8 kg for the 16-bus configuration, while the low-pressure buffer increases from 5.15 kg to 82.37 kg. This consistency in scaling behaviour confirms that the sizing methodology is internally coherent: the dominant driver of station capacity is simply the cumulative daily range demand imposed by the fleet.

Table 4.10 presents, for each scenario, the annual compressor energy consumption together with the corresponding specific energy demand per unit of hydrogen compressed. In this context, $E_{comp,year}$ denotes the total annual electricity requirement of the compressor system (kWh/year), whereas $E_{comp,year,kg}$ represents the specific energy demand per kilogram of hydrogen dispensed (kWh/kg). The values demonstrate that, although the absolute annual compressor load naturally increases with increasing fleet size, the specific compressor energy requirement per kilogram of hydrogen remains relatively stable across all scenarios. This

indicates that the thermodynamic compression penalty is essentially governed by the operating pressure levels and the daily cycling pattern rather than by the number of buses served.

Table 4.10. Compression Energy for Different Number of Buses

No	N_{bus}	Daily Range, km	$E_{comp,year}$, kWh	$E_{comp,year,kg}$, kWh/kg
1	1	150	38553.1	6.072
2	2	300	76835	6.05
3	4	600	153108.8	6.026
4	8	1200	306445.3	6.028
5	16	2400	613163.5	6.028

Figure 4.12 compares two extreme station configurations (150 km/day and 2400 km/day) by presenting the annual evolution of hydrogen mass stored in both the low-pressure and high-pressure buffers together with the corresponding high-pressure vessel pressure. The traces highlight the expected thermodynamic coupling between stored mass and system pressure. Increases in tank inventory led to a proportional rise in pressure, whereas reductions in stored hydrogen result in a corresponding decrease. This behaviour aligns with the ideal gas formulation $PV = mRT$, since the vessel volumes are fixed and the variations in hydrogen mass directly translate into pressure fluctuations. More importantly, the observed trajectories confirm that the storage system remains within the intended operational boundaries. In all cases, the high-pressure vessel consistently stays above the 35 MPa minimum delivery threshold required to sustain dispenser operation, while the low-pressure inventory remains confined to its prescribed 2–5 bar production envelope. These results demonstrate that the selected tank capacities are sufficient to buffer variations in hydrogen demand under both low and high throughput conditions, and that the sizing methodology scales coherently without violating the pressure constraints imposed by the station architecture.

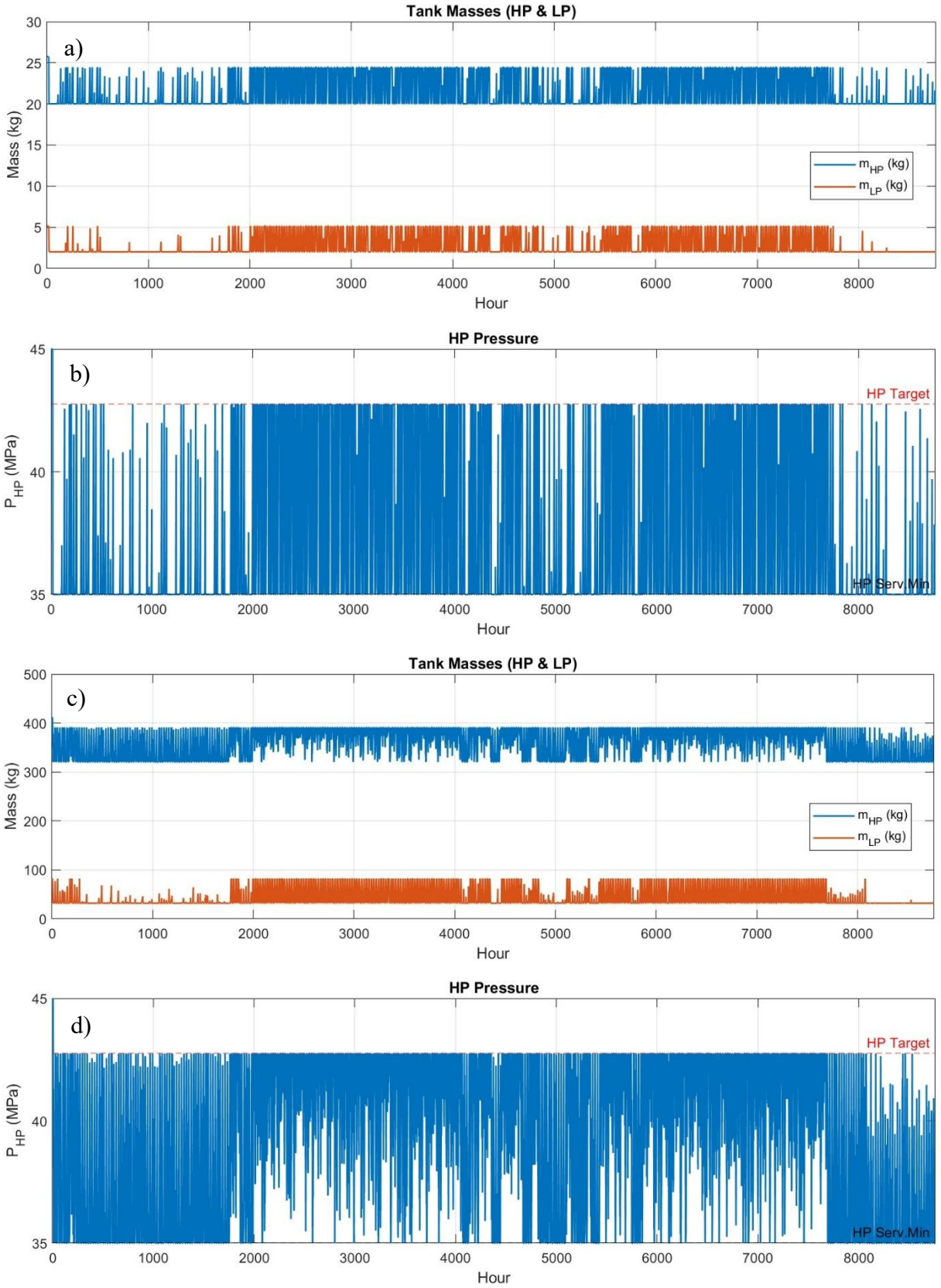

Figure 4.12. Comparison of the Pressure and Mass levels of the HP and LP tanks

4.4.2. Pre-cooling unit energy consumption

The monthly E_{PCU} trajectories shown in Figure 4.13 provide a direct view of how the specific precooling load evolves under different fleet sizes. For the smallest utilisation level (150-km/day equivalent), the monthly values span a broad range, from approximately 0.82 kWh/kg-H_2 in February up to 3.16 kWh/kg-H_2 in August. Increasing the daily range to 300 km reduces both the amplitude and the absolute level of this seasonal swing; the reported values fall into a narrower band of 0.50–2.23 kWh/kg-H_2 over the year. The compression of that envelope continues systematically as the effective fleet size increases. In the 600-km/day case the seasonal band is already constrained to 0.34–1.26 kWh/kg-H_2, in the 1200-km/day case to 0.27–0.77 kWh/kg-H_2, and in the largest utilisation scenario (2400-km/day) to 0.24–0.52 kWh/kg-H_2. This systematic monotonic contraction of the month-to-month variability is consistent with the qualitative expectation that, as the daily mass throughput grows, the precooling duty becomes a relatively smaller perturbation per unit of dispensed hydrogen, and therefore the temperature-driven penalty is diluted. In other words, the EPCU signal converges toward lower and flatter values as the station loading approaches a higher-capacity regime. Overall, the resulting values on a kWh/kg-H_2 basis are of the same order of magnitude as those reported in the literature for comparable precooling duty formulations.

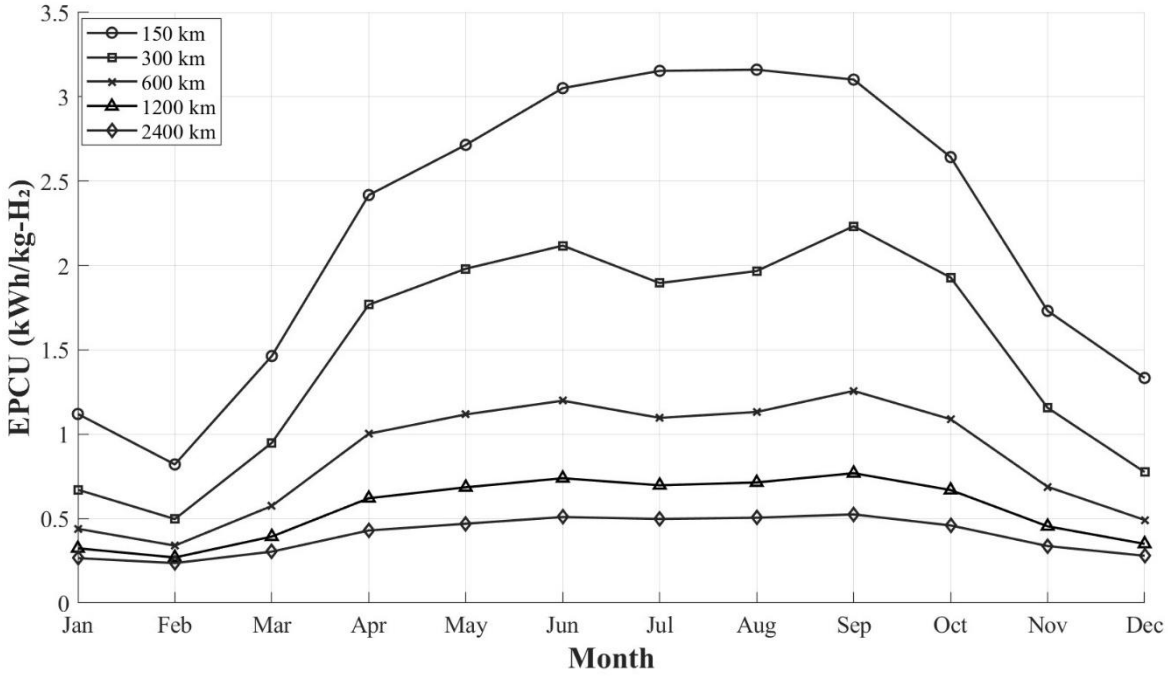

Figure 4.13. Energy Consumption of the EPCU over a Year for Different Daily Range

Table 4.11 summarises the monthly E_{PCU} (kWh/month) associated with the same five demand ranges. The pattern is broadly monotonic in two dimensions: first, across fleet size, and second,

across season. The lowest annual-load case (150 km/day) returns a monthly EPCU demand of 493 kWh in February and 1825 kWh in July; the highest-load case (2400 km/day) spans from 2269 kWh (February) to 4607 kWh (July). In other words, within each column, the minimum occurs in late winter (February) and the maximum in midsummer (July), consistent with the temperature-driven penalty formulation introduced earlier. Likewise, for any given month, the ranking across scenarios is strictly ordered, as EPCU demand increases monotonically with total daily hydrogen throughput, resulting in monthly spreads that rise from approximately 740 to 2800 kWh in January to approximately 1825 to 4600 kWh in July. Finally, the annual aggregates reinforce this same structure: total E_{PCU} increases from 13.6 MWh/year (150 km/day) to 39.6 MWh/year (2400 km/day), with no inversions or irregularities across the intermediate demand levels.

Table 4.11. Energy Consumption of the EPCU unit

	E_{PCU} (kWh) for Daily Range				
Month	**150 km**	**300 km**	**600 km**	**1200 km**	**2400 km**
January	736.73	882.72	1156.17	1703.06	2796.85
February	493.03	597.16	816.55	1294.61	2269.23
March	846.78	1098.12	1330.10	1820.11	2813.60
April	1033.49	1511.27	1714.97	2122.39	2937.22
May	1199.28	1750.05	1974.16	2422.38	3318.82
June	1392.28	1932.64	2187.80	2698.10	3718.72
July	1824.58	2193.62	2538.33	3227.75	4606.59
August	1737.58	2163.07	2488.91	3140.60	4443.97
September	1348.38	1941.20	2185.27	2673.39	3649.64
October	1167.22	1703.91	1924.21	2364.81	3246.00
November	914.50	1221.95	1454.41	1919.34	2849.20
December	871.34	1015.37	1291.50	1847.08	2958.85
Total	13565.19	18011.08	21062.38	27233.63	39608.71

4.4.3. Potential Hydrogen Production from Biomass

The waste treatment installation in Carpi that is examined in this work handles approximately 25564 tons/year of the organic fraction of municipal solid waste and about 11113 tons/year of virgin wood. When a moisture level of 50% is assumed for both material streams, the corresponding hydrogen production potential is calculated to be on the order of 1050 kg/day from the OFMSW-derived biomethane route and around 913.4 kg/day from the virgin wood gasification route. These production levels indicate that the two green hydrogen pathways

investigated here are capable of supplying the full hydrogen requirement associated with the operation of the urban bus fleet of the city.

Moreover, the comparison becomes even more meaningful when these values are contrasted with the actual demand emerging from the transport context. As previously reported in Section 4.4.1, the yearly hydrogen requirement associated with the selected mobility scenario ranges between 6349 and 101707 kg/year, depending on fleet size and average daily vehicle-kilometres. The available resource base at the Carpi facility therefore appears not merely adequate but comfortably sufficient, since the potential range of hydrogen production from OFMSW and virgin wood significantly exceeds the daily requirement envelope documented earlier. This observation suggests that, under the assumed operational and conversion conditions, hydrogen generated exclusively from locally available biogenic waste streams could satisfy the urban mobility energy demand without the need for additional external hydrogen import.

In order to provide a quantitative illustration of how much biomass must be committed to reach a target yearly hydrogen output within this interval, the estimated biogenic feedstock requirements for both conversion routes have also been calculated, and these values are reported in Table 4.12.

Table 4.12. Annual hydrogen production potential from Carpi feedstocks and comparison with fleet demand

Item	Value
Annual OFMSW processed at facility	25564 tons/year
Annual virgin wood processed at facility	11113 tons/year
Hydrogen potential from OFMSW	383250 kg/year
Hydrogen potential from virgin wood	333405 kg/year
Combined annual hydrogen potential	716655 kg/year
Yearly hydrogen demand of bus fleet	6349 – 101707 kg/year
Required OFMSW to meet this demand	423 – 6780 tons/year
Required virgin wood to meet this demand	212 – 3390 tons/year

5. CONCLUSION AND FUTURE WORK

This research aimed to confront two fundamental barriers in advancing sustainable urban bus transport: the limited capacity of conventional driving cycles to capture localized driving characteristics and the lack of a unified approach for evaluating both the technological and infrastructural viability of environmentally friendly transport options, with particular attention to hydrogen-based systems. To overcome these challenges, the study developed an extensive and interconnected methodological framework that integrates detailed driving behaviour at the microscopic level with the broader system design and capacity planning of an autonomous hydrogen refuelling station.

The first phase of this dissertation focused on developing a representative bus driving cycle for the city of Modena, MBDC. To this end, a novel hybrid metaheuristic optimization algorithm MMAS-ABC was proposed and implemented by integrating the MMAS with the ABC algorithm. The hybrid approach demonstrated clear superiority over the conventional MCMC method. Leveraging real-world GPS data collected from the Modena Linea 7 bus route, the MMAS-ABC algorithm generated a high-fidelity driving cycle with an exceptionally low mean error of 0.76%. In contrast, the best cycle produced by the MCMC method yielded an error of 1.16%. This improvement is attributed to the ABC algorithm's ability to intelligently tune key MMAS parameters (α, β, ρ and Q) in accordance with the problem's specific requirements.

A key contribution of the developed MBDC is its quantitative demonstration of the inadequacy of standardized cycles (UDDS, CBD-14, OCTA, and MANDC) under Modena's local operating conditions. Simulation results revealed that widely used cycles such as UDDS, CBD, and OCTA systematically and substantially underestimated energy consumption by up to 58% when compared with the MBDC. This finding confirms the essential need for empirically grounded, location-specific driving cycles like the MBDC to ensure accurate evaluation of local energy demand and operational costs.

In the second phase of the dissertation, five distinct bus powertrain architectures (Diesel, CNG, HEB, EB, and FCB) were modelled using the ADVISOR simulation environment and evaluated under multiple driving cycles, including the MBDC. The key findings of this comparative analysis can be summarized as follows:

- Using the MBDC as the reference, the EB demonstrated the highest energy efficiency, followed by the FCB. Diesel buses, and particularly CNG buses, exhibited the lowest efficiency levels.

- In grade-climbing assessments, the HEB which couples an internal combustion engine with an electric motor delivered the strongest performance, achieving a 22.5% grade at 20 km/h. In contrast, within the simulated configuration, the FCB showed the lowest gradeability.
- On constant inclines (2% and 4%), the EB remained the most energy-efficient option in absolute consumption terms. However, the HEB showed the smallest proportional increase in fuel consumption as the gradient increased, highlighting its robustness for routes with significant elevation changes.
- Sensitivity analyses revealed that vehicle mass exerted the most dominant influence on fuel consumption across all powertrains, while the aerodynamic drag coefficient had the weakest effect.

The third and final phase of the study assessed the feasibility of establishing a localized green hydrogen infrastructure in Modena by utilizing the FCB energy demand profiles derived from MBDC simulations. This phase served as a critical bridge between vehicle-level performance and infrastructure-level design. The FCB consumption range (9.5–14.3 kg/100 km) was combined with local climate data obtained from the PVGIS, incorporating heating loads (<10°C) and cooling loads (>26°C) to generate a realistic daily hydrogen demand profile. HRS sizing was conducted for fleet sizes ranging from 1 to 16 buses, revealing that a 16-bus fleet would require approximately 101.7 tons of hydrogen per year, a compressor capacity of about 200 kW, and roughly 412 kg of HP on-site storage.

The most significant outcome of the infrastructure analysis concerns the potential for locally produced renewable hydrogen. Two biomass streams from the waste treatment facility in Carpi. namely the OFMSW and woody residues were examined. The results indicate that the potential annual green hydrogen production from these local sources (approximately 716655 kg/year) substantially exceeds the maximum annual demand of a 16-bus fuel cell fleet (around 101707 kg/year). This finding provides strong evidence that a self-sufficient biohydrogen supply chain, based entirely on local waste resources and without reliance on external hydrogen imports, is technically feasible for supporting Modena's urban bus fleet.

In summary, this dissertation presents a holistic methodological framework that successfully integrates real-world driving-cycle development, comparative powertrain analysis, and renewable-resource-based infrastructure design. The proposed MBDC accurately reflects the true energy requirements of bus operations in Modena, while the infrastructure analysis

demonstrates that these demands can be sustainably met using locally available biomass streams. Together, these contributions offer a scientifically grounded and robust foundation for Modena, and comparable urban contexts to plan and implement sustainable public transportation strategies.

The integrated methodology and findings presented in this dissertation provide a solid foundation for future research in sustainable urban transportation. Several promising directions for further investigation are outlined below:

- This study primarily focused on technical feasibility. A natural extension would involve a comprehensive techno-economic assessment of the entire proposed system including alternative powertrains modelled with the MBDC and locally produced biohydrogen. Such an analysis should evaluate the economic competitiveness of different bus technologies and HRS configurations using metrics such as TCO and LCOH.
- The MBDC was generated using data from a single representative bus route in Modena (Linea 7). Future studies could incorporate data from additional routes with varying traffic densities, topographies, and stop frequencies to construct a more extensive city-wide driving-cycle database.
- While this thesis conceptually assessed hydrogen production potential from OFMSW and woody residues at the Carpi facility, future work could conduct detailed process simulations (e.g., in Aspen Plus) tailored to the specific characteristics of these feedstocks for pathways such as anaerobic digestion or steam gasification. Experimental validation would further refine conversion efficiencies and product purity estimations.
- Although the hybrid MMAS-ABC algorithm achieved high accuracy, the ABC-based parameter-tuning layer required a substantial computational effort of approximately nine hours. Future algorithmic research may explore parallel computing techniques or more efficient optimization strategies to accelerate this metaheuristic tuning process.
- The analysis employed ADVISOR, a robust yet quasi-static simulation environment. Future modelling efforts may benefit from advanced dynamic simulation platforms such as MATLAB/Simulink or AVL CRUISE to examine energy-management and thermal-control strategies in greater detail, particularly for HEB and FCB powertrains.

6. REFERENCES

[1] IEA – International Energy Agency. Global Energy Review 2025. Paris: 2025.

[2] Cui Y, Zou F, Xu H, Chen Z, Gong K. A novel optimization-based method to develop representative driving cycle in various driving conditions. Energy 2022;247:123455. https://doi.org/10.1016/j.energy.2022.123455.

[3] Energy system - IEA n.d. https://www.iea.org/energy-system/transport (accessed March 1, 2025).

[4] Aminudin MA, Kamarudin SK, Lim BH, Majilan EH, Masdar MS, Shaari N. An overview: Current progress on hydrogen fuel cell vehicles. Int J Hydrogen Energy 2023;48:4371–88. https://doi.org/10.1016/j.ijhydene.2022.10.156.

[5] Kaya AF, Pedrazzi S, Muscio A. Numerical Modeling and Simulation of a Small-Scale Locomotive Powered by Solid Oxide Fuel Cells. J Phys Conf Ser 2023;2648:0–12. https://doi.org/10.1088/1742-6596/2648/1/012055.

[6] Perera F. Pollution from fossil-fuel combustion is the leading environmental threat to global pediatric health and equity: Solutions exist. Int J Environ Res Public Health 2018;15. https://doi.org/10.3390/ijerph15010016.

[7] De Wolf D, Smeers Y. Comparison of Battery Electric Vehicles and Fuel Cell Vehicles. World Electr Veh J 2023;14:1–13. https://doi.org/10.3390/wevj14090262.

[8] Xia X, Li P. A review of the life cycle assessment of electric vehicles: Considering the influence of batteries. Sci Total Environ 2022;814. https://doi.org/10.1016/j.scitotenv.2021.152870.

[9] Fayyazbakhsh A, Bell ML, Zhu X, Mei X, Koutný M, Hajinajaf N, et al. Engine emissions with air pollutants and greenhouse gases and their control technologies. J Clean Prod 2022;376:134260. https://doi.org/10.1016/j.jclepro.2022.134260.

[10] Gerutu GB, Greyson KA, Chombo PV. Compressed Natural Gas as an Alternative Vehicular Fuel in Tanzania: Implementation, Barriers, and Prospects. Methane 2023;2:66–85. https://doi.org/10.3390/methane2010006.

[11] Ehsani M, Singh KV, Bansal HO, Mehrjardi RT. State of the Art and Trends in Electric and Hybrid Electric Vehicles. Proc IEEE 2021;109:967–84. https://doi.org/10.1109/JPROC.2021.3072788.

[12] Mekhilef S, Saidur R, Safari A. Comparative study of different fuel cell technologies. Renew Sustain Energy Rev 2012;16:981–9. https://doi.org/10.1016/j.rser.2011.09.020.

[13] The Technology Collaboration Programme on Advanced Fuel Cells (AFC TCP). Annual Report 2024. 2024.

[14] Yiğit BH, Karamangil Mİ. Selection powertrain for 25 m bi-articulated series hybrid, electric or fuel cell vehicle operating on Istanbul Bus Rapid Transit Line. Eng Sci Technol an Int J 2024;54. https://doi.org/10.1016/j.jestch.2024.101719.

[15] Szilassy PÁ, Földes D. Compliance indicator determination method to match electric buses with bus lines. Heliyon 2024;10. https://doi.org/10.1016/j.heliyon.2024.e38321.

[16] Guo J, Jiang Y, Yu Y, Liu W. A novel energy consumption prediction model with combination of road information and driving style of BEVs. Sustain Energy Technol

Assessments 2020;42:100826. https://doi.org/10.1016/j.seta.2020.100826.

[17] Hai T, Dhahad HA, Fadhil Jasim K, Sharma K, Zhou J, Fouad H, et al. Deep learning-based prediction of lithium-ion batteries state of charge for electric vehicles in standard driving cycle. Sustain Energy Technol Assessments 2023;60:103461. https://doi.org/10.1016/j.seta.2023.103461.

[18] Gurusamy A, Ashok B, Mason B. Prediction of Electric Vehicle Driving Range and Performance Characteristics: A Review on Analytical Modeling Strategies With Its Influential Factors and Improvisation Techniques. IEEE Access 2023;11:131521–48. https://doi.org/10.1109/ACCESS.2023.3334620.

[19] Tong HY, Ng K. Development of bus driving cycles using a cost effective data collection approach. Sustain Cities Soc 2021;69:102854. https://doi.org/https://doi.org/10.1016/j.scs.2021.102854.

[20] Kancharla SR, Ramadurai G. Incorporating driving cycle based fuel consumption estimation in green vehicle routing problems. Sustain Cities Soc 2018;40:214–21. https://doi.org/10.1016/j.scs.2018.04.016.

[21] Comert SE, Yazgan HR. A new approach based on hybrid ant colony optimization-artificial bee colony algorithm for multi-objective electric vehicle routing problems. Eng Appl Artif Intell 2023;123:106375. https://doi.org/10.1016/j.engappai.2023.106375.

[22] Kefayat M, Lashkar Ara A, Nabavi Niaki SA. A hybrid of ant colony optimization and artificial bee colony algorithm for probabilistic optimal placement and sizing of distributed energy resources. Energy Convers Manag 2015;92:149–61. https://doi.org/10.1016/j.enconman.2014.12.037.

[23] Younes M, Maamar M. Improvement of the ACO meta-heuristic by using the method Artificial Bees Colony (ABC). PRZEGLĄD ELEKTROTECHNICZNY (Electrical Rev 2012;88:174–8.

[24] Keskin F, Yıldız M, Arslannur B. A Data-Driven Framework for Driving Cycle Generation and Analysis. Transp Res Rec 2025;2679. https://doi.org/10.1177/03611981241260700.

[25] Bishop JDK, Axon CJ. Using natural driving experiments and Markov chains to develop realistic driving cycles. Transp Res Part D Transp Environ 2024;137:104507. https://doi.org/10.1016/j.trd.2024.104507.

[26] Arun NH, Mahesh S, Ramadurai G, Shiva Nagendra SM. Development of driving cycles for passenger cars and motorcycles in Chennai, India. Sustain Cities Soc 2017;32:508–12. https://doi.org/10.1016/j.scs.2017.05.001.

[27] Gurusamy A, Ashok B. Establishment of electric two-wheeler driving cycle for energy economy and life cycle assessment under Indian Tier-2 city driving environments. Sustain Energy Technol Assessments 2024;66:103826. https://doi.org/10.1016/j.seta.2024.103826.

[28] Mafi S, Kakaee A, Mashadi B, Moosavian A, Abdolmaleki S, Rezaei M. Developing local driving cycle for accurate vehicular CO2 monitoring: A case study of Tehran. J Clean Prod 2022;336:130176. https://doi.org/10.1016/j.jclepro.2021.130176.

[29] Tong HY. Development of a driving cycle for a supercapacitor electric bus route in Hong Kong. Sustain Cities Soc 2019;48:101588. https://doi.org/10.1016/j.scs.2019.101588.

[30] Hull C, Collett KA, McCulloch MD. Developing a representative driving cycle for paratransit that reflects measured data transients: Case study in Stellenbosch, South Africa. Transp Res Part A Policy Pract 2024;181:103987. https://doi.org/10.1016/j.tra.2024.103987.

[31] Shen P, Zhao Z, Li J, Zhan X. Development of a typical driving cycle for an intra-city hybrid electric bus with a fixed route. Transp Res Part D Transp Environ 2018;59:346–60. https://doi.org/10.1016/j.trd.2018.01.032.

[32] Pandey PK, Arora H, Kumar BA. Development of Driving Cycles for Electric Buses in Patna, India. 2023 8th Int Conf Model Technol Intell Transp Syst MT-ITS 2023 2023. https://doi.org/10.1109/MT-ITS56129.2023.10241532.

[33] Kaymaz H, Korkmaz H, Erdal H. Development of a driving cycle for Istanbul bus rapid transit based on real-world data using stratified sampling method. Transp Res Part D Transp Environ 2019;75:123–35. https://doi.org/10.1016/j.trd.2019.08.023.

[34] Nguyen YLT, Nghiem TD, Le AT, Bui ND. Development of the typical driving cycle for buses in Hanoi, Vietnam. J Air Waste Manag Assoc 2019;69:423–37. https://doi.org/10.1080/10962247.2018.1543736.

[35] Kivekas K, Vepsalainen J, Tammi K. Stochastic Driving Cycle Synthesis for Analyzing the Energy Consumption of a Battery Electric Bus. IEEE Access 2018;6:55586–98. https://doi.org/10.1109/ACCESS.2018.2871574.

[36] Zhao L, Li K, Zhao W, Ke HC, Wang Z. A Sticky Sampling and Markov State Transition Matrix Based Driving Cycle Construction Method for EV. Energies 2022;15:1–19. https://doi.org/10.3390/en15031057.

[37] Durkin K, Khanafer A, Liseau P, Stjernström-Eriksson A, Svahn A, Tobiasson L, et al. Hydrogen-Powered Vehicles: Comparing the Powertrain Efficiency and Sustainability of Fuel Cell versus Internal Combustion Engine Cars. Energies 2024;17. https://doi.org/10.3390/en17051085.

[38] Gautam PK, Arya A, Kumar S, Mitra U, Mehroliya S, Gupta S. Modelling and Simulating Performance of Hybrid Electric Vehicle Using Advisor 2.0. IEEE 4th Int Conf Comput Power Commun Technol GUCON 2021:1–6. https://doi.org/10.1109/GUCON50781.2021.9573552.

[39] Dogdu MF, Reyhancan IA. The comparison of gasoline powered vehicle and serial hybrid vehicle on emissions. Heliyon 2024;10:e28532. https://doi.org/10.1016/j.heliyon.2024.e28532.

[40] Diaz J, Pérez B, Fernández FJ. Energy Assessment of Alternative City Bus Lines: A Case Study in Gijón, Spain. Sustain 2024;16. https://doi.org/10.3390/su16104101.

[41] Keegan G, Nelendran P, Oluwafemi O. Modeling and Simulation of Hybrid Electric Vehicles for Sustainable Transportation: Insights into Fuel Savings and Emissions Reduction. Energies 2024;17. https://doi.org/10.3390/en17205225.

[42] Molina S, Novella R, Pla B, Lopez-Juarez M. Optimization and sizing of a fuel cell range extender vehicle for passenger car applications in driving cycle conditions. Appl Energy 2021;285. https://doi.org/10.1016/j.apenergy.2021.116469.

[43] Kim H, Hartmann N, Zeller M, Luise R, Soylu T. Comparative tco analysis of battery electric and hydrogen fuel cell buses for public transport system in small to midsize

cities. Energies 2021;14. https://doi.org/10.3390/en14144384.

[44] Luu LQ, Riva Sanseverino E, Cellura M, Nguyen HN, Nguyen TM, Nguyen HA. Comparative life cycle impact assessment of electric and conventional bus in Vietnam. Sustain Energy Technol Assessments 2022;54:102873. https://doi.org/10.1016/j.seta.2022.102873.

[45] Muñoz P, Franceschini EA, Levitan D, Rodriguez CR, Humana T, Correa Perelmuter G. Comparative analysis of cost, emissions and fuel consumption of diesel, natural gas, electric and hydrogen urban buses. Energy Convers Manag 2022;257. https://doi.org/10.1016/j.enconman.2022.115412.

[46] Shahariar GMH, Bodisco TA, Zare A, Sajjad M, Jahirul MI, Chu Van T, et al. Impact of driving style and traffic condition on emissions and fuel consumption during real-world transient operation. Fuel 2022;319:123874. https://doi.org/10.1016/j.fuel.2022.123874.

[47] Ahmadi P, Raeesi M, Changizian S, Teimouri A, Khoshnevisan A. Lifecycle assessment of diesel, diesel-electric and hydrogen fuel cell transit buses with fuel cell degradation and battery aging using machine learning techniques. Energy 2022;259. https://doi.org/10.1016/j.energy.2022.125003.

[48] de Almeida SCA, Kruczan R. Effects of drivetrain hybridization on fuel economy, performance and costs of a fuel cell hybrid electric vehicle. Int J Hydrogen Energy 2021;46:39404–14. https://doi.org/10.1016/j.ijhydene.2021.09.144.

[49] Jiang B, Yang D, Yu H, Wang J, He C, Li J, et al. Impact of Road Gradient on Fuel Consumption of Light-Duty Diesel Vehicles. Atmosphere (Basel) 2025;16. https://doi.org/10.3390/atmos16020143.

[50] Posada-Henao JJ, Sarmiento-Ordosgoitia I, Correa-Espinal AA. Effects of Road Slope and Vehicle Weight on Truck Fuel Consumption. Sustain 2023;15:1–19. https://doi.org/10.3390/su15010724.

[51] Venkata KoteswaraRao K, Naga Srinivasulu G, Ramesh Rahul J, Velisala V. Optimal component sizing and performance of Fuel Cell – Battery powered vehicle over world harmonized and new european driving cycles. Energy Convers Manag 2024;300:117992. https://doi.org/10.1016/j.enconman.2023.117992.

[52] Navas-Anguita Z, García-Gusano D, Dufour J, Iribarren D. Prospective techno-economic and environmental assessment of a national hydrogen production mix for road transport. Appl Energy 2020;259:114121. https://doi.org/10.1016/j.apenergy.2019.114121.

[53] Ayodele TR, Mosetlhe TC, Yusuff AA, Ntombela M. Optimal design of wind-powered hydrogen refuelling station for some selected cities of South Africa. Int J Hydrogen Energy 2021;46:24919–30. https://doi.org/10.1016/j.ijhydene.2021.05.059.

[54] Chrysochoidis-Antsos N, Escudé MR, van Wijk AJM. Technical potential of on-site wind powered hydrogen producing refuelling stations in the Netherlands. Int J Hydrogen Energy 2020;45:25096–108. https://doi.org/10.1016/j.ijhydene.2020.06.125.

[55] Guerra CF, Reyes-Bozo L, Vyhmeister E, Salazar JL, Caparrós MJ, Clemente-Jul C. Sustainability of hydrogen refuelling stations for trains using electrolysers. Int J Hydrogen Energy 2021;46:13748–59. https://doi.org/10.1016/j.ijhydene.2020.10.044.

[56] Bahou S. Techno-economic assessment of a hydrogen refuelling station powered by an

on-grid photovoltaic solar system: A case study in Morocco. Int J Hydrogen Energy 2023;48:23363–72. https://doi.org/10.1016/j.ijhydene.2023.03.220.

[57] Gökçek M, Paltrinieri N, Liu Y, Badia E, Dokuz AŞ, Erdoğmuş A, et al. Optimum sizing of hybrid renewable power systems for on-site hydrogen refuelling stations: Case studies from Türkiye and Spain. Int J Hydrogen Energy 2024;59:715–29. https://doi.org/10.1016/j.ijhydene.2024.02.068.

[58] Caponi R, Bocci E, Del Zotto L. On-site hydrogen refuelling station techno-economic model for a fleet of fuel cell buses. Int J Hydrogen Energy 2024;71:691–700. https://doi.org/10.1016/j.ijhydene.2024.05.216.

[59] Bartolucci L, Cordiner S, Mulone V, Tatangelo C, Antonelli M, Romagnuolo S. Multi-hub hydrogen refueling station with on-site and centralized production. Int J Hydrogen Energy 2023;48:20861–74. https://doi.org/10.1016/j.ijhydene.2023.01.094.

[60] Rosa L, Mazzotti M. Potential for hydrogen production from sustainable biomass with carbon capture and storage. Renew Sustain Energy Rev 2022;157:112123. https://doi.org/10.1016/j.rser.2022.112123.

[61] Cormos CC. Green hydrogen production from decarbonized biomass gasification: An integrated techno-economic and environmental analysis. Energy 2023;270:126926. https://doi.org/10.1016/j.energy.2023.126926.

[62] Andrea MF, Sara RH, Luca DZ, Giovanni SS, Enrico B. Techno-economic analysis of in-situ production by electrolysis, biomass gasification and delivery systems for Hydrogen Refuelling Stations: Rome case study. Energy Procedia 2018;148:82–9. https://doi.org/10.1016/j.egypro.2018.08.033.

[63] Martins AH, Rouboa A, Monteiro E. On the green hydrogen production through gasification processes: A techno-economic approach. J Clean Prod 2023;383. https://doi.org/10.1016/j.jclepro.2022.135476.

[64] Tang W, Zhang L, Qiu T, Tan H, Wang Y, Liu W, et al. Efficient Conversion of Biomass to Formic Acid Coupled with Low Energy Consumption Hydrogen Production from Water Electrolysis. Angew Chemie - Int Ed 2023;62:1–8. https://doi.org/10.1002/anie.202305843.

[65] Huzayyin OA, Salem H, Hassan MA. A representative urban driving cycle for passenger vehicles to estimate fuel consumption and emission rates under real-world driving conditions. Urban Clim 2021;36:100810. https://doi.org/10.1016/j.uclim.2021.100810.

[66] Società Emiliana Trasporti Autofiloviari. Mappa del trasporto pubblico locale di Carpi. n.d.

[67] Sadeghian P, Håkansson J, Zhao X. Review and evaluation of methods in transport mode detection based on GPS tracking data. J Traffic Transp Eng (English Ed 2021;8:467–82. https://doi.org/10.1016/j.jtte.2021.04.004.

[68] Tong HY, Ng KW. A bottom-up clustering approach to identify bus driving patterns and to develop bus driving cycles for Hong Kong. Environ Sci Pollut Res 2021;28:14343–57. https://doi.org/10.1007/s11356-020-11554-w.

[69] Qin X, Yu K, Li H, Dai F, Liu H, Yang H, et al. Development of a one-day driving cycle for electric ride-hailing vehicles. Transp Res Part D Transp Environ 2020;89:102597. https://doi.org/10.1016/j.trd.2020.102597.

[70] Duran A, Earleywine M. GPS data filtration method for drive cycle analysis applications. SAE Tech Pap 2012. https://doi.org/10.4271/2012-01-0743.

[71] Shi S, Lin N, Zhang Y, Cheng J, Huang C, Liu L, et al. Research on Markov property analysis of driving cycles and its application. Transp Res Part D Transp Environ 2016;47:171–81. https://doi.org/10.1016/j.trd.2016.05.013.

[72] Walsh B. Markov Chain Monte Carlo and Gibbs Sampling. Lect. Notes EEB 581, 2004.

[73] Li Y, Peng J, He H, Xie S. The Study on Multi-scale Prediction of Future Driving Cycle Based on Markov Chain. Energy Procedia 2017;105:3219–24. https://doi.org/10.1016/j.egypro.2017.03.709.

[74] Dorigo M, Birattari M, Stützle T. Ant Colony Optimization Artificial Ants as a Computational Intelligence Technique. IEEE Comput Intell Mag 2006. https://doi.org/10.4249/scholarpedia.1461.

[75] Deif DS, Gadallah Y. An Ant Colony Optimization Approach for the Deployment of Reliable Wireless Sensor Networks. IEEE Access 2017;5:10744–56. https://doi.org/10.1109/ACCESS.2017.2711484.

[76] Stützle T, Hoos HH. MAX-MIN Ant System. Futur Gener Comput Syst 2000;16:889–914. https://doi.org/10.1016/S0167-739X(00)00043-1.

[77] Miao C, Chen G, Yan C, Wu Y. Path planning optimization of indoor mobile robot based on adaptive ant colony algorithm. Comput Ind Eng 2021;156:107230. https://doi.org/10.1016/j.cie.2021.107230.

[78] Tawfeek MA, El-Sisi A, Keshk AE, Torkey FA. Cloud task scheduling based on ant colony optimization. Proc - 2013 8th Int Conf Comput Eng Syst ICCES 2013 2013:64–9. https://doi.org/10.1109/ICCES.2013.6707172.

[79] Dorigo M, Maniezzo V, Colorni A. Ant system: Optimization by a colony of cooperating agents. IEEE Trans Syst Man, Cybern Part B Cybern 1996;26:29–41. https://doi.org/10.1109/3477.484436.

[80] Duan H bin, Zhang X yin, Wu J, Ma G jun. Max-Min Adaptive Ant Colony Optimization Approach to Multi-UAVs Coordinated Trajectory Replanning in Dynamic and Uncertain Environments. J Bionic Eng 2009;6:161–73. https://doi.org/10.1016/S1672-6529(08)60113-4.

[81] Karaboga D, Basturk B. A powerful and efficient algorithm for numerical function optimization: Artificial bee colony (ABC) algorithm. J Glob Optim 2007;39:459–71. https://doi.org/10.1007/s10898-007-9149-x.

[82] Karaboga D, Gorkemli B, Ozturk C, Karaboga N. A comprehensive survey: Artificial bee colony (ABC) algorithm and applications. Artif Intell Rev 2014;42:21–57. https://doi.org/10.1007/s10462-012-9328-0.

[83] Zhou X, Zhang X, Gao W, Wang H, Ma Y. Adaptive multi-population artificial bee colony algorithm based on fitness landscape analysis. Appl Soft Comput 2024;164:111952. https://doi.org/10.1016/j.asoc.2024.111952.

[84] Galgamuwa U, Perera L, Bandara S. Development of a driving cycle for Colombo, Sri Lanka: an economical approach for developing countries. J Adv Transp 2016;50:1520–30. https://doi.org/10.1002/atr.1414.

[85] Serway RA, Jewett JW. Physics for scientists and engineers with Modern Physics. 9th ed. Cengage Learning; 2018.

[86] Golebiewski W, Prajwowski K, Danilecki K, Lisowski M, Abramek KF. Reducing the Fuel Consumption of an Hybrid Electric Vehicle with the Use of Model Predictive Control-Case Study. IEEE Trans Veh Technol 2023;72:11458–68. https://doi.org/10.1109/TVT.2023.3266829.

[87] Yang J, Zhu GG. Model predictive control of a power split hybrid powertrain. Proc Am Control Conf 2016;2016-July:617–22. https://doi.org/10.1109/ACC.2016.7524982.

[88] Prajwowski K, Golebiewski W, Lisowski M, Abramek KF, Galdynski D. Modeling of working machines synergy in the process of the hybrid electric vehicle acceleration. Energies 2020;13. https://doi.org/10.3390/en13215818.

[89] Wei X, Rizzoni G. Objective metrics of fuel economy, performance and driveability - A review. SAE Tech Pap 2004;2004-01–13. https://doi.org/10.4271/2004-01-1338.

[90] Kumar A, Thakura PR. ADVISOR-Based Performance Analysis of a Hybrid Electric Vehicle and Comparison with a Conventional Vehicle. IETE J Res 2020. https://doi.org/10.1080/03772063.2020.1838344.

[91] Ribbens W. Understanding automotive electronics: an engineering perspective. 8th ed. Butterworth-Heinemann, Elsevier Inc; 2017.

[92] KoteswaraRao.K V, Naga Srinivasulu G. Modeling, downsizing, and performance comparison of a fuel cell hybrid mid-size car with FCEV for urban and hill road driving cycles. Int J Green Energy 2019;16:115–24. https://doi.org/10.1080/15435075.2018.1549996.

[93] Turkmen AC, Solmaz S, Celik C. Analysis of fuel cell vehicles with advisor software. Renew Sustain Energy Rev 2017;70:1066–71. https://doi.org/10.1016/j.rser.2016.12.011.

[94] Zhang G, Chen W, Li Q. Modeling, optimization and control of a FC/battery hybrid locomotive based on ADVISOR. Int J Hydrogen Energy 2017;42:18568–83. https://doi.org/10.1016/j.ijhydene.2017.04.172.

[95] Harvey CA. Gasoline-equivalent fuel economy determination for alternate automotive fuels. SAE Tech Pap 1982;820794. https://doi.org/10.4271/820794.

[96] Nath DS, Pujari PC, Jain A, Rastogi V. Drag reduction by application of aerodynamic devices in a race car. Adv Aerodyn 2021;3. https://doi.org/10.1186/s42774-020-00054-7.

[97] Johnson VH. Battery performance models in ADVISOR. J Power Sources 2002;110:321–9. https://doi.org/10.1016/S0378-7753(02)00194-5.

[98] Wipke K, Markel T, Haraldsson K, Kelly K, Vlahinos A. Fuel Cell Vehicle Systems Analysis. Hydrog Fuel Cells, Infrastruct Technol FY 2003 Prog Rep 2003:1–5.

[99] Katragadda S, Bata R, Wang WG, Gautam M, Clark N, Lyons D, et al. A correlation study between two heavy-duty vehicle chassis dynamometer emissions testing facilities. SAE Tech Pap 1993. https://doi.org/10.4271/931788.

[100] Michael Patrick O, Keith V. An Analysis of Hybrid Electric Propulsion Systems for Transit Buses. Natl Renew Energy Lab 2002;Tech. Rep.

[101] WI H, PARK J. Analyzing uncertainty in evaluation of vehicle fuel economy using FTP-75. Int J Automot Technol 2013;14:471–7. https://doi.org/10.1007/s12239-013-0051-x.

[102] Hirata N, Mizutani N, Matsui H, Yano K, Takahashi T. Fuel consumption in a driving test cycle by robotic driver considering system dynamics. Proc - IEEE Int Conf Robot Autom 2015:3374–9. https://doi.org/10.1109/ICRA.2015.7139665.

[103] Environmental Protection Agency. CFR-2011- title40-vol18-part86.115-78 EPA Urban Dynamometer Driving Schedule. 2011.

[104] Michael Z, John K, Michael F. Heat Tolerant NiMH Batteries for Stationary Power. Ovonic Battery Company, Rochester Hills, MI USA: 2010.

[105] Markel T, Brooker A, Hendricks T, Johnson V, Kelly K, Kramer B, et al. ADVISOR: A systems analysis tool for advanced vehicle modeling. J Power Sources 2002;110:255–66. https://doi.org/10.1016/S0378-7753(02)00189-1.

[106] Anbarasu A, Dinh TQ, Sengupta S. Novel enhancement of energy management in fuel cell hybrid electric vehicle by an advanced dynamic model predictive control. Energy Convers Manag 2022;267:115883. https://doi.org/10.1016/j.enconman.2022.115883.

[107] Reithuber P, Weller K, Schutting E, Eichlseder H. Energy and hydrogen consumption evaluation of a fuel cell city bus based on roller chassis dynamometer measurements. Int J Hydrogen Energy 2025;97:1227–40. https://doi.org/10.1016/j.ijhydene.2024.11.460.

[108] Cigarini F, Schminkel P, Sonnekalb M, Best P, Göhlich D. Determination of improved climatic conditions for thermal comfort and energy efficiency in electric buses. Appl Ergon 2022;105. https://doi.org/10.1016/j.apergo.2022.103856.

[109] Hasan MM, Maas J, El Baghdadi M, de Groot R, Hegazy O. Thermal Management Strategy of Electric Buses towards ECO Comfort. 8th Transp Res Arena Conf (TRA 2020) 2020.

[110] Li L, Gao S, Wang B, Li C, Wang Y, Sun B, et al. Analysis of cooling and heating characteristics of thermal management system for fuel cell bus. Int J Hydrogen Energy 2023;48:11442–54. https://doi.org/10.1016/j.ijhydene.2022.07.083.

[111] Photovoltaic geographical information system (PVgis) n.d. https://re.jrc.ec.europa.eu/pvg_tools/en/.

[112] Nazir H, Muthuswamy N, Louis C, Jose S, Prakash J, Buan MEM, et al. Is the H2 economy realizable in the foreseeable future? Part III: H2 usage technologies, applications, and challenges and opportunities. Int J Hydrogen Energy 2020;45:28217–39. https://doi.org/10.1016/j.ijhydene.2020.07.256.

[113] Micena RP, Llerena-Pizarro OR, de Souza TM, Silveira JL. Solar-powered Hydrogen Refueling Stations: A techno-economic analysis. Int J Hydrogen Energy 2020;45:2308–18. https://doi.org/10.1016/j.ijhydene.2019.11.092.

[114] Chen Q, Gu Y, Tang Z, Wang D, Wu Q. Optimal design and techno-economic assessment of low-carbon hydrogen supply pathways for a refueling station located in Shanghai. Energy 2021;237.

[115] Gökçek M, Kale C. Techno-economical evaluation of a hydrogen refuelling station powered by Wind-PV hybrid power system: A case study for İzmir-çeşme. Int J Hydrogen Energy 2018;43:10615–25. https://doi.org/10.1016/j.ijhydene.2018.01.082.

[116] Ghaithan AM, Mohammed A, Al Hanbali A, Alshibani A. A Mixed Integer Linear Programming Model for Optimal Sizing of Hydrogen Refueling Station Powered Using a PV-Grid System. Arab J Sci Eng 2025;50:11129–44. https://doi.org/10.1007/s13369-024-09481-w.

[117] Öztürk RA, Devrim Y. Optimal design and technoeconomic analysis of on-site hydrogen refueling station powered by wind and solar photovoltaic hybrid energy systems. Renew Energy 2025;245. https://doi.org/10.1016/j.renene.2025.122788.

[118] Toghyani S, Baniasadi E, Afshari E. ScienceDirect Performance assessment of an electrochemical hydrogen production and storage system for solar hydrogen refueling station. Int J Hydrogen Energy 2021;46:24271–85. https://doi.org/10.1016/j.ijhydene.2021.05.026.

[119] Ottani F, Pedrazzi S, Morselli N, Puglia M, Allesina G. Seeking the synergistic potential of biochar integration in municipal composting plants for techno-economic and environmental leverage. Sustain Energy Technol Assessments 2024;64. https://doi.org/10.1016/j.seta.2024.103717.

[120] Antonini C, Treyer K, Streb A, van der Spek M, Bauer C, Mazzotti M. Hydrogen production from natural gas and biomethane with carbon capture and storage - A techno-environmental analysis. Sustain Energy Fuels 2020;4:2967–86. https://doi.org/10.1039/d0se00222d.

[121] Yagüe L, Linares JI, Arenas E, Romero JC. Biohydrogen production through biomethane steam reforming with CCUS for decarbonizing Spain's tile industry. Results Eng 2024;24. https://doi.org/10.1016/j.rineng.2024.103361.

[122] Ugurlu A. An emission analysis study of hydrogen powered vehicles. Int J Hydrogen Energy 2020;45:26522–35. https://doi.org/10.1016/j.ijhydene.2020.05.156.

[123] Zamri MFMA, Hasmady S, Akhiar A, Ideris F, Shamsuddin AH, Mofijur M, et al. A comprehensive review on anaerobic digestion of organic fraction of municipal solid waste. Renew Sustain Energy Rev 2021;137:110637. https://doi.org/10.1016/j.rser.2020.110637.

[124] Mousania Z, Rafiee R, Moeinaddini M, Atkinson JD. Anaerobic digestion of the organic fraction of municipal solid waste in a simulated bioreactor to improve predictive modeling of landfill systems. J Hazard Mater Adv 2024;13:100396. https://doi.org/10.1016/j.hazadv.2023.100396.

[125] Ottani F, Parenti M, Santunione G, Moscatelli G, Kahn R, Pedrazzi S, et al. Effects of different gasification biochar grain size on greenhouse gases and ammonia emissions in municipal aerated composting processes. J Environ Manage 2023;331:117257. https://doi.org/10.1016/j.jenvman.2023.117257.

[126] Kleinrahm R, Duschek W, Wagner W, Jaeschke M. Measurement and correlation of the (pressure, density, temperature) relation of methane in the temperature range from 273.15 K to 323.15 K at pressures up to 8 MPa. J Chem Thermodyn 1988;20:621–31. https://doi.org/10.1016/0021-9614(88)90092-4.

[127] Salam MA, Ahmed K, Akter N, Hossain T, Abdullah B. A review of hydrogen production via biomass gasification and its prospect in Bangladesh. Int J Hydrogen Energy 2018;43:14944–73. https://doi.org/10.1016/j.ijhydene.2018.06.043.

[128] Kumar P, Fiori L. Thermochemical and biological routes for biohydrogen production: A review. Energy Convers Manag X 2024;23:100659. https://doi.org/10.1016/j.ecmx.2024.100659.

[129] Krótki A, Bigda J, Spietz T, Ignasiak K, Matusiak P, Kowol D. Performance Evaluation of Pressure Swing Adsorption for Hydrogen Separation from Syngas and Water–Gas Shift Syngas. Energies 2025;18. https://doi.org/10.3390/en18081887.

[130] Demol R, Dufour A, Rogaume Y, Mauviel G. Production of Purified H2, Heat, and Biochar from Wood: Comparison between Gasification and Autothermal Pyrolysis Based on Advanced Process Modeling. Energy and Fuels 2022;36:488–501. https://doi.org/10.1021/acs.energyfuels.1c03528.

[131] Nesamani KS, Subramanian KP. Development of a driving cycle for intra-city buses in Chennai, India. Atmos Environ 2011;45:5469–76. https://doi.org/10.1016/j.atmosenv.2011.06.067.

[132] Yuhui P, Yuan Z, Huibao Y. Development of a representative driving cycle for urban buses based on the K-means cluster method. Cluster Comput 2019;22:6871–80. https://doi.org/10.1007/s10586-017-1673-y.

[133] Wayne WS, Clark NN, Nine RD, Elefante D. A comparison of emissions and fuel economy from hybrid-electric and conventional-drive transit buses. Energy and Fuels 2004;18:257–70. https://doi.org/10.1021/ef030096t.

[134] Hucho WH, Sovran G. Aerodynamics of road vehicles 1993:485–537.

[135] Balakrishnan M, Ellappan AP, Krishnan S. Experimental aerodynamic drag reduction studies on bus coaches of India. SAE Tech Pap 1989. https://doi.org/10.4271/892532.

[136] Palanivendhan M, Chandradass J, Saravanan C, Philip J, Sharan R. Reduction in aerodynamic drag acting on a commercial vehicle by using a dimpled surface. Mater Today Proc 2021;45:7072–8. https://doi.org/10.1016/j.matpr.2021.01.884.

[137] Islameka M, Leksono E, Yuliarto B. Modelling of regenerative braking system for electric bus. J Phys Conf Ser 2019;1402. https://doi.org/10.1088/1742-6596/1402/4/044054.

[138] Islameka M, Haq IN, Leksono E, Yuliarto B. Energy Consumption Simulation and Analysis of Rear-Driven Electric Bus with Regenerative Braking. Proceeding 6th Int Conf Electr Veh Technol 2019:105–10. https://doi.org/10.1109/ICEVT48285.2019.8994012.

[139] Tian S, Wang Y, Wu L. Parameters Matching and Effects of Different Powertrain on Vehicle: Performance for Pure Electric City Bus. SAE Tech Pap 2015;2015-01–27. https://doi.org/10.4271/2015-01-2799.

[140] Fox H, Eweka E. Simulation of hybrid buses: A study of fuel economy and emissions. WIT Trans Built Environ 2009;107:129–41. https://doi.org/10.2495/UT090131.